Integrated Aerodynamic and Structural Measurements of the Gust Response of a Flexible Wing with Robotic PIV

Tomás de Rojas Cordero

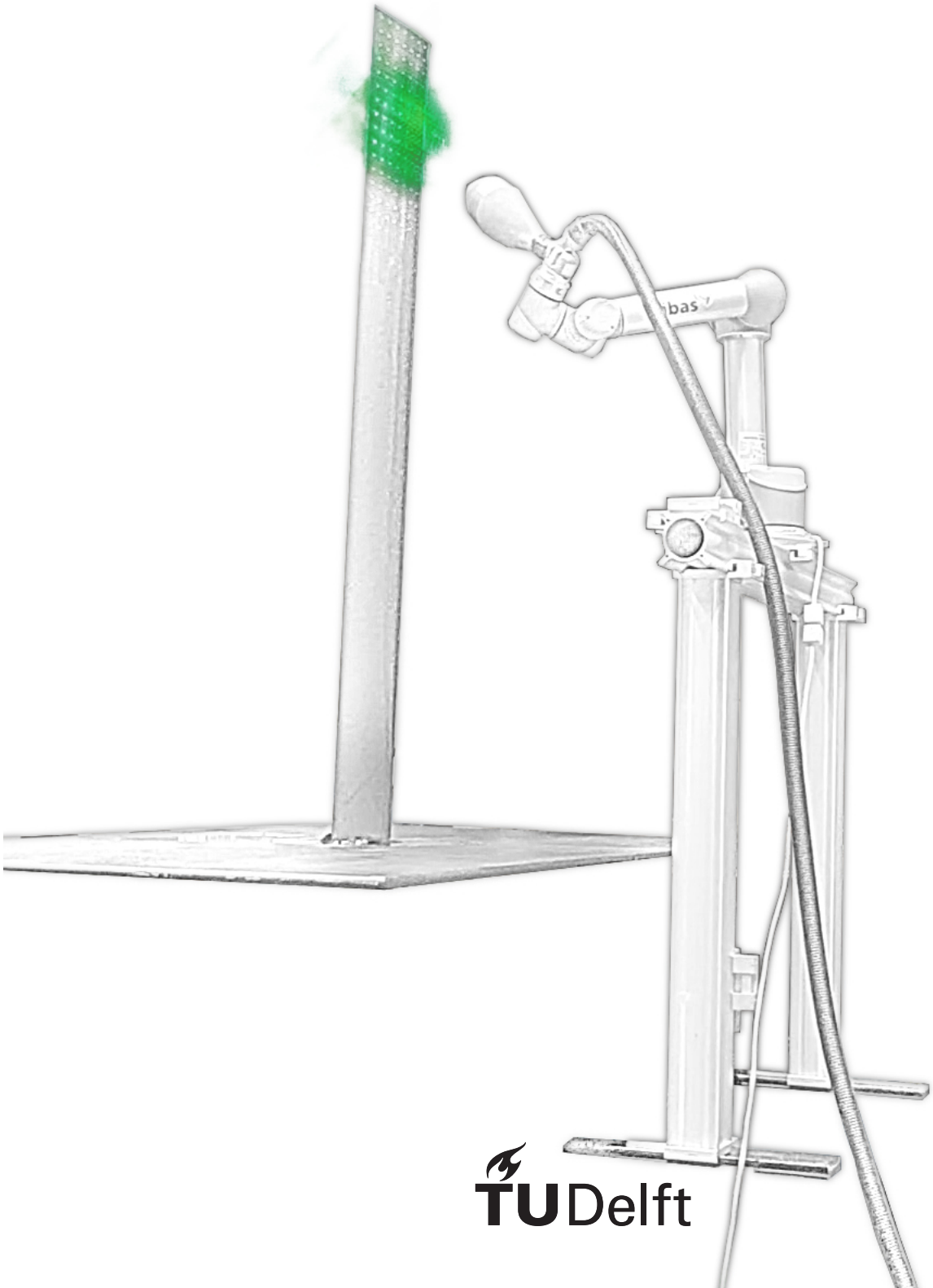

TU Delft

Integrated Aerodynamic and Structural Measurements of the Gust Response of a Flexible Wing with Robotic PIV

by

Tomás de Rojas Cordero

to obtain the degree of Master of Science
at the Delft University of Technology,
to be defended publicly on March 13, 2020 at 10:00 AM.

Student number:	4723473	
Project duration:	April 15, 2019 – March 13, 2020	
Thesis committee:	Dr. ir. B.W. van Oudheusden	TU Delft, Chair of assessment committee
	Dr. A. Sciacchitano	TU Delft, supervisor
	Ir. C. Mertens	TU Delft, daily supervisor
	Dr. ir. R. De Breuker	TU Delft, ASM, external

TU Delft

Acknowledgements

When reaching important milestones it is always important to look back and think about all the help one has received along the way. Finishing my studies in aerospace engineering is definitely a special occasion and, therefore, I would like to use this page to thank a series of people.

I would like to start by thanking Andrea Sciacchitano and Bas van Oudheusden for their supervision during my thesis project and for the genuine interest they showed for my work whenever I had questions or doubts about which direction to take in my research. I am also thankful to Jurij Sodja and Darwin Rajpal for their help before, during and after my experiments. Last but not least, a special thanks goes out to Christoph Mertens for dealing with my questions and sense of humour almost daily over the past 10 months. I have enjoyed working with you a lot and I believe it is fair to say that without your inputs, constructive criticism and relaxed spirit, this thesis would have looked very different.

Secondly, I would also like to thank Robbie Stevens from Renault Formula 1 for giving me the chance to experience what working in a top engineering environment is like. I learnt a lot from you both personally and professionally, and I will always keep a fond memory of my time with the Team.

Looking back, I am also extremely thankful for all the friends who have been with me over the past few years in the Netherlands, UK, Madrid, US and back home in Santiago. I feel privileged to have met such an amazing group of people, and I really hope I will continue to enjoy your friendship over many years because life would have not been as enjoyable as it has been without you. You have made me a better person and I have learnt from you as much (if not more) as I have learnt from my studies. All I can say is that I hope I have been as good of a friend to all of you you as you have been to me. Thank you very much.

Finally and most importantly, I want to thank my family and especially my parents. It's hard to put into words how grateful I am for all you have done for me, Juan and Javi. You are the people I admire the most in this world, and you have been a constant source of inspiration throughout my life. I cannot thank you enough for your support in every decision I have taken over the last few years, which has allowed me to have the best first 25 years of life any person could hope for. I also want to thank my grandparents, Tita and the rest of my family for all the love, support and advice you have constantly given me. The work in this thesis and the rest of my achievements would not have been possible without all of you.

Muchísimas gracias a todos.

Dedicado a mi familia

Tomás de Rojas Cordero
Delft, March 2020

Contents

List of Figures

List of Tables

Nomenclature

Acronyms

BFS	Bubble Soap Fluid
CMOS	Complementary Metal-Oxide-Semiconductor
CVV	Coaxial Volumetric Velocimetry
DNS	Direct Numerical Simulation
DOF	Degree of Freedom
HFSB	Helium Filled Soap Bubbles
IPR	Iterative Particle Reconstruction
LDV	Laser Doppler Vibrometry
LES	Large Eddy Simulation
NLR	Netherlands Aerospace Center
OJF	Open Jet Facility
OTF	Optical Transfer Function
PIV	Particle Image Velocimetry
ppp	Particles per pixel
px	pixel
RAM	Random Access Memory
RANS	Reynolds-Averaged Navier Stokes
STB	Shake-The-Box
VSC	Volume Self Calibration

Symbols

α_G	Angle of attack induced by the gust
α_w	Wing static angle of attack
α_{eff}	Effective angle of attack
α_{st}	Angle of attack induced by the wing motion
β	Tomographic aperture angle
δ_G	Deflection of the gust generator vanes
Γ	Flowfield circulation
κ	Reduced frequency
λ_g	Gust wavelength

μ	Fluid dynamic viscosity
μ_{st}	Mass distribution of the wing
$\overline{x}_{err}$	Average fit error of the wing reconstruction
ρ_f	Fluid density
ρ_p	Flow tracer density
ρ_∞	Freestream density
σ_u	Standard deviation of the velocity
τ_p	Flow tracer response time
ε	Longitudinal strain
ε_u	Relative uncertainty of PIV velocity measurements
$\varepsilon_{\Delta X}$	Wing reconstruction error in X direction
$\varepsilon_{\Delta Y}$	Wing reconstruction error in Y direction
a_Y	Acceleration in Y direction
a_Z	Acceleration in Z direction
b	Wing Span
C	Particle concentration
c	Airfoil Chord
C_S	Scattering cross section
$c_{l\alpha}$	Slope of the lift coefficient curve of a wing section
d_p	Flow tracer diameter
d_τ	Particle image size
E	Young's Modulus
f_G	Gust frequency
F_y	Total transverse force
F'_y	Transverse force per unit length
I	Second Moment of Inertia
I_0	Laser intensity
k_T	Phase averaging time kernel
l_b	Linear size of ensemble averaging cell
M	Image magnification factor
M	Moment
N_{unc}	Number of uncorrelated samples
P_S	Total scattered power
Q	Shear force

q_{aero}	Aerodynamic loading acting on the wing
q_{inr}	Inertial loading acting on the wing
q_{ufm}	Uniform loading acting on the wing
T	Duration of a sinusoidal gust cycle
t	Physical time
t^*	Non-dimensional time
U_∞	Freestream velocity
U_{slip}	Flow tracer slip velocity
v_0	Amplitude of the transverse velocity signal
v_G	Transverse velocity induced by the gust
w	Deflection of the wing beam model
x_G, y_G, z_G	Global coordinate system
x_{R1}, y_{R1}, z_{R1}	Robot base coordinate system 1
x_{R2}, y_{R2}, z_{R2}	Robot base coordinate system 2
z_a	Coverage factor in uncertainty calculations
Ø	Marker diameter

1

Introduction

From the very beginnings of human flight starred by the Wright brothers in 1903, it became clear that, in order to guarantee the safety and progress of aviation, it would be necessary to fully understand the interactions between the different structural elements of the planes and the air flowing around them. Pilots and engineers soon noticed that the structural and aerodynamic forces were not individual entities that could be dealt with independently, but that there existed different types of couplings between them that needed to be considered to achieve successful flights.

Some forms of coupling were intuitive and easier to understand, such as for example, the need to make a wing stiff enough to withstand the forces and moments associated to the generation of lift. On the other hand, other forms were more complex in nature and involved unsteady phenomena that only appeared in certain scenarios with causes that could be attributed to different factors: flight speed, structure properties, aerodynamic properties of the airplane etc.

The study of these interaction between man-made structures and the surrounding fluids constitutes the area of engineering known as aeroelasticity. It is a multi-disciplinary field which involves the coupling between forces with very different origins such as aerodynamic forces and structural forces. The study of aeroelasticity therefore requires a good understanding of the basic principles of aerodynamic and structural theory, how to implement that theory into computational solvers and how to measure all the relevant quantities in experimental investigations.

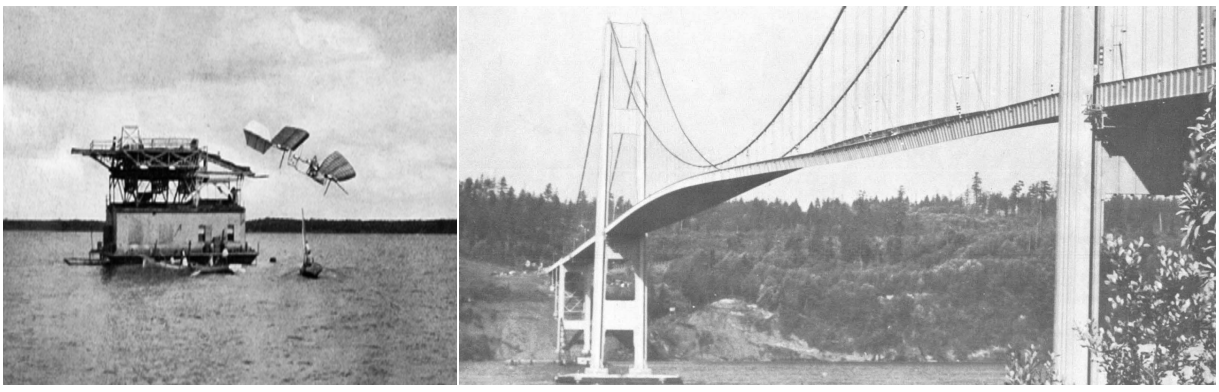

a) b)

Figure 1.1: a) Langley's flier,1903. Reproduced from www.wikipedia.org. b) Tacoma Narrows bridge during the 1940 events that led to its collapse. Reproduced from Ammann et al. [4]

Some early examples of the importance of these interactions were observed even before the first plane ever took off successfully. In November 1903, Samuel P. Langley conducted a test of his "flying machine" on the Potomac river in the United states. The vehicle suffered a catastrophic failure of its rear wing that was attributed to aeroelasticity and to the problem of divergence in particular. However, aeroelastic phenomena are not limited to airplanes. An aeroelastic instability caused the famous collapse of the Tacoma Narrows bridge in 1940 (see Ammann et al. [4]) in what is perhaps one of the most famous incidents in the field of aeroelasticity, highlighting the importance of this field in the design of civil structures. It also plays a vital role in the structural design of wind turbines, as well as in the behaviour of other complex machines such as Formula 1 cars.

The field of aeroelasticity is currently very active in both industrial and academic contexts. In industry, aeroelasticity plays an important role in the safety certification of airplanes, wind turbines or civil constructions for example. On the other side, research work includes exploring the use of more complex structural architectures or the use of advanced materials such as composites or exotic metal alloys. In both contexts, aeroelastic investigations rely mainly on two approaches. Firstly, computer simulations coupling aerodynamic and structural solvers can be used, having the advantage of allowing a quick, relatively inexpensive evaluation of multiple test cases. Secondly, experimental campaigns in wind tunnels are also conducted to confirm the findings of the simulations. These campaigns generally involve the use of several measurement systems in order to acquire the necessary information to fully characterize the experiments.

This introduction only covers some basic points of aeroelastic theory which are relevant to the topic of the work of this thesis. For a detailed review of the foundations of this discipline, the reader is referred to introductory texts such as the work of Dowell et al. [18].

1.1. Collar's triangle

A particularly important factor in the study of aeroelasticity is the fundamentally different nature of the three main force components at play. The aerodynamic forces arise from the interaction between an object and a fluid which manifest themselves predominantly through the pressure on the surface of the object. On the other hand, elastic forces are related to structural properties of the object such as its stiffness and manifest themselves as stresses when the object experiences a deformation. Finally, inertial forces arise from the fact that the object has a mass and undergoes an acceleration.

One of the first researchers who realized what the key elements were was A.R. Collar, who proposed to summarize the field of Aeroelasticity into a single diagram (Collar [15]), famously known as Collar's triangle and shown in Figure 1.2.

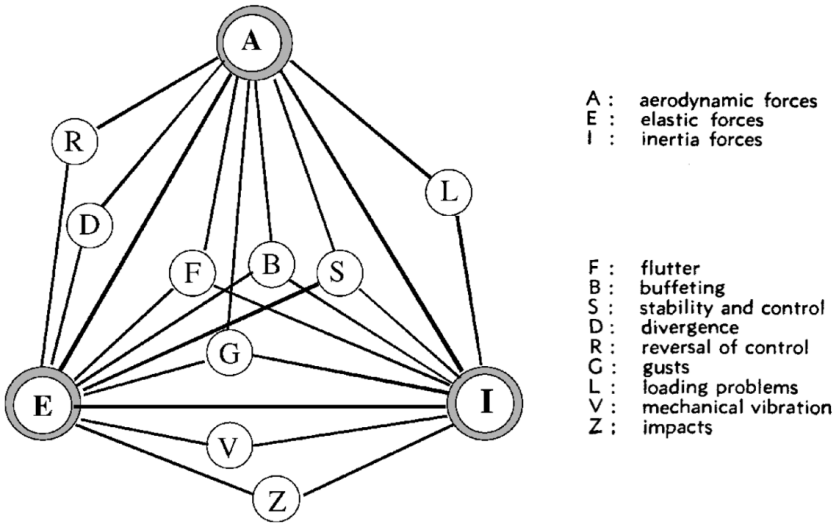

Figure 1.2: Collar's Triangle of forces, representing the interactions that give rise to the classical aeroelasticity problems. Reproduced from Collar [15].

The diagram shows the three main forces in its vertices, as well as how the interaction between two or three of those vertices gives rise to problems of different nature. Some of them do not involve all elements of aeroelasticity: vibrations and impacts belong to the field of solid mechanics for example, and loading problems belong to flight mechanics. However, the interaction between aerodynamic and elastic forces is the source of divergence and control reversal, which are two classical areas of static aeroelasticity. Furthermore, in the middle of the triangle we can find famous dynamic aeroelastic phenomena such as flutter, buffeting, stability and gusts, which arise as an interaction between the three forces and which can be considered as the problems with the highest complexity.

A second classification that is usually established (Wright and Cooper [77]) is the distinction between static and dynamic aeroelasticity. Static aeroelasticity deals with non-oscillatory effects caused by aerodynamic forces on the structure of aircraft. A clear example of this is the problem of divergence, where the aerodynamic pitching moment of the wing exceeds the restoration moment coming from the structure. This causes the twist of the wing to increase and can potentially lead to a catastrophic failure.

On the other side, dynamic aeroelasticity deals with oscillatory interactions, of which perhaps the most famous example is the phenomenon of flutter. Here, the coupling of two or more[1] flexible modes of a structure favours the extraction of energy from the airstream by the structure. This leads to a sustained oscillatory response which, under the right conditions, can grow without bounds powered by that energy extraction and eventually lead to a collapse of the structure after surpassing the stress safety margins.

1.2. Gusts

One of the problems connected to all three vertices of Collar's triangle of forces is that of gust encounters, and it is also the problem chosen as a test case in this study.

Gusts are a manifestation of atmospheric turbulence that is often encountered by aircraft. They are caused by localized currents of air that move in a direction that is not aligned with the flight path, which can have different origins such as thermal effects close to the ground (sun heats up the surface and the adjacent air, causing it to rise), topological features of the terrain (mountains) or shear layers in the proximity of the jet streams in the upper atmosphere.

As events that aircraft experience often and that can result in passenger discomfort in the less severe cases, or loss of control of the airplane and even catastrophic failure in the most severe situations, gusts are nowadays included as part of the aircraft certification process. The requirements that aircraft must fulfill are contained in specific regulations authored by the aviation authorities, such as the Federal Aviation Administration (Federal Aviation Administration [22]) or the European Aviation Safety Agency (EASA [19]).

This is not only a topic that has been introduced in the modern era of aviation. Gust effects were already identified as an important factor as early as 1915, only 12 years after the first manned flight. In a report authored by Wilson [76], an analytical approach was used to try to describe the effect of different types of gusts (head on, vertical, lateral...), discovering the potential effect that this phenomena could have on aircraft flight.

In the present day, the basic concepts about the structure of gusts and how they can affect structures such as airplane wings or wind turbine blades are well understood. However, gust encounters are still an active area of research. For example, the increase in use of composite materials in modern aircraft in an effort to save weight has led to the production of studies that try to optimize the weight of a given wing by using composite materials while ensuring that structural safety margins are still satisfied. An example is the study by Rajpal et al. [54], where the laminate of a composite wing was optimized across a variety of static and dynamic load cases, showing the importance of including gust loads in the preliminary design of composite wings.

[1] Single-mode responses are also possible in some cases, such as stall flutter.

1.3. Analysis methods for aeroelastic problems

Theoretical Models

Theoretical aeroelasticity relies on simplified models of both structure and aerodynamics. The most classical example is the work of Theodorsen [68] and Von Karman and Sears [72] on the typical airfoil section based on linearized potential aerodynamics. Their models use important simplifications of the flow analysis, such as 2D flow, thin airfoil theory and small perturbations. However, by including the effect of the wake of the airfoil on the aerodynamics of the airfoil itself, they were capable of explaining some of the classical aerodynamic unsteady effects, such as the lag between the transient motion of an airfoil and the loads it experiences.

The theoretical models are therefore limited to some basic applications but the results they offer can be very useful. Also, the physical principles they use are the basis of the more complex and versatile computational methods which will be briefly introduced in the next section.

Computational Methods

While useful and insightful, these analytical models can generally only be applied to very simplified versions of real-world problems. However, the basic rules of physics behind those theoretical models can be implemented in computer models that can solve much more complex cases. Nowadays, a wide array of aerodynamic and structural computer solvers are available.

Aerodynamic software usually relies on the discretized version of the Navier-Stokes (NS) equations of fluid dynamics. The discretization is generally done in the form of Finite Volume Methods that can easily be adapted to flows around complex geometries. From the user point of view, it is important to emphasize that these solvers all use simplified versions of the NS equations, especially when it comes to the treatment of turbulence. Depending on the level of simplification, different solvers arise. The simplest solvers are those known as potential solvers, where the effect of viscosity is neglected. Solvers that include this effect range from the Reynolds-Averaged Navier Stokes (RANS) Solvers and the Large Eddy Simulation (LES) ones. The possibility of a Direct Numerical Simulation (DNS) of the NS equations also exists, although its use is not practical for large scale aerospace simulations due to the computational effort required for it.

On the structural side, simulations usually rely on the Finite Element Method (FEM), where the structure is modelled by a series of elements connected at discrete points.

In the context of aeroelastic simulations, both a CFD and a FEM solver are needed to compute the coupled interaction between flow and structure. From the point of view of the users, it is common to treat solvers as black boxes and focus on providing them with the right inputs and boundary conditions at each timestep. For example one could start by giving the CFD solver a certain geometry, from which the aerodynamic pressure can be extracted. That pressure can then be inputted as a load field to the FEM model which then outputs the deformed shape of the body. This procedure is known as a coupled iterative simulation, and several iteration schemes are available depending on the properties of the problem at hand. For a detailed review of computational methods in aeroelasticity the reader is referred to Hou et al. [32].

The computational approach is widely used in aeroelastic investigations due to its versatility and its affordability in comparison to wind tunnel campaigns. However, all computational models rely on a certain set of assumptions, meaning that they can misrepresent the real physics up to a certain degree. This justifies the need for occasional experimental validations to ensure that computer models are indeed capturing the right physics and, if they are not, to identify the possible causes for the mismatch and to quantify the uncertainty in the results.

Experimental campaigns

The need for experimental data, either to investigate the true structure or to validate theoretical and computational models, has motivated several lines of research in the area of experimental aerodynamics. In this sense, the characterization of aeroelastic events in wind tunnels is a complex and expensive task which requires equipment both to replicate unsteady conditions relative to aeroelasticity (such as gust generators like the one built by Lancelot et al. [39]) and also to measure the aerodynamic and structural variables of the problem.

The measurement of those quantities of interest poses a significant technological challenge as it requires

capturing variables of very different nature simultaneously and, ideally, in a non-intrusive way. The resolution of the data is another important factor, as the complete understanding of aeroelastic problems sometimes requires full-field information.

The focus of this thesis is placed on the experimental approach and will deal with how simultaneous and coherent aerodynamic and structural data can be measured and acquired during experimental investigations. Traditional approaches involve the coordinated use of several measurement systems, where each one of them is used for the measurement of a single quantity. Some examples of these measurement systems are accelerometers, strain gauges and force balances for structural variables, and pressure probes and PIV for aerodynamic quantities. Most of these systems have some limitations in common such as their intrusiveness in the flow and structure or the resolution of their output, which need to be taken into account. Moreover, the combined use of several of these tools results in very complex and expensive wind tunnel setups which must be specifically tailored for each investigation, meaning that their versatility is limited.

Based on these considerations, a need exists for a single measurement system capable of providing simultaneous, synchronized and coherent data in aeroelastic experiments. This thesis proposes the state-of-the-art technique of robotic PIV as a system capable of satisfying these requirements and that could become an alternative to traditional measurement systems, overcoming the aforementioned shortcomings.

Robotic PIV has already been shown to be a valuable tool to obtain full-field volumetric aerodynamic measurements. It relies on the robotic manipulation of a Coaxial Volumetric Velocimetry probe in combination with the use of Helium-Filled-Soap-Bubbles as flow tracers, which are then tracked in time and space with an advanced tracking algorithm commonly referred to as Shake-The-Box and introduced by Schanz et al. [62]. The technique was first introduced by the work of Jux et al. [35], where the time-averaged, low-speed flow-field around a full-scale cyclist replica was measured. In addition, Saredi et al. [56] showed that the approach can be extended to higher speeds with some modifications to the acquisition process, and Martinez et al. [47] proved that it can also be used to acquire phase-averaged unsteady information by studying the wake of a flapping micro-air vehicle. In order to extend its range of application to aeroelastic problems, Mitrotta et al. [49] used the system to perform the simultaneous tracking of both flow tracers and reflective markers placed on the surface of a flexible flat plate.

1.4. Structure of this report

The research of this thesis and the structure of this document are motivated by the following research objective:

"Develop a framework for the use of the robotic PIV system as a tool for integrated, simultaneous and coherent aerodynamic and structural measurements by means of an experimental campaign on a flexible wing exposed to discrete and continuous gust excitations".

Therefore, the report starts in Chapter 2 with a review of the different measurement approaches used in experimental aeroelastic investigations. Their strengths and limitations will be highlighted, and the potential of PIV (and in particular Robotic PIV) as an alternative approach capable of overcoming the most important shortcomings will be presented. Following this, the research questions and objectives of the thesis are introduced.

In order to fulfill the research objective, an experimental campaign featuring a large-scale flexible wing with reflective markers is conducted in TU Delft's Open Jet Facility. Chapter 3 describes the facilities, test object (wing model) and the experimental setup. This includes a description of the robotic PIV system as the main measurement tool as well as secondary systems used to provide validation measurements. The campaign explored the static deflection of the wing at different speeds as well its the dynamic response during gust encounters.

The research objective also involves developing a methodology to process data acquired with robotic PIV and to use that information to reconstruct the relevant aeroelastic variables. This methodology is described in detail in Chapter 4. The first important point is how the raw images are processed in order to track both the structural markers and the flow tracers with the Shake-The-Box tracking algorithm. Secondly, the method used to reconstruct the deformed wing geometry and structural loads based on marker tracking information is discussed.

The results of the investigation are presented in Chapter 5. The reconstruction of the static deflection of the wing in a uniform flowfield is shown in the first place, followed by the unsteady results corresponding to the gust encounter cases. A good agreement between marker-based structural measurements and the references is found, and the unsteady aerodynamic response of the wing is discussed. Finally, the conclusions of the investigation are derived in Chapter 6 with the goal of answering the research questions. A series of recommendations for future work are also listed.

2

Literature Review

2.1. Experimental Tools for Aeroelastic Research

As mentioned in the previous section, one of the methods that can be used to gain insight into aeroelastic interactions is to perform experiments in wind tunnels. Experimental information is needed mainly to validate the results of numerical simulations, as well as to better understand the behaviour of complex structures without the need of intermediate modelling. This need for reliable experimental data was already addressed by Garrick [25] as early as 1976, highlighting the challenge of aerodynamic non-linearities as the origin of complex interactions and stating that *"Insight into such problems remains difficult to achieve and is fallible without supplementary experimental programs"*.

The development of experimental methods that can be used to acquire the data needed for validation has been and currently is an area of active research. In this section, an overview of the conventional techniques of widespread use is given, after which a review of the most modern methods will be conducted. The main distinctions used to structure this section and classify the methods are:

- The intrusiveness of the method, distinguishing between installed sensors or optical techniques. Installed sensors are considered as being intrusive since they can potentially modify the real response of the test object, by adding mass to it or disturbing its external aerodynamics for example.
- Whether the method is used for structural or aerodynamic characterization.

Industrial relevance

It is worth highlighting that many of the techniques to be presented in this chapter have found their way into the aerospace industry over the past decades. For example, the use of accelerometers and strain gauges reported in a review of industrial aeroelasticity practices by Garrigues [26], and non-intrusive techniques are presented as the state-of-the-art for wind tunnel testing by the German-Dutch Wind Tunnels [17].

2.1.1. Installed sensors

This section introduces some of the intrusive techniques available for the measurement of structural and aerodynamic variables in wind tunnels. In general, each of these techniques tends to be designed specifically for the measurement of a single variable and provide pointwise information.

Therefore, in order to get a full description of an aeroelastic problem, these techniques need to be combined with each other, increasing both the intrusiveness and complexity of the setups. However, many of them are still the reference techniques in their fields and their use is widespread through industry and academia.

Accelerometers

Accelerometers are electromechanical devices capable of measuring accelerations, and their use for structural testing and monitoring is widespread in the aerospace industry, as well as in Academia for both structural and aeroelastic tests in wind tunnels. For example, Govers et al. [30] offers a review of the use of piezoelectric accelerometers for ground vibration testing in industry. Many examples of their use are available in literature, but as a particular example, Gaspari et al. [27] use 4 single-axis piezoelectric accelerometers distributed along the span of a flexible wing to capture its bending response during a wind tunnel campaign. This work also shows that the measurements from several accelerometers correctly distributed can be used to indirectly measure secondary motions such as wing torsion.

Piezoelectric accelerometers consist of a clamped piece of piezoelectric material which, when compressed due to a force, produces an electric field such that the output voltage of the sensor is proportional to its acceleration. The dimensional and mass information of the accelerometer define that proportionality, as well as the operational frequency range which is the main parameter for the selection of an accelerometer for a particular application. A typical frequency response of an accelerometer is displayed in Figure 2.1, with the useful frequency domain defined as the frequency span over which the sensitivity of the sensor remains constant. More information about the working principles of these sensors can be found in Vijaya [71].

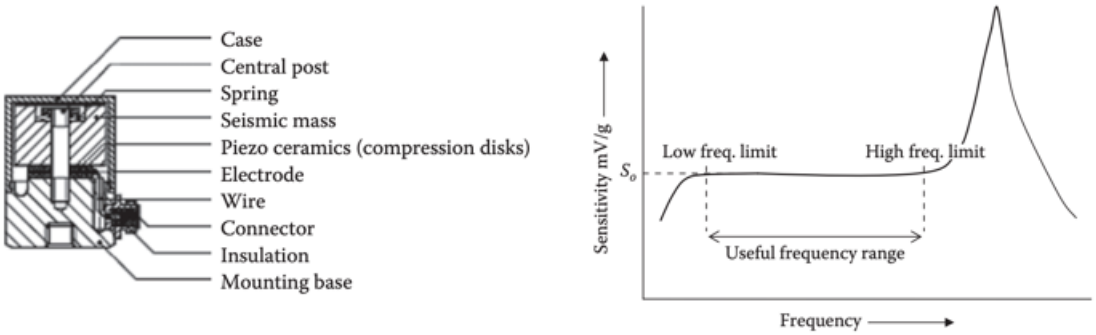

Figure 2.1: Typical arrangement (left) and frequency response (right) of a piezoelectric accelerometer. Reproduced from Vijaya [71]

Accelerometers can therefore be used to retrieve acceleration information along one or several directions depending on the type of sensor and/or its orientation. On the other hand, these devices still suffer from some limitations such as their intrusiveness, since they need to be firmly attached to the structure. This sometimes requires specific modifications to the structure in order to accommodate them, and it means that they can potentially alter the measurements in an aeroelastic campaign since they can change the mass structural properties, and even the aerodynamics at play if they are exposed to the flowfield. In addition, their output is limited to pointwise information and changing in their location is not always straightforward.

Force Balance

Force balances are one of the key pieces of instrumentation available for the evaluation of forces and moments in wind tunnel tests. There is a wide variety of balances that can be used for a test depending on its characteristics. Some distinctions often used to classify force balances are:

- Number of forces and moments that can be measured simultaneously (1 to 6).
- Placement: Internal (inside the wind tunnel model) or external (outside the model).
- Strain gauge balances or piezoelectric balances.

For a detailed review of the use of force balances in wind tunnel campaigns, the reader is referred to Tropea et al. [69]. The use of force balances is completely widespread, including their use in aeroelastic experiments such as the one performed by Dietz et al. [16], where a piezoelectric balance is used to determine the aerodynamic loads on a flexible wing.

The measurement of static resultant forces and moments and their evolution over time in dynamic cases allows for a structural characterization of the structure. On the other side, the fact that only the resultant force can be measured means that, for example, in the context of aeroelasticity experiments it is not possible to determine the distribution of that resultant force which may come from completely different origins (see Collar's triangle). In addition, it is also not possible to look at local effects of the loading on the structure. For these reasons, force balances often need to be complemented with other measurement devices such as accelerometers and strain gauges in order to get a complete understanding of the problem.

Their use is also not always straightforward since they require a careful calibration and they tend to be complex pieces of equipment as shown in Figure 2.2. Wind tunnel models will also have to be specifically designed to be attached to the balance, or to fit one inside them in the case of internal balances, constraining the design space of those models.

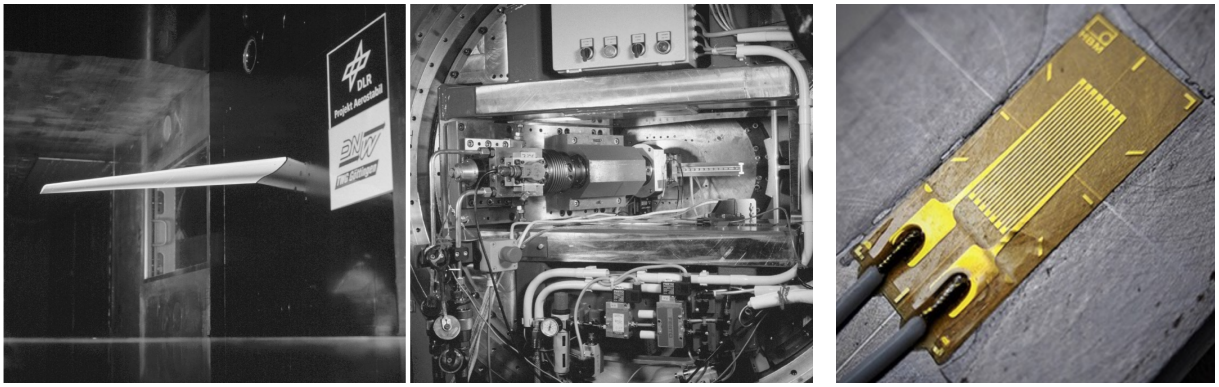

a) b)

Figure 2.2: a) Wind tunnel wing model mounted in the Transonic Wind Tunnel Göttingen (TWG) and detail of the mechanics of the force balance and hydraulic actuator. Reproduced from Dietz et al. [16]. b) Typical strain gauge. Reproduced from www.medium.com

Strain Gauges

In engineering, strains are defined as the relative displacements between to points in a structure which are not caused by solid-body motions. Strains can be related to stresses through the constitutive equations of the material of the structure (such as Hooke's law), and those stresses ultimately determine whether there is a risk of failure of the structure depending on the properties of the material.

The increase in use of composite materials in the aerospace industry has caused an increase in the interest to monitor local strains and stresses in composite structures due to the complex mechanical properties of composites such as their anisotropy.

The measurement of strains in wind tunnels has historically relied on the use of strain gauges such as the one shown in Figure 2.2, which are electrical sensors with a resistance that varies depending on the forces applied to them. They are delicate and require careful placement and wiring, as well as the use of secondary equipment such as a Wheatstone bridge. Their use is widely reported in aeroelastic campaigns such as the examples of Lin et al. [43] or Tang and Dowell [67], where the response of elastic wings is studied with the help of strain gauges and accelerometers. It is worth highlighting that strain gauges only provide pointwise information, meaning that it is often necessary to use several of them in order to fully characterize a structure.

An improvement from strain gauges can be achieved with the use of optic fibers, from which strains can be detected by using the change in optical pathlength as described by [11]. Some of their advantages are their small size and light weight, high spatial resolution, insensitivity to electromagnetic radiation and easy integration in composite materials as described by Ramakrishnan et al. [55]. Another improvement is the capability to provide information along a line (the fiber) instead of just pointwise information. Their use in wind tunnels is reported by Freydin et al. [23] for example, where fiber optic sensors were embedded in a wing for shape-sensing in both static and dynamic conditions.

a) b) c)

Figure 2.3: a) Wind tunnel model equipped with pressure taps, reproduced from www.cppwind.com. b) Multihole pressure probe, reproduced from www.surreysensors.com. c) Hot-wire probe for measurement of 3 velocity components, reproduced from www.dantecdynamics.com

Pressure probes and pressure taps

Aerodynamic pressure is one of the most important quantities to be measured during a wind tunnel investigation, since it allows the evaluation of aerodynamic forces. It is also relevant for phenomena such as boundary layer transition and flow separation, which can be a limiting factor when determining the aerodynamic performance of a structure. Pressure measurements usually rely on a hole exposed to the flowfield and connected to a piezoelectric transducer, which ultimately transforms the pressure reading into an electrical signal.

For a detailed review of the different methods, the reader is referred once again to Tropea et al. [69]. There exist several options depending on which pressure is of interest - static, total or dynamic pressure - and in general, all of them are intrusive as they require the introduction of a probe in the flowfield or in the test model. A limited review of some of those methods together with their advantages,limitations and examples of their use could include:

- **Pressure taps:** these are the reference method for the evaluation of pointwise static surface pressure, which is used for determination of loads. Holes of small diameter need to be drilled on the surface of the wind tunnel model and connected to a pressure transducer. The model needs to be specifically designed to accommodate them and they are very sensitive to contamination and manufacturing imperfections. Despite this, their use is widespread in aerospace (Chu and Luckring [14]) and civil wind tunnel investigations (Levitan and Mehta [42]).

- **Pitot tube and Multi-hole pressure probes**: Pitot tubes are used for the determination of the total and dynamic pressure of the flow. They use a hole that is aligned with the flow in order to stagnate the flow and determine the total pressure, which in combination with a static pressure port can be used to determine the dynamic pressure by subtracting both readings. They provide pointwise information and they tend to be fixed in space unless mounted on traverses, and they are sensitive to misalignments with respect to the flow direction.

  In order to reduce this sensitivity, multi-hole pressure probes were invented. By using the simultaneous readings from different holes, the orientation of the probe can be determined and then used to correct the total pressure reading based on a calibration dataset as described by Everett et al. [21]. Furthermore, the dynamic pressure reading can be used together with the orientation information to resolve the 3 flow velocity components. A picture of a multi-hole pressure probe can be seen in Figure 2.3, together with a model equipped with static pressure taps.

  More variations of this concept include pressure probe rakes, which can be used to sample a large domain at several points at the same time at the cost of increasing the intrusiveness. On the downside, a common limitation to all methods is the incapacity of performing measurements under reverse-flow conditions.

2.1.2. Optical measurement techniques

The previous section covered some of the main intrusive techniques that are normally used for flowfield and structural measurements in wind tunnels, and therefore in aeroelastic experiments. Even though many

of these techniques are very powerful methods for certain contexts, their intrusiveness has motivated the development of alternative techniques which are normally based on optical methods.

This section will cover some of the most relevant examples taking into account the context of the present project. On the structural side, Laser Vibrometry and techniques based on photogrammetry are highlighted. On the aerodynamic side, non-intrusive techniques include Laser Doppler Velocimetry and Particle Image Velocimetry. The first uses the interference pattern between two laser beams and the Doppler effect to produce pointwise velocity information, and will not be covered in this review. The second one represents the state-of-the-art of optical measurement techniques for aerodynamic measurements and uses high-speed imaging and laser illumination to capture the motion of flow tracers in images, from which the flow velocity can be subsequently derived. Since this is the primary measurement technique used in this thesis, its working principles and applications will be described in detail in Section 2.2.

Laser Doppler Vibrometry

A Laser Doppler Vibrometer (LDV) is an instrument that allows the measurement of the velocity of a point along a single axis. The technique is non-intrusive and takes advantage of the Doppler effect in order to perform the measurement: a laser beam is projected on a moving point and the light scattered from the surface is used to compute the Doppler frequency shift by comparing it to the reference laser beam. That Doppler shift is then used to compute the velocity component of the moving point along the line of sight of the laser. The system allows the measurement of high frequency vibrations, with sampling frequencies of the order of MHz. Furthermore, the introduction of the Scanning LDV allows the user to quickly change the measurement point, allowing vibration measurements of large structures in a short time, as shown by Sriram et al. [66].

An extensive review of this technique and its uses can be found in Castellini et al. [13]. While the spatial and velocity resolution are highlighted as some of the strong points of LDV, the misalignment between the real velocity vector and the laser beam is mentioned as an important source of uncertainty, which compromises the performance of the system in measuring high amplitude vibrations of the measurement point. Other known limitations are the fact that only one velocity component can be recovered and that the data is outputted as pointwise information, meaning that this cannot be considered as a full-field technique.

Photogrammetry

Photogrammetry is a measurement technique used to determine variables like displacement and deformation of a structure by using digital images. This field has seen significant advancements during the last decade mainly due to two factors:

- The aforementioned widespread interest in full-field, non-intrusive measurement techniques for structural characterization.
- The huge technological advancements in computer storage and processing capabilities and digital imaging sensors such as charge-coupled devices (CCD) and complementary metal-oxide semiconductor (CMOS).

In a broad sense, photogrammetry uses imaging sensors to identify the coordinates of markers or patterns placed on the surface of an object, from which displacements and deformations can be determined. The use of a single camera generally allows the measurement of displacements in a plane, while the use of 2 cameras in stereoscopic configuration can detect 3D displacements. This can also be achieved by increasing the number of cameras to 3 or more.

The use of cameras for photogrammetry normally requires a careful calibration process in order to detect and correct effects such as lens distortions, scaling of units and also to determine the real-world coordinates of the measured tracers. This process is usually performed by using images of a calibration pattern. The reader is referred to Baqersad et al. [6] for a detailed review of the techniques included in the photogrammetry field, while Liu et al. [44] offers another interesting review focusing on the applications of the techniques to the aerospace engineering context. The two techniques that will be covered in more detailed in this documents will be Point-Tracking and Digital Image Correlation (DIC).

Point/Marker Tracking consists, as its name suggests, on locating discrete points in space through images from cameras. The markers are typically circular and highly reflective targets which can be easily detected by the sensors, and the number of markers that can be tracked simultaneously is only limited by the optics and size of the sensor. The technique is very popular and thus there are several relevant examples of its use. For example, Kalpoe et al. [38] use marker tracking with a stereoscopic configuration to measure the out-of-plane vibrations of a model wind turbine in TU Delft's Open Jef Facility, as seen in Figure 2.4. In an earlier example, Schairer and Hand [60] also used stereo photogrammetry to reconstruct the deflected shape of a flexible wing in both static and dynamic conditions. In a more extreme case, the technique was extended to full-scale, in-flight testing by Burner et al. [10], who used a single camera to quantify the aeroelastic deflection of the wing of an experimental F/A-18 fighter plane, as depicted in Figure 2.4. Another trend in the marker tracking technique is its application to the characterization of complex flying structures, such as the flexible wings of nature-inspired micro air vehicles (MAV). The work of Heitzig et al. [31] shows this application in the case of the DelFly II MAV, which allowed the tracking of over 130 points simultaneously and the detection of previously unnoticed responses of the wings.

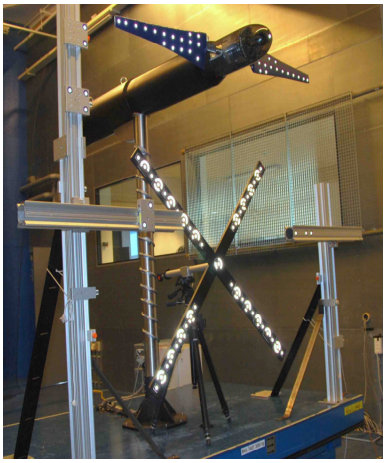

a)

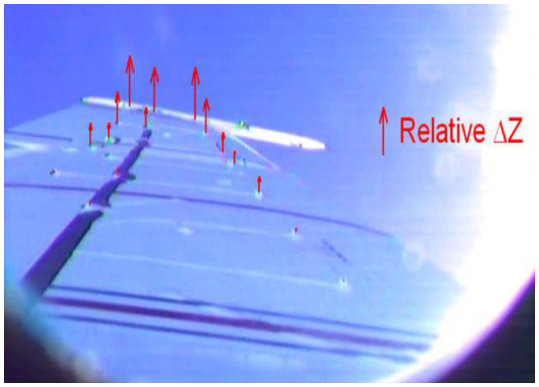

b)

Figure 2.4: a) Use of marker tracking for structural characterization of a model wind turbine. Reproduced from Kalpoe et al. [38]. b) In-flight measurements of the aeroelastic deformation of the F/A-18 Active Aeroelastic wing research aircraft. Reproduced from Burner et al. [10]

.

Digital Image Correlation (DIC) is the second optical technique covered in this section. Once again, the method makes use of images taken from one or several cameras to detect the deformation of a structure. In contrast to Point Tracking, this method is based on continuous randomized patterns imprinted onto the surface of interest rather than in discrete targets. It also has sufficient spatial resolution to accurately measure strains, from which stresses can be computed.

The working principle is based on taking images of the pattern in a reference, undeformed condition and later in a deformed condition. The images are then divided into small windows which are then compared between the loaded and unloaded (reference) condition by means of a cross-correlation algorithm, which makes this method computationally intensive. On the other hand, it has the advantage of providing full field information. This technique is also widely used, as in the study by Werter et al. [73] where the deformation of a wing was quantified by a stereoscopic DIC system.

2.1.3. Simultaneous aerodynamic/structural measurement

Until now, this section has covered the basics of an array of techniques that can be used to measure individual variables in a wind tunnel experiment. The techniques usually provide pointwise measurements of structural (acceleration, displacement, deformations...) and aerodynamic (flow velocities, pressure) variables, and in the best cases that information can be full field information.

As mentioned during the description of Collar's triangle of forces, aeroelastic problems are usually char-

acterized by the simultaneous interaction between different forces. During the previous section, some examples of how some of the techniques have been used in previous aeroelastic experiments to measure some of these forces were given, but there are two main problems that can be identified:

- Previous examples show that normally only one, or in the best case two techniques are used in order to characterize the problem. In addition, these techniques rarely provide information in more than a few discrete points, which might not be enough to understand the physics of the problem depending on its scale and/or complexity.
- Despite the division proposed by Collar, it can be considered that aeroelastic interactions have two main sides: the structural and the aerodynamic one. The second issue is that the previous studies in wind tunnels cited until now tend to focus only on one of the two sides, meaning that, for example, accelerometers and strain gauges might be used to characterize the structural response of a flexible wing. However the measured structural response is not related to the corresponding flowfield that is causing that response in the first place.

Therefore for a complete understanding of and aeroelastic problem, wind tunnel campaigns should strive to use a combination of these techniques which allows for a complete description of the problem while trying to keep the intrusiveness and complexity of the setups at reasonable levels. This is not a straightforward job, but it is a research gap that has been identified in Academia and some attempts have been made in order to solve it. Some relevant attempts found in literature will be described in the following paragraphs.

For clarification purposes, the reader should keep in mind the following general requisites for a hypothetical **ideal** measurement system for aeroelastic problems:

- The system should be able to capture both flowfield and structural information simultaneously.
- The system should provide sufficient information density, meaning that full-field information is preferred.
- The system should be non-intrusive, or as least intrusive at possible.
- The complexity of the system should be kept at reasonable levels, in the case of needing several pieces of equipment to perform the measurement. This requirement increases the versatility of the system.

These requisites tend to favor optical methods, which as the reader will notice are the protagonists of the following examples.

A common benchmark case for the validation of fluid structure interaction computer codes is that of a flexible plate attached behind a fixed cylinder. The vortex-shedding from the cylinder causes the plate to deform and thus a coupling between the flow and the structure is established. In the work of Kalmbach and Breuer [37], experimental data is acquired for this case in a water tunnel. The flowfield is captured by both PIV and Volumetric 3-component velocimetry, while the structural displacement is evaluated by means of a laser distance sensor. Moreover, the flowfield phase-averaged velocity data is used to reconstruct the pressure from the momentum equation of the Navier-Stokes equations allowing for a qualitative evaluation of the lift and drag coefficients.

A very similar and earlier case is that of Gomes and Lienhart [29], where the same setup is studied but using only one single PIV system consisting on two cameras in a parallel arrangement (so only 2D velocity information could be retrieved) to extend the field of view. The deformation of the structure was determined by using a special software developed to scan the PIV images and recognise the shape of the oscillating plate. The study was again limited to a water tunnel operated at low speed (4.5 m/s) and the method proposed for the structural measurements seems unsuitable for more complex 3D geometries.

A leap in complexity is done by Bleischwitz et al. [8] in their study on the fluid-structure interaction of flexible wings used for MAVs in ground effect. They use planar PIV for the flowfield characterization, together with DIC and load cell measurements for the structural response. A dotted pattern is imprinted on the flexible wings to allow the DIC measurements, while the load cell is integrated in the support structure of the wind tunnel model. Their setup, reproduced in Figure 2.5 produced planar information that allowed the study of

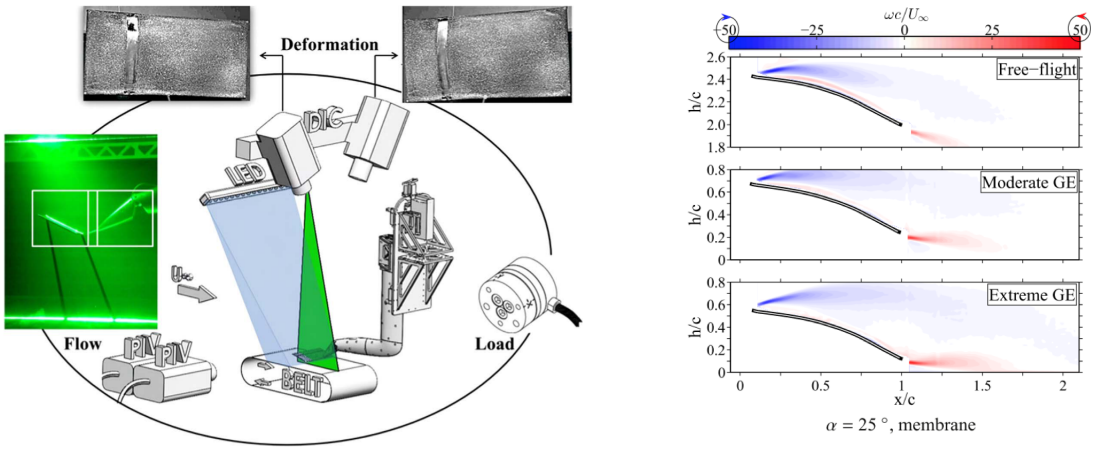

a) b)

Figure 2.5: a) PIV/DIC/Load Cell setup for combined simultaneous measurements. b) Time-averaged vorticity field for the flexible membrane wing at $\alpha = 25°$. Reproduced from Bleischwitz et al. [8].

the coupling between the flexible membrane and the flowfield in ground effect conditions, which highlighted some of the aerodynamic advantages of flexible membrane wings with respect to rigid plates.

Finally, Marimon Giovannetti et al. [46] successfully synchronise a stereoscopic PIV and a 3D DIC system, together with a force balance. The test object is similar to the one proposed for this thesis, a flexible composite wing of 0.9m of span, and the quantities of interest are the deformation of the wing and the position of the tip vortex. Their study reports that the accuracy of the DIC system is not significantly affected by the combination with the PIV system and vice versa.

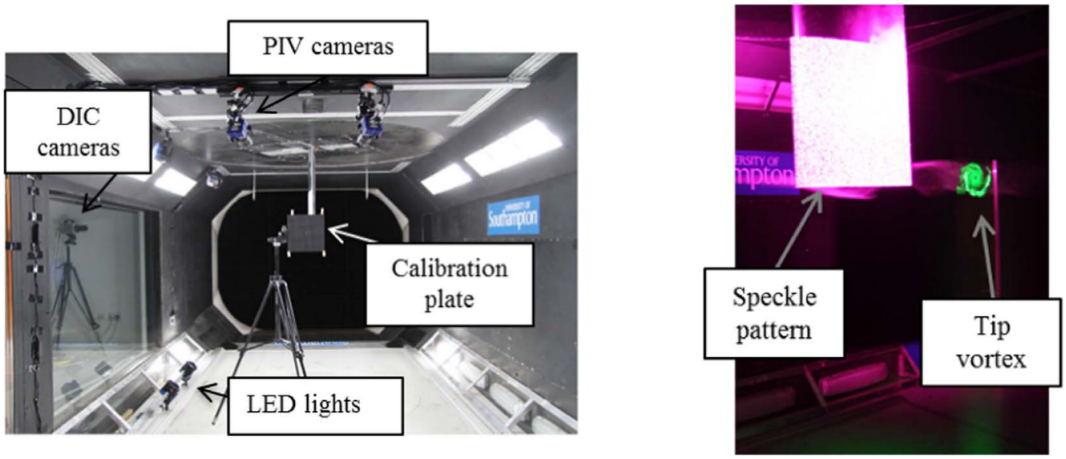

a) b)

Figure 2.6: a) PIV/DIC setup. b) Combined measurement of wing deflection (magenta ligth, DIC) and tip vortex (green light, PIV). Reproduced from Marimon Giovannetti et al. [46]

To the knowledge of the author, the previous examples are some of the most relevant for the purpose of this thesis. However, these cases still show some limitations from the point of view of "closing" Collar's triangle and measuring the interaction between all variables of aeroelasic problems simultaneously:

- Flowfield information is planar, which makes characterizations of complex 3D flows difficult and measurements of large domains costly.
- More than one system is needed to perform the measurements, causing a lack of versatility. Even though the presented examples show promising trends and results, using them for the full character-

ization of bigger and more complex structures would result in a very complex and time-consuming campaign.

2.1.4. Measurement systems: Summary

An overview of the most common techniques used in experimental investigations in the field of aeroelasticity has been conducted in the previous sections. As a final summary, Table 2.1 classifies the different methods according to the kind of information they can measure (Aerodynamic/Structural), their intrusiveness and the resolution of the output data.

Measurement System	Aerodynamic Information	Structural Information	Intrusive	Data Resolution
PIV (Planar/Volumetric)	Yes	No	No	2D/3D
Pressure Probe	Yes	No	Yes	0D
Accelerometers	No	Yes	Yes	0D
Laser Vibrometer	No	Yes	No	0D
Strain Gauge	No	Yes	Yes	0D
Optic Strain Fiber	No	Yes	Yes	1D
Photogrammetry (Marker Tracking/DIC)	No	Yes	No	2D
Force Balance	Yes*	Yes*	Yes	0D

Table 2.1: Table showing a simplified classification of typical measurement systems according to the type of quantity they measure and their intrusiveness. Pointwise information is referred to as "0D". *The force balance measures the global, combined effect of all forces but cannot separate them.

2.2. PIV and PTV as diagnostics methods in aerodynamics

The research to be conducted in this thesis is based on the state-of-the-art technique of robotic PIV, and therefore a review of the working principles of PIV and its evolution to the present day is necessary.

This section will cover the basics of planar PIV and its evolution towards stereoscopic and volumetric PIV. The text will also introduce the technological advancements in particle-tracking algorithms, seeding particles and hardware that have made possible large-scale volumetric PIV measurement possible by means of robot arm manipulation.

2.2.1. Working principles of PIV

Particle Image Velocimetry is a well established technique in the present day for the measurement of velocity fields in hydrodynamic, aerodynamic and even multiphase flows. Its use is widespread in Academia, with a growing use in industrial contexts. Its origins can be traced back to 1977, when researchers such as Barker and Fourney [7] used pulsed laser illumination and seeding particles to determine flow velocities based on laser speckles. However, the Particle Image Velocimetry nomenclature was first used by Adrian [1] who realised that speckle formation was not always possible due to the high seeding density needed, and that flow velocity could be determined based on the light scattered by individual particles.

As the name of the technique implies, it is an imaging technique that relies on the presence of reflective tracing particles in the flowfield. Those particles are chosen such that they will follow the flow with sufficient accuracy, and they are typically illuminated by a pulsed laser beam which is shaped into a laser sheet by

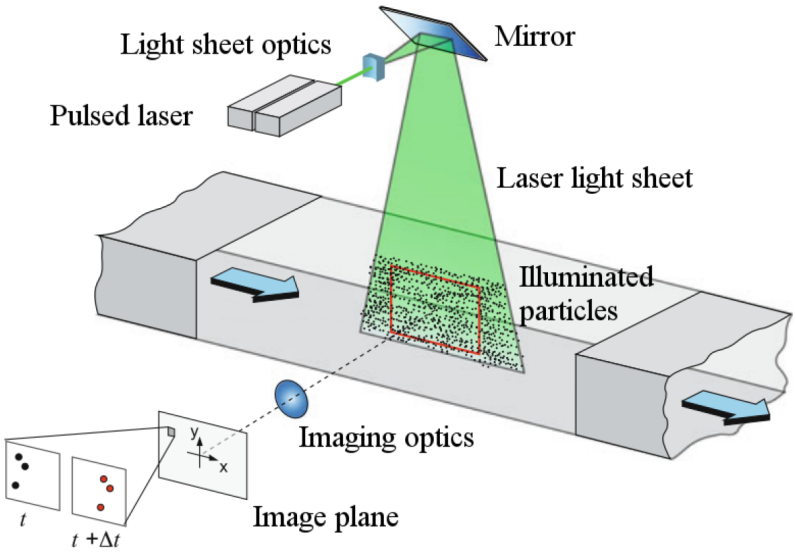

Figure 2.7: Typical PIV experimental wind tunnel setup.Reproduced from Raffel et al. [53]

means of a set of optics. When illuminated, the tracing particles will scatter light which can then be recorded by one or several cameras which must be carefully coordinated with the laser.

In its simplest planar configuration, shown in Fig.2.7, PIV makes use of a single camera which takes two successive images of the particles with a time separation Δt between them. Those two frames are then divided into small windows, and the displacement vector $\vec{d} = [\Delta x, \Delta y]$ of the particles within each window between time instants t and $t + \Delta t$ is computed using the statistical method of cross-correlation. Once the displacement vector is determined, the flow velocity can be immediately computed taking into account the time delay between frames and the magnification factor introduced by the optics:

$$u = \frac{\Delta x}{M \Delta t} \tag{2.1}$$

$$v = \frac{\Delta y}{M \Delta t} \tag{2.2}$$

By performing this operation for all the windows in the two frames, full instantaneous and time-resolved velocity fields can be reconstructed. This is one of the most remarkable advantages of PIV in comparison with other methods used for velocity measurements such as Hot Wire Anemometry or multi-hole pressure probes which can only measure pointwise data. Another major advantage is the non-intrusiveness of PIV, a quality of significant importance when studying complex flowfields or small-scale features. Finally, even though the postprocessing requires usually more time than other techniques, the amount of information that can be obtained in that time makes this an attractive tool. For a more detailed explanation of the principles and hardware needed for PIV the reader is directed to Raffel et al. [53].

However, the PIV technique in its previously defined form is only capable of recovering two components of the velocity field in a plane. This is a significant improvement in comparison to the techniques presented in the previous chapter in terms of intrusiveness and information density, but soon after the start of PIV efforts were directed towards capturing more information from the images.

One of the first relevant advances was the introduction of a second camera in the PIV setup by Arroyo and Greated [5]. This is not a complex change to the setup and on the other hand, the return improvement is significant since this optical arrangement is capable of measuring all 3 velocity components of the flowfield in a plane. On the other side, this information is still contained in a single plane, which might not be insightful enough to fully characterize and understand flows where complex 3D features are dominant.Consequently, after the introduction of stereoscopic PIV, many research lines were opened in the PIV community to retrieve volumetric, 3 component information from a flowfield.

Some early attempts to retrieve volumetric information made use of a stereoscopic PIV setup that could be moved along a certain direction in order to scan the flow in several successive planes. A clear example of this is the study by Nakagawa et al. [50] where several PIV planes are used to study the effect of certain aerodynamic devices on the wake of a car, or the work of Jenkins et al. [33] where again PIV planes are used to study the wake of a helicopter rotor. This approach to volumetric measurements has the advantage of having the same working principles as planar or stereoscopic PIV, meaning that there doesn't exist a remarkable increase in complexity. On the other side, it can be time-consuming to translate the equipment for each plane measurement, which compromises both the spatial and temporal resolution of the resulting measurements.

However, the biggest step towards 3-component volumetric PIV was achieved by introducing further cameras in the setup, as first shown by Elsinga et al. [20], in what is known as tomographic PIV. In their setup, the flow tracers are illuminated in a 3D region of space and imaged by 4 cameras with different orientations. The images from those cameras are then used to reconstruct the 3D particle distribution, which is a non-trivial problem for which specific algorithms have been developed. It is formally formulated as the problem of retrieving the 3D light intensity distribution $E(X,Y,Z)$ from the individual 2D projections of the particles on each camera $I(x_i, y_i)$, and in the aforementioned example the chosen algorithm is known as Multiplicative Algebraic Reconstruction Technique (MART). In addition, the 3D reconstruction is done in the image space, which means that a careful geometrical calibration will be needed to translate the results to real-world coordinates.

There are several examples of successful uses of tomographic available in literature. As mentioned by Scarano [57] in his detailed review of the tomo-PIV field, the advantages of this technique stand out in applications where the instantaneous flowfield needs to be retrieved in all three dimensions. This is why the technique has been studied for the study of wakes of bluff bodies such as cylinders (Scarano and Poelma [58]) and of coherent turbulent structures in wall-bounded flows (Gao et al. [24]).

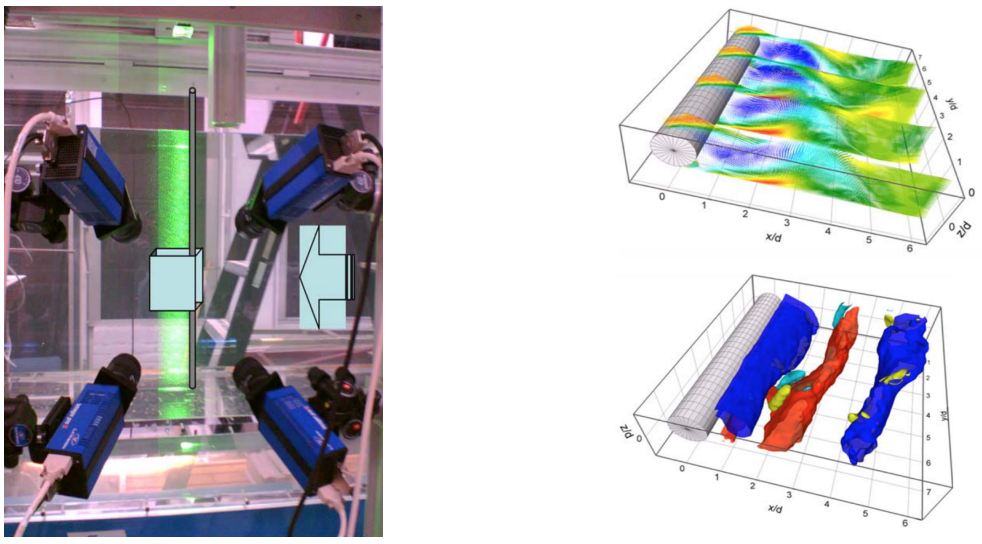

a) b)

Figure 2.8: a) Example of a typical tomographic PIV setup. b) Examples of results that can be achieved through tomographic PIV. Top: Velocity field in the wake of a cylinder, u-component. Bottom: Vorticity iso-surfaces. Reproduced from Scarano and Poelma [58]

,

However, tomographic PIV does suffer from some important limitations. Perhaps the most important one concerns the measurement volume, which is generally small (of the order of a few cm^3) due to the limitations in light-scattering properties of the tracer particles and the decrease in illumination power that lasers suffer when expanded into a volume. On top of that the technique does need significant optical access so its application to complex geometries might not be possible, and the computational cost of the post-processing is expensive, especially considering once again the size of the typical measurement volumes.

2.2.2. Large-scale volumetric PIV

As previously explained, the measurement of 3-component volumetric flowfields has been a long-term goal of the PIV research community. While tomographic provided a solution to this problem, its performance is still limited by its small measurement volumes and the computational effort needed to retrieve that information.

Extensive work has therefore been directed to develop a PIV measurement technique that can provide large-scale volumetric measurements. An answer to this need appeared a few years ago in the form of a robotic Coaxial Volumetric Velocimeter, which is the technique that will be used in this thesis work.

This section provides an overview of the main technological developments that have made possible this revolutionary technique, of which the most important are the following:

- Helium-Filled Soap Bubbles as flow tracers.
- Lagrangian Particle Tracking: Shake the box.
- Coaxial Volumetric Velocimeter and robotic manipulation.

Helium Filled Soap Bubbles as flow tracers

The choice of flow tracers to be used for PIV measurements is determined by 2 main factors:

- Mechanical properties
- Light-scattering properties

The mechanical properties are usually quantified in terms of what is known as the slip velocity, which is the difference between the flow velocity U and the velocity of a particle immersed in that flowfield V. The formulation of the slip velocity for small particles can be written as (Raffel et al. [53]):

$$U_{slip} = U - V = -\frac{d_p^2(\rho_p - \rho_f)}{18\mu}\frac{dU}{dt} \tag{2.3}$$

where d_p is the diameter of the tracer particle, ρ_f and ρ_p are the densities of the fluid and the tracer material respectively and μ is the dynamic viscosity of the fluid. A good tracer particle should therefore have the smallest slip velocity possible. Looking at the previous equation, this can either be achieved by neutrally-buoyant particles ($(\rho_p - \rho_f) \ll 1$) or by minimizing the particle diameter d_p. Another variable that is commonly used for the mechanical characterization of tracers is the particle response time defined as

$$\tau_p = d_p^2\frac{\rho_p - \rho_f}{18\mu} \tag{2.4}$$

This variable basically tells how fast the tracing particles react to changes in the flowfield, and thus the interest is to minimize it.

On the other side, the light-scattering properties of the particles must also be taken into account. These properties are a function of the particle diameter, their shape and the ratio between the refractive index of the particle and the surrounding fluid. An intuitive way to quantify the scattering efficiency of a particle is the so-called scattering cross section:

$$C_S = \frac{P_S}{I_0} \tag{2.5}$$

where P_S is the total scattered power and I_0 is the laser intensity that illuminates the particle. This figure was defined by Melling [48], who also showed that this scattering cross section increases with the size of the particle.

It is therefore clear that finding a good tracing particle implies finding a compromise between its light-scattering properties and its mechanical properties. This is not very complex in liquid flows, where finding

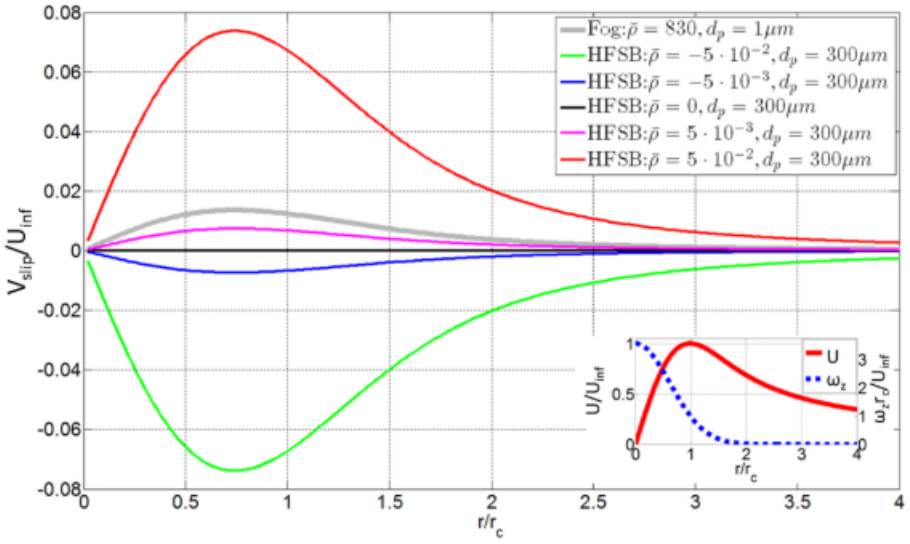

Figure 2.9: HFSB slip velocity compared to standard fog slip velocity for a Lamb-Oseen vortex. Reproduced from Caridi [12] and Scarano et al. [59].

neutrally buoyant particles of large enough sizes to be imaged is not difficult. On the other side, flow seeding in gas flows is much more delicate and solutions have historically relied on the atomization of certain liquids (DEHS, olive oil) and metal oxide powders (TiO_2, Al_2O_3 with particle sizes ranging from $0.5\mu m < d_p < 10\mu m$.

These particles provide a good solution for planar PIV measurements, where the laser beam used for illuminations is expanded into a laser sheet meaning that the illumination power drop as a function of the distance to the source is not too big. However, when expanding the laser beam into a cone for volumetric measurements, the light intensity drops as (Schneiders et al. [63]):

$$I_p \propto \frac{1}{z^4} \tag{2.6}$$

being z the distance to the light source. This is a downside with respect to planar illumination where the intensity drop is proportional to z^2, and the drop in volumetric light intensity proves to be too high for the particles mentioned previously, which are not large enough to be imaged in a volume.

This is where Helium-Filled Soap Bubbles (HFSB) appear as an alternative. Firstly introduced for PIV measurements by Bosbach et al. [9], they consist on bubbles of a special soap with high surface tension (referred to as Bubble Soap Fluid or BFS) filled with helium. Their use for wind tunnel experiments was studied by Scarano et al. [59], and their main advantage is that they offer the possibility to generate large bubbles (in the order of 200-400 μm) that are neutrally buoyant thanks to the introduction of helium, resulting in good tracing as reported by the previous study, with a response time of the particles of $\tau_p \sim 10\mu s$. Figure 2.9 shows the mechanical characterization of HFSB of different properties (as a function of particle diameter d_p and normalized density difference $\overline{\rho} = (\rho_p - \rho_f)/\rho_f$) in the test case of a Lamb-Oseen vortex, showing almost null slip velocities for the lowest normalized densities.

The use of HFSB presents, however, some important challenges in terms of their production. Their use for wind tunnel experiments requires the ability to produce bubbles at a consistent, high-enough rate. The generation of individual bubbles normally relies on nozzles with coaxial channels of air, BFS and helium. In order to seed large enough areas in wind tunnels, some researchers like Caridi [12] have developed rake-like devices that make use of several of these nozzles. The typical geometry of a HFSB nozzle and a sketch of a rake device for the seeding of large areas can be seen in Figure 2.10.

Lagrangian particle tracking. Shake the Box

The next development that has made large-scale volumetric measurements possible is the advancement in tracking algorithms.

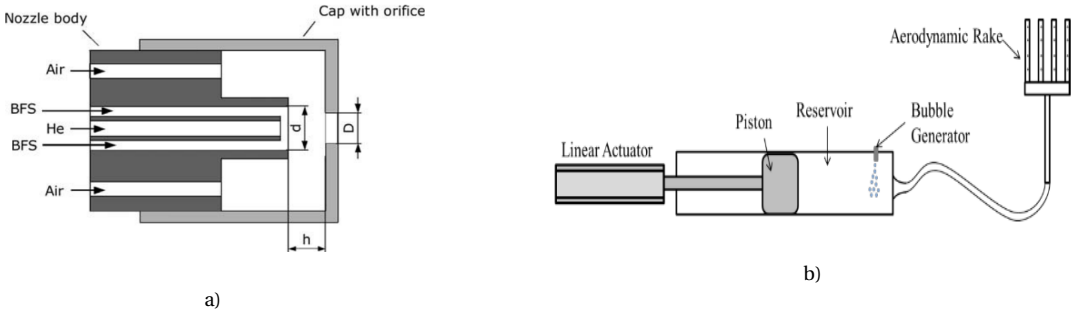

Figure 2.10: a) Example geometry of an HFSB nozzle. Reproduced from Bosbach et al. [9]. b) Aerodynamic rake for HFSB seeding. Reproduced from Caridi [12].

Tomographic PIV uses the aforementioned MART algorithm to reconstruct the light intensity distribution in 3D space from the 2D images from the cameras, and then uses cross-correlation between 2 consecutive volumes to compute the 3D velocity field. As explained previously, the reconstruction of the entire volume is a computationally expensive procedure that compromises the efficiency of this approach for large volumes, making it not suitable for the purpose of large-scale volumetric PIV.

The alternative approach is to reconstruct the position of individual particles in space instead of the entire volume, in what is known as Particle Tracking Velocimetry or PTV. In theory, it offers several advantages such as the lower computational cost and the higher spatial resolution, since the information comes from tracking individual particles instead of computing the average over a volume as in the cross-correlation approach. On the other side, PTV is limited by the amount of particles it can track simultaneously.

The idea of PTV is to perform the detection of the particles in the 2D images of each camera first, to then use that information to triangulate the position of the particle in space. This is what is known as the detection step in which the particles are positioned in 3D space without tracking them yet. This detection step is what limits the performance of classical triangulation approaches in flows with high-density seeding, where due to the overlapping of several particles along the lines of view of the cameras leads to the false detection of particles (known as *ghost* particles). A particle density/concentration measure commonly used is the particles-per-pixel or ppp, which in the first research works in the field of PTV was limited to around 0.001 - 0.005ppp such as the case of Maas et al. [45]. While these concentrations are useful for the evaluation of some Lagrangian statistics, higher concentrations of the order of 0.01ppp are needed for the full-field characterization of 3D flowfields. The solution to this limitation appeared in the work of Wieneke [75], through what is known as Iterative Particle Reconstruction. The details of this reconstruction technique are detailed in the following subsection.

Iterative Particle Reconstruction

Iterative Particle Reconstruction (IPR) is a particle reconstruction technique introduced by Wieneke [75]. The algorithm starts with a 2D particle detection in the camera images and then uses standard 3D triangulation to get a first estimate of their position in space. The novelty is that this 3D position is then used to reproject the particle position on the camera images and compare the resulting images to the original ones, which allows to iteratively fine-tune the 3D position of the particle.

The number of iterations can be increased in order to improve the positioning accuracy at the cost of a higher computation time. IPR also needs an accurate spatial calibration (calibration errors of the order of 0.1px) to deliver the expected results. For this, the use of a Volume Self Calibration is recommended according to Wieneke [74].

Shake the Box

Iterative Particle Reconstruction opened the possibility of reconstructing the 3D position of particles in high seeding density flows. However, even by applying this technique at every single time step of a measurement, the positioning information remains unrelated to time, meaning that particles are not being tracked and the flow velocity is still not resolved. An efficient tracking algorithm to answer this need was introduced by Schanz et al. [62]. It is commonly known as Shake The Box and it is the state of the art technique for particle

tracking in aerodynamic measurements.

This is a particle tracking algorithm that makes use of IPR during the first steps of the tracking. However, after sufficient time steps, it starts using the positioning information of previous steps to get a first guess of where a particle will be in the next one, thus avoiding excessive use of IPR and saving significant computation time.

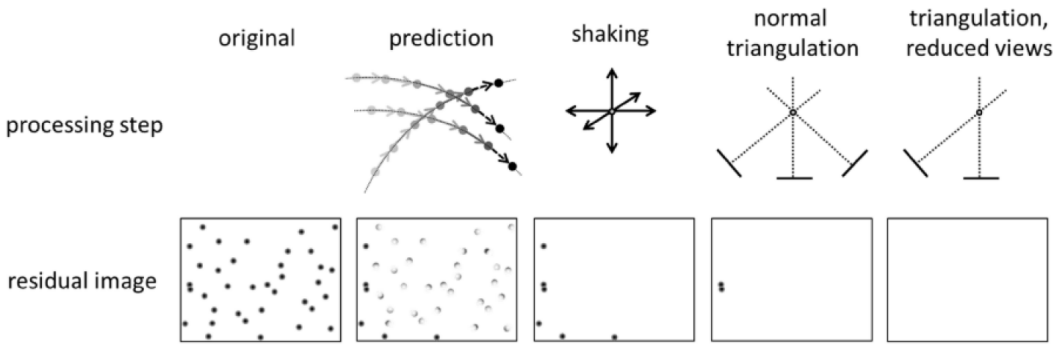

Figure 2.11: Illustration of the steps involved in a single time-step of the converged phase of the Shake-The-Box algorithm. Reproduced from Schanz et al. [62]

The algorithm consists of 3 main phases, namely:

1. **Initialization:** In this phase no previous tracking information is available for the particles. For the first timesteps, the tracking therefore relies on detecting the particles through IPR and then matching them between timesteps (usually the first 4 timesteps) in order to initialize the tracks. This pairing between frames can be done through a simple search radius algorithm.

2. **Convergence:** Once the tracks are initialized, the information from previous timesteps is used to predict the position of the particle in the next timestep by means of a Wiener filter for extrapolation. This is a first guess which will closely match the real position of the particle. In order to further optimize this position, the algorithm "shakes" the particle in space and reprojects it to each of the camera image planes by means of an OTF in a similar way to the IPR algorithm. This shaking is an iterative process which once again aims to minimize the image residual.

   At the same time and in parallel to the tracking of existing tracks, the algorithm must also start tracking new particles entering the measurement volume and be able to detect and delete ghost particles. The steps of the Shake the Box algorithm during the converged phase are depicted in Figure 2.11.

3. **Converged state:** The converged state is reached when the number of tracked particles stays approximately constant. This means that, assuming a constant seeding efficiency, the particle tracks end when the tracers leave the measurement volume, but that loss in particle count is compensated by new particles entering the domain.

After running this algorithm the result comes in the form of particle tracks inside a volume, that is, in Lagrangian format. While this is useful and insightful information, the computation of statistics and/or the identification of coherent structures in the flowfield requires the transformation of the results into a regular grid. This problem was tackled by Agüera et al. [2] by dividing the measurement volume into cells/bins, and reconstructing the velocity inside those cells by using the information of the tracks of the particles that cross that cell. The aforementioned paper explores several reconstruction techniques for this purpose, ranging in complexity from a simple top-hat filter to a more sophisticated polynomial fit.

Robotic Volumetric PTV

Once the problems of how to seed large flowfield volumes and how to track particles in those volumes have been solved, the only challenge left to be addressed is the versatility of the measurement technique.

In order to run the Shake the Box algorithm one must first obtain the source images with a set of hardware similar to that of tomographic PIV, which includes several cameras and laser illumination. As discussed in section 2.2.1, one of the limitations of tomographic PIV comes precisely from the hardware setups that are needed for it, which require significant optical access and are not very mobile.

This was addressed by Schneiders et al. [63] who developed a compact multi-camera imaging system with coaxial illumination named Coaxial Volumetric Velocimeter. The system features 4 cameras in a coaxial arrangement as shown in Figure 2.12, as well as laser illumination along the same axis in the form of a laser cone, in contrast to the typical PIV approaches where illumination and images is done in clearly differentiated directions. This illumination approach ensures that the laser covers the entire field of view of the cameras, and it is achieved by directing the laser beam from a high-speed laser to the CVV probe by means of a carefully aligned optic fiber.

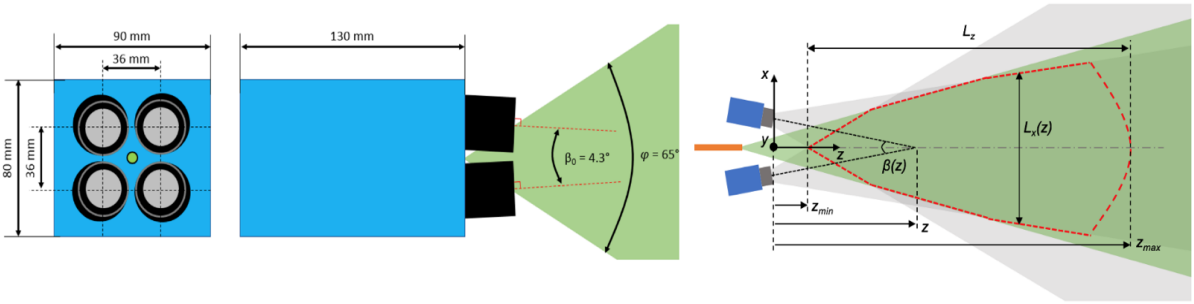

Figure 2.12: Sketch of the Coaxial Volumetric Velocimeter probe, featuring a low tomographic aperture angle β. Reproduced from Schneiders et al. [63].

While allowing for a higher compactness of the setup, the use of a low tomographic aperture angle in the camera arrangement has the consequence of increasing the uncertainty in positioning of the particles along the axis of the CVV probe (normally referred to as the z axis). The proposed CVV system uses a tomographic aperture angle of 4.3°, while the ones used in tomographic PIV experiments is of the order of 40 to 60°. As explained by Schneiders et al. [63], the reconstructed particle size along the other two axes (x, y) depends on the particle image size:

$$d_x = d_y = \frac{d_\tau}{M} \tag{2.7}$$

and the particle positioning uncertainty is proportional to the particle image size:

$$\epsilon_x = c_\tau d_\tau \tag{2.8}$$

where c_τ is a coefficient that accounts for the uncertainty in determining the particle image center. On the other side, the particle image size along the z axis and the positional uncertainty are given by

$$d_z = \frac{2}{\beta} d_x \tag{2.9}$$

$$\epsilon_z = \frac{2}{\beta} \epsilon_x \tag{2.10}$$

This is a significant result and it is something that must be taken into account when positioning the CVV probe. Knowing that there exists a "weak axis", the probe should be positioned in such a way that the axis with the maximum positional uncertainty is aligned with the least relevant flow velocity component. As a reference figure, some typical values of uncertainty for the CVV system are $\epsilon_x = \epsilon_y \sim 0.1$ mm and $\epsilon_z \sim 1$ mm.

The positioning of the CVV probe is another of the main novelties introduced by Schneiders et al. [63]. Taking advantage of the compactness of the CVV probe, it is mounted on a Universal Robots UR5 collaborative robot arm which has a reach of 0.85 m from its base. This choice motivates the denomination of this

technique as Robotic PIV/PTV, and it allows to divide large measurement domains into several sub-volumes that can be quickly and automatically swept by the robot arm as well as the access to areas of difficult optical access.

The first application of the robotic PIV system to a large-scale wind tunnel campaign is reported by Jux et al. [35], who studied the flowfield around a 1:1 scale replica of a professional cyclist by merging several sub-volumes such as the ones shown in Figure 2.13 and mapping them onto a common reference frame. This allowed the detection of some relevant and insightful large scale features of the flowfield such as the vortex structures shown in the aforementioned Figure.

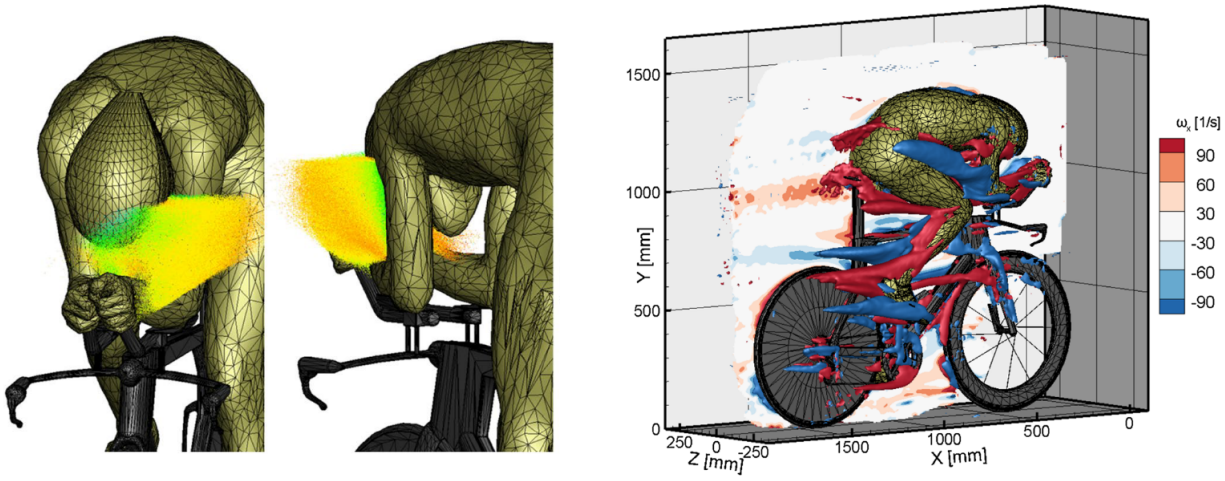

a) b)

Figure 2.13: a) Example of a sub-volume of the flowfield around the cyclist replica. b) Visualization of vortex structures by vorticity contours. Reproduced from Jux et al. [35].

2.3. Potential of Robotic PIV for aeroelastic research

The work of Schneiders et al. [63] and Jux et al. [35] showcased the big potential of the robotic PIV technique, triggering several lines of research at TU Delft aimed at extending the capabilities of the system.

To start with, the study by Giaquinta and Sciacchitano [28] focused on flow topology by using robotic PIV to study the wake of the Ahmed body in straight ahead and crosswind conditions. The study was steady and done at low speeds.

The jump to unsteady measurements was performed by Martinez et al. [47] who conducted phase-averaged measurements of the wake of the DelFly II flapping Micro Air Vehicle, while the possibility of conducting measurements at high speeds was explored by Saredi et al. [56] by implementing a new acquisition technique based on a multi Δt exposure approach. This work showed that measurements can be conducted at velocities of the order of 20 m/s. Measurements at higher speeds are also possible with the STB tracking method as reported by Novara et al. [51] and as advertised by the manufacturer of the hardware (LaVision [40]).

These studies showed that a wide range of flowfields can indeed be studied by using robotic PIV. After this, the main lines of research moved into the direction of recovering load information from robotic PIV measurements, that is, recovering the pressure fields. The computation of pressure from PIV is an extensive field of research, conveniently summarized by Van Oudheusden [70]. In its basic principles, extracting pressure from PIV relies on using the velocity field measured by PIV to compute the pressure field based on the momentum equation of the Navier-Stokes equations. The research on pressure reconstruction techniques applied to volumetric data obtained from robotic PIV is led by the work of Jux, published in Jux et al. [34] and Jux et al. [36] showing its application to the case of the pressure field around a sphere and around generic geometries such as the flowfield around a cyclist.

The capability of the robotic PIV system to resolve the aerodynamic side of a problem is therefore proved, and in combination with another optical method for structural measurements, it could become the first uni-

fied system capable of fully resolving an aeroelastic problem. The proposed approach at TU Delft and in this thesis is to use the marker tracking technique for this purpose: the markers will be imaged together with the HFSB tracers and processed separately in order to characterize the structural and aerodynamic response. This method has already been explored by Mitrotta et al. [49] in the case of a flexible flat plate with promising results, and it will be continued in this thesis for the case of a flexible composite wing.

2.4. Research questions and objectives

A review of relevant literature has shown that there exist several measurement techniques that can be applied in aeroelastic experimental campaigns to measure the dynamics of a structure as well as the corresponding flowfield. However, very few efforts can be found in literature in which techniques from both sides have been used to fully characterize an aeroelastic problem and, when they have been combined, the resulting setups have been complex and their application seems to be limited to specific cases and small geometries, lacking versatility.

This thesis proposes the use of the state-of-the-art aerodynamic measurement technique of Robotic PIV capable of retrieving 3D flow information in large measurement volumes. This will be used in combination with the point tracking principle of photogrammetry for structural measurements by placing reflective markers on the surface of the test model, resulting in a single imaging system which will track both the flow and the structure. The proposal will be applied to the classical aeroelastic problem of gust encounter by a flexible wing, which is still a relevant case of research in Aeroelasticity. In order to do this, the following research questions and objectives have been defined.

2.4.1. Research Questions

1. Can a robotic PIV system be used to perform simultaneous, non-intrusive and instantaneous aerodynamic and structural measurements in a large-scale aeroelastic experiment?

   (a) Is it possible to conduct aeroelastic measurements in a static case?

   (b) Is it possible to conduct aeroelastic measurements in a dynamic case (gust encounter)?

   (c) Is marker-tracking a suitable approach to conduct structural measurements using the CVV system?

   - Can structural accelerations be recovered from marker-tracking data?
   - Can structural strains be recovered from marker-tracking data?

   (d) Can unsteady aerodynamic measurements be conducted using robotic PIV and a phase-averaged approach?

   (e) Is it possible to use data acquired with robotic PIV to retrieve information about the different kinds of loads at play during an aeroelastic interaction?

2. What are the accuracy and uncertainty of this system in comparison to traditional measurement approaches used in aeroelastic experiments?

   This question aims to determine whether this approach could substitute or at least become an alternative to the traditional techniques used in aeroelastic experiments mentioned in the literature review.

   (a) Are the measured unsteady flowfields compliant with the reconstructed surface of the structure and the estimated loads?

   (b) What is the accuracy of the acceleration measurements obtained with robotic CVV with respect to the validation measurements?

   (c) What is the accuracy of the strain measurements obtained with robotic CVV with respect to the validation measurements?

   (d) What is the origin of the discrepancies that are found, if any?

   (e) What are the main strengths and limitations of robotic CVV as a measurement system for experimental aeroelastic campaigns?

2.4.2. Research Objective

The research objective of this proposal is *"Develop a framework for the use of the robotic PIV system as a tool for integrated, simultaneous and coherent aerodynamic and structural measurements by means of an experimental campaign on a flexible wing exposed to discrete and continuous gust excitations"*. Completing this objective would give a proof-of-concept of the proposed technique which, if validated, could become a powerful alternative to traditional measurement systems used for aeroelastic tests in industry and Academia.

This research objective will be achieved through the following research framework:

1. Expand the understanding of the robotic PIV system and its capabilities by using it on a large-scale, unsteady case.
2. Obtain structural and aerodynamic raw measurements on the flexible wing using robotic PIV, by means of an experimental campaign specifically designed for this purpose.
3. Transform the raw aerodynamic data into meaningful flowfield information, namely:
    - Velocity fields will be computed using the Particle Tracking Velocimetry principles, implemented in the commercial software *DaVis 10*.
    - The steady and unsteady aerodynamic loads will be estimated based on the circulation of the flowfield around the wing.
4. Develop a method to provide full field structural data from point-tracking information acquired with the PIV system:
    - Develop a methodology to extract acceleration measurements from point-tracking data.
    - Develop a methodology to extract strain measurements from point-tracking data.
5. Assess the performance of the developed methodology by comparing the structural results obtained with it to independent measurement systems, namely the accelerometers, optic strain fiber and force balance.
6. Combine the aerodynamic and structural measurements to evaluate their compatibility and the overall performance of the system as a combined measurement system.

3

Experimental Setup and Procedures

This chapter describes the main aspects of the experimental campaign conducted to answer the research questions that motivate this thesis.

First of all, the wind tunnel facilities where the experiment is conducted are presented in Section 3.1. The main characteristics of the flexible wing used as a test object are discussed in Section 3.2 and the robotic PIV system and its main components are described in Section 3.3. Other measurement systems, listed in Section 3.4 were also used to provide a validation for the robotic PIV structural measurements. Finally, Section 3.6 discusses the acquisition strategy chosen to perform the measurements and the motivation behind that choice.

3.1. Wind Tunnel

The investigation has been conducted in TU Delft's Open Jet Facility (OJF), which is a closed-loop, open test section wind tunnel with an octagonal exit of 2.85x2.85 m^2 and a 3:1 contraction ratio. The tunnel is powered by a 500 kW electrical engine which drives a fan that can provide air speeds of up to 35 m/s. The nominal turbulence intensity of the tunnel is 0.5%, although this value will likely be higher during this experiment due to the presence of the PIV seeding system and the gust generator. Previous work by Giaquinta and Sciacchitano [28] reports an increase of the turbulence level up to 0.8% when the the PIV seeder is placed in the settling chamber of the wind tunnel, as is the case in this study.

The motivation for the use of this facility is straightforward considering the scale of the experiment to be conducted. The dimensions of the model and the large amount of equipment needed for the measurements (gust generator, PIV system etc.) require a large test section which the OJF satisfies, since its test section is embedded in a room with a width of 13 m and a height of 8 m. In addition, the gust generator - to be described in Section 3.5 - has been designed specifically for this facility.

3.2. Flexible Wing Model

The test object of the experiment is an unswept flexible wing with a span of 1.75 m and a NACA 0010 airfoil profile with a constant chord of 25 cm. The wing has been manufactured by the Aerospace Structures & Materials group at the Aerospace faculty at TU Delft, and it has been specifically tailored to exhibit an optimal behaviour for the study of fatigue degradation under the conditions that can be achieved at the OJF with the gust generator.

The wing is made out of carbon fiber reinforced epoxy (Hexcel 8552 IM7) unidirectional tailored laminates. Its inner structure is formed by two spars and thirteen ribs, and the outer skin is divided into three spanwise regions of equal length, where each has its own laminate properties (orientation and thickness). The properties of those laminates were determined through an optimization process driven by an objective function which tries to both minimize the weight of the wing and to maximize the wing tip displacement

while satisfying certain safety margins. This displacement is also favoured by the addition of a wing tip mass of 400 g which lowers the natural frequency of the wing, placing it within the range of excitation frequencies achievable with the gust generator.

To allow the clamping of the model to the force balance in the wind tunnel, a 5 cm section with a solid aluminium block is added to the bottom of the wing. This results in a final model which is 1.80 m long, although for the purpose of this investigation the bottom 5 cm are considered to be perfectly rigid and are excluded from the measurements. The inner structure of the wing with the presence of this block can be observed in Figure 3.1

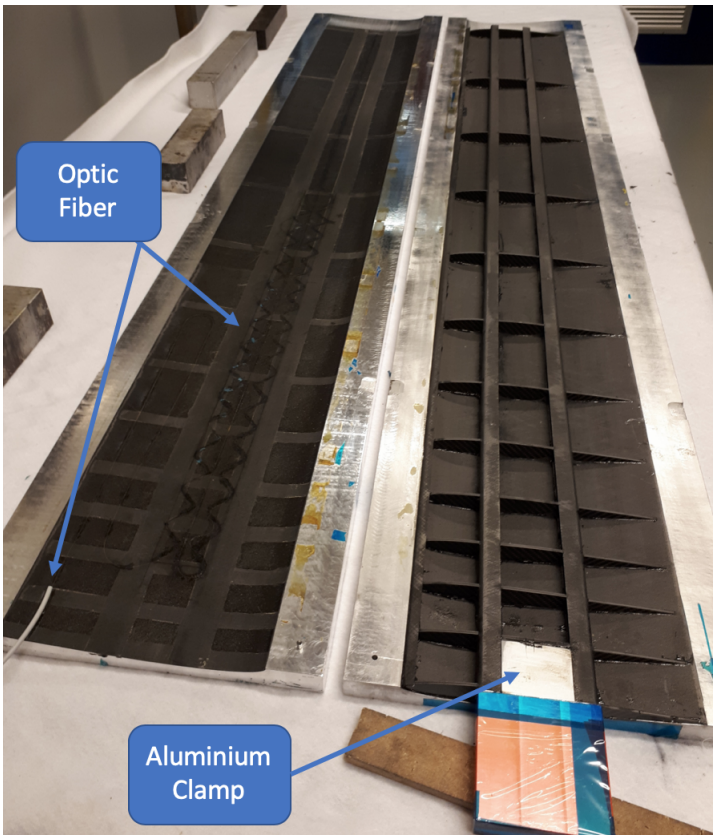

Figure 3.1: Picture of the wing inner structure before the bonding of the two halves. The layout of the optic fiber and the aluminium block used for the clamp can be observed.

Property	Units	Value
Chord	[mm]	250
Height	[mm]	1750
Weight	[g]	2369
Weight - Aluminium Block	[g]	928
Grid Spacing - X	[mm]	30
Grid Spacing - Z	[mm]	30
Marker Diameter	[mm]	1.5

Table 3.1: Table summarizing the main properties of the wing model

Finally, the model was also fitted with a zig-zag strip running along the span of the wing on both sides of the model. This is done to trigger the transition of the boundary layer from laminar to turbulent and avoid undesired effects such as laminar separation bubbles. The chordwise locations of the tape were 5% and 65% for the suction and pressure side respectively, and the thicknesses of the tape were 0.2 mm and 0.5 mm.

3.2.1. Marker grid

A central part of this thesis consists on performing structural measurements with the robotic PIV system. This is done by imaging reflective markers placed on the surface of the wing which are then tracked in time and space.

A rectangular grid of circular markers is imprinted on the surface of the wing model for this purpose. The markers have a diameter of 1.5 mm and are spaced equally every 30 mm both horizontally and vertically. The choice of these dimensions is motivated by two main reasons:

- The markers should be small enough so that they can be tracked with the Shake-The-Box software and to ensure that a sufficient amount of the field of view of the cameras is left "marker-free" so that the HFSB flow tracers can still be tracked.With respect to the marker diameter in particular, previous work by Mitrotta et al. [49] done on a similar case shows good results for the chosen dimension of Ø= 1.5 mm.
- The marker grid should be dense enough to provide local information about the deformation of the wing and to ensure that enough markers can still be imaged even if the structure is moving and some of its sections (and the corresponding markers) fall out of the field of view of the cameras. On the other side, the grid should be sparse enough to once again guarantee that enough field of view is available to image the flow tracers.

The markers are imprinted on the surface of the wing using a laser-cut template which is then spray-painted with white paint. The template is manufactured with a cardboard sheet with a thickness of 0.4 mm so that the resulting template is flexible and can follow the curvature of the wing profile. The marker grid is symmetrically imprinted on both the pressure and suction side of the wing. A sketch of the wing, marker grid and some of its main dimensions is presented in Fig.3.2.

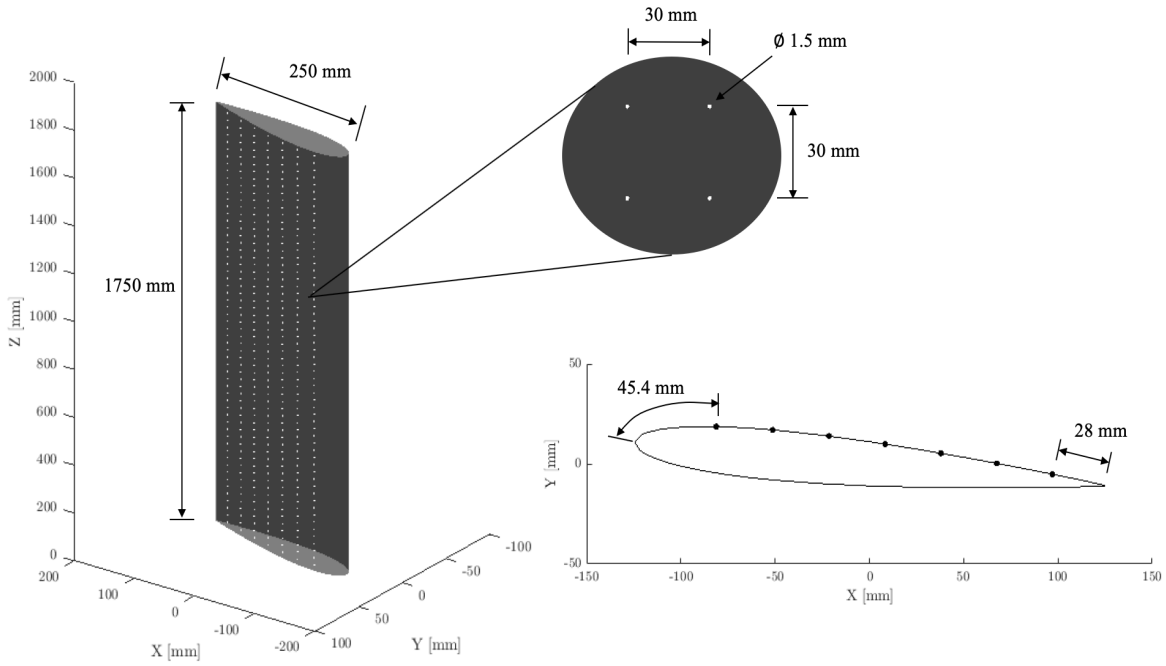

Figure 3.2: Relevant dimensions of the wing and the marker grid. Note that the scaling of the axes on the sketch of the full wing might distort the real spacing between markers.

3.3. Robotic PIV system

This section presents the main measurement system used during the experimental campaign and the protagonist of this study: the robotic PIV system. Each of the main components of the system will be briefly described together with an explanation of their purpose.

3.3.1. Seeding system

As any other PIV system, the robotic PIV system requires the presence of flow tracers to conduct measurements. In addition, due to the large-scale and volumetric nature of such measurements, the seeding of Helium-Filled Soap Bubbles is required in particular because of their mechanical and light-scattering properties. These tracers are normally produced by means of nozzles inside of which air, soap and helium are mixed to generate the bubbles. Some of the properties of the tracers (rate of production, buoyancy etc.) can be controlled by adjusting the flow rates of each of the fluids, which can be done from a control unit designed in-house at the Aerodynamics department of the TU Delft.

The seeding of large areas of the flowfield requires a seeding device with multiple nozzles. In this experiment, a seeding rake also manufactured by the Aerodynamics department is used. The rake is designed to be minimally intrusive on the flow in terms of added turbulence, and it consists of an array of ten vertical wings positioned in parallel. Each wing houses twenty equally-spaced nozzles, such that the exits of the nozzles are aligned with the trailing edge of each wing. With this arrangement, an area of roughly 1 x 0.5 m^2 is seeded under nominal working conditions although these cannot be achieved due to the deterioration of the seeder (blocked/broken nozzles, blocked fluid lines...). This deterioration has been reported in previous works (Ordonez [52]) and in this campaign only a section of approximately one fourth of the total area was working reliably.

The seeder is placed on the settling chamber of the OJF, right before the contraction of the tunnel. This arrangement is the same one used in previous works such as Giaquinta and Sciacchitano [28] or Saredi et al. [56], where it is reported that this is the setup that produces a minimum increase in turbulence intensity. The seeding rake is mounted on a support structure formed by X95 beams which allows for some vertical and horizontal displacement of the rake, needed to achieve good seeding concentrations in all the areas of interest of the model.

3.3.2. Coaxial Volumetric Velocimetry Probe

The key component of the robotic PIV system is the Coaxial Volumetric Velocimetry[1] probe that is used to both take the images of the particles and to illuminate them thanks to its optical arrangement. The probe used in this campaign is the *Minishaker Aero* manufactured by *LaVision*, and it features 4 CMOS[2] cameras housed inside an oval-shaped container designed to minimize the aerodynamic interference of the probe. The cameras are mounted on a low-tomographic angle configuration around a common axis which contains the illumination source. The illumination is achieved by redirecting the laser beam output by the laser to the CVV probe through an optic fiber. The CVV probe also has a special attachment point that can be used to mount it on a UR5 collaborative robot arm which will be discussed next.

Finally, from an operational point of view, the sensor size of the cameras can be modified to change the maximum acquisition frequency. In this campaign, two sensor sizes were used:

- **704 x 540 px** for a maximum acquisition frequency f_{max} = 821 Hz, used for aerodynamic measurements.

- **704 x 636 px** for a maximum acquisition frequency f_{max} = 500 Hz, used in measurements where only markers were captured. The reason behind it is to maximize the number of markers captured in a single recording and to match the acquisition frequency of some of the secondary measurement systems.

[1] Hereafter referred to as CVV
[2] Stands for Complementary Metal Oxide Semiconductor

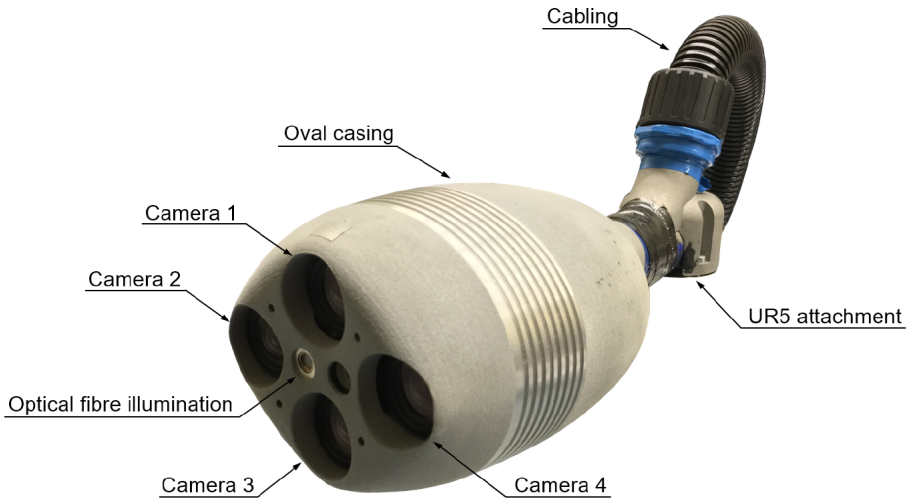

Figure 3.3: *MiniShaker Aero* Coaxial Volumetric Velocimetry probe by *LaVision*. Reproduced from Ordonez [52].

3.3.3. Robot Arm

One of the main features of the robotic PIV system is its versatility when conducting large-scale measurements thanks to its ability to conduct measurements in different locations quickly, automatically and without the need of a new calibration in between them. This mobility is provided by a *Universal Robots - UR5* robot arm, which has 6 degrees of freedom and a maximum reach of 850 mm from its base. This robot is controlled through the *RoboDK* software installed in the acquisition PC, which can simulate the 3D environment around the robot making the positioning of the arm more intuitive.

An important aspect of the robotic PIV measurements is the positioning of data in space. In principle, the PIV data acquired with the CVV probe will be positioned in a reference system which will be dependent on the particular robot positioning and orientation during a measurement, as shown in Fig.3.4 ("Robot Tool" reference frame). On the other hand, when sweeping large measurement domains, the use of a global reference system is preferred. This is a feature available on the *Davis 10* PIV acquisition software, which allows to position all the measurements in the "Robot Base" reference frame by means of an automatic transformation performed using the angular position of each of the robot joints. After that, the data can be moved to any other reference system by knowing the positioning of the robot with respect to the wind tunnel. Finally, in terms of positioning performance the manufacturer of the robot advertises a repeatability of ± 0.1 mm, although this figure will be debated in Section 4.

3.3.4. Illumination source

The light source needed to illuminate the flow tracers is provided by a *QuantronixDarwinDuoNd: YLF* high-speed laser with a wavelength of λ =527 nm, a frequency range of [0.2-10] kHz and a maximum power of 25 mJ. The light beam produced by the laser is focused on the end of an optic fiber through a coupling system mounted on the laser head. The optic fiber is both quite long (4 m) and flexible, allowing for a wide range of motion of the CVV probe mounted on the robot arm, as well as the safe placement of the laser head away from the measurement area. The laser light travels through the optic fiber to the CVV probe where it is expanded into a cone through a set of spherical lenses, which produces a measurement domain that resembles a truncated pyramid.

The laser also needs to be triggered in coordination with the shutters of the cameras, which is done by a timing unit housed inside the acquisition PC.

3.3.5. Acquisition PC & Software

The acquisition PC is another important piece of equipment needed for the operation of the robotic PIV system. On the hardware side, it contains the Programmable Timing Unit used to trigger the cameras and

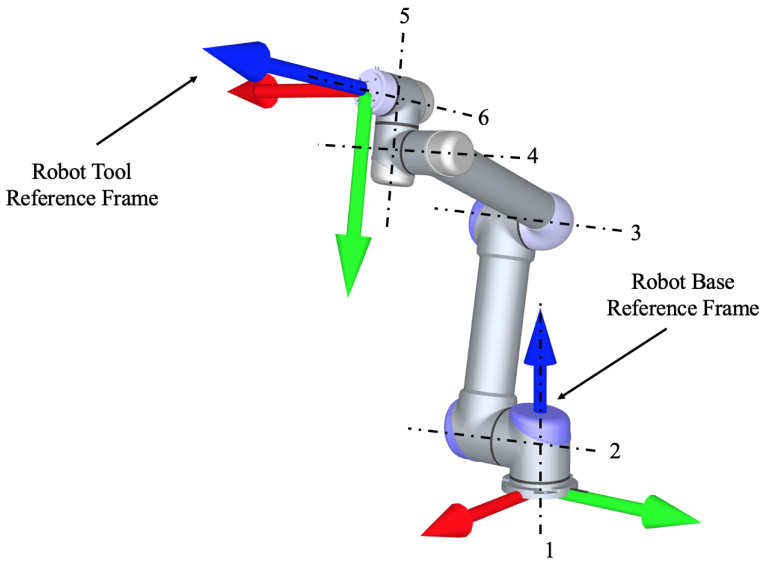

Figure 3.4: Sketch of the *Universal Robots UR5* collaborative robot arm where the 6 different joints and their axes of rotation are enumerated, and the "Robot Tool" and "Robot Base" reference systems are highlighted.

the laser. This unit can also accept external triggers, a feature used extensively in this campaign to conduct simultaneous measurements with the robotic PIV system and other measurement tools. The PC also has 64GB of RAM memory, which limits the maximum number of images that the cameras can acquire during a single measurement run.

On the software side, the acquisition PC contains the *DaVis 10.0.5* program used to set up the PIV acquisitions. This program is coupled with the *RoboDK 3.2* software, which controls the movement of the robot arm. With this arrangement, an acquisition over several measurement positions can be easily automated.

3.4. Auxiliary Measurement Systems

One of the main goals of this thesis is to evaluate the performance of the robotic PIV system with respect to traditional structural measurement systems. It is therefore necessary to conduct a series of validation measurements to make that comparison. Previous work by Mitrotta et al. [49] used a laser vibrometer to validate the tracking of markers with the Shaker-The-Box software and therefore this option is not used in this campaigns. Three other measurement systems were chosen for this experiment:

- Accelerometers
- Optic Fiber
- Force Balance

The purpose of each of them will be briefly discussed next together with some of their performance characteristics.

3.4.1. Accelerometers

Some of the most important aeroelastic interactions are dynamic, which means that there exists a fluid-structure coupling over time. It is therefore needed to prove that the marker-tracking information obtained with the Shake-The-Box algorithm can be used to accurately reconstruct dynamic events.

For this purpose, two *Endevco Isotron Model 65-10* tri-axial accelerometers are used during this campaign. The sensors are provided by the Netherlands Aerospace Centre (NLR) and have a dedicated acquisition system. The accelerometers are located on the top rib of the wing such that they remain housed inside the inner

structure of the wing and that they don't interfere with the flow at the tip of the wing. The devices are positioned along the mid-line of the top rib, at 5 cm and 17.5 cm from the leading edge of the wing respectively. The accelerometer model is shown in Figure 3.5, together with its typical frequency response as advertised by the manufacturer. Some of the most relevant performance characteristics of the accelerometers can be found in Table 3.2[3].

The performance characteristics are listed in Figure 3.5 where it can be seen that its performance deteriorates slightly when approaching the ends of the frequency range of the accelerometers. In addition, Table 3.2 shows that this not only affects the amplitude response, but also the phase response which is guaranteed to stay within ±5° of the real phase only in the 10-1500 Hz range. These facts are particularly important considering that the range of frequencies of the excitations (gusts) used in this campaign will be of 2-6 Hz and thus some error in the measurements can be expected.

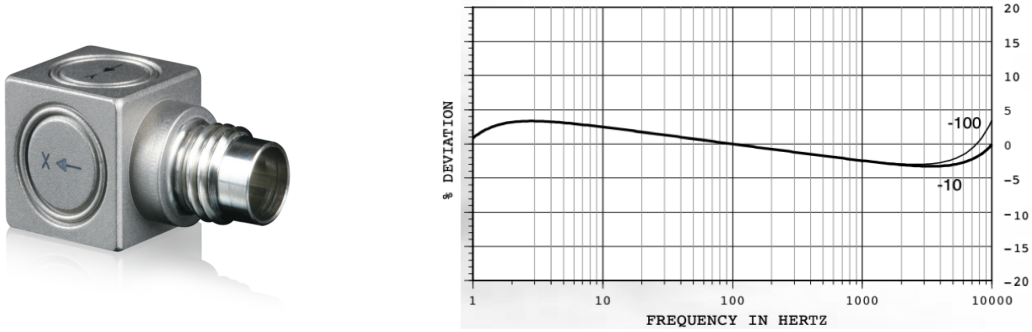

a) *Endevco Isotron Model 65-10* accelerometer.

b) Typical frequency response (Amplitude) of the accelerometer

Figure 3.5: Picture of the accelerometer model used and its typical frequency response. Reproduced from www.endevco.com.

Property	Units	Value
Mass	[g]	5
Number of axes	-	3
Range	g[m/s^2]	50
Typical Voltage Sensitivity	[mV/(m/s^2)]	10
Acquisition Frequency	[Hz]	500
Amplitude Response, 5%	[Hz]	3 - 6000
Phase Response, ±5°	[Hz]	10 - 1500

Table 3.2: Main performance characteristics of the *Endevco Isotron Model 65-100* accelerometer.

3.4.2. Optic Fiber

Another variable of interest in aeroelastic investigations is the strains that the materials suffer when undergoing static or dynamic deformations. These strains can be related to the forces (stress) that the materials must endure and can therefore be used as safety margins that cannot be exceeded in order for a material not to fail. Strains are even more important when using composite materials, due to their typical anisotropy in properties.

In this campaign, strain measurements are conducted using a *LUNA OPT 06006* Optical Backscatter Reflectometer, which uses Rayleigh backscattering to conduct local strain measurements. To use the system, an optic fiber must first be installed inside the model following the line along which the measurement is to be

[3] More information available at `https://buy.endevco.com/ContentStore/MktgContent/Endevco/Datasheet/65_DS_082719.pdf`

conducted. This can be seen on the left-hand side of Figure 3.1, where the optic fiber has been bonded to one of the sides of the wing. The installation shows that the fiber is installed using different kinds of patterns (straight line / zig-zag), but for the purpose of this study only a straight line running from the root of the wing to the 1.65 m height is considered. The chordwise location of the optic fiber is approximately the half-chord position.

In terms of acquisition, the system allows for certain adjustments in terms of spatial and temporal resolution. During this campaign, an acquisition frequency of 500 Hz is chosen which results in a maximal spatial resolution of 2.59 mm. This trade-off between temporal and spatial resolution is imposed by the measurement system technical specifications.

3.4.3. Force Balance

Finally, some of the most important outputs of an aeroelastic campaign are the different loads that the structure experiences. This thesis will also explore the reconstruction of loads from the robotic PIV measurements, and therefore a 6-component force balance is used during the investigation.

The balance serves both as a measurement system and as a support system for the wing during the investigation. The aluminium block on the bottom of the wing is held using a special clamp which is directly connected to the balance. The balance sits on top of a rotating table which can be used to adjust the angle of attack of the wing.

3.5. Wind tunnel setup

The most relevant pieces of equipment needed to conduct the experiments have been listed in the previous sections. As the reader can probably deduct at this point, the use of all this equipment results in a complex experimental setup where lots of different systems need to be properly located and coordinated to conduct the measurements. This section provides an overview of how this has been achieved and what the most important aspects of the complete setup are.

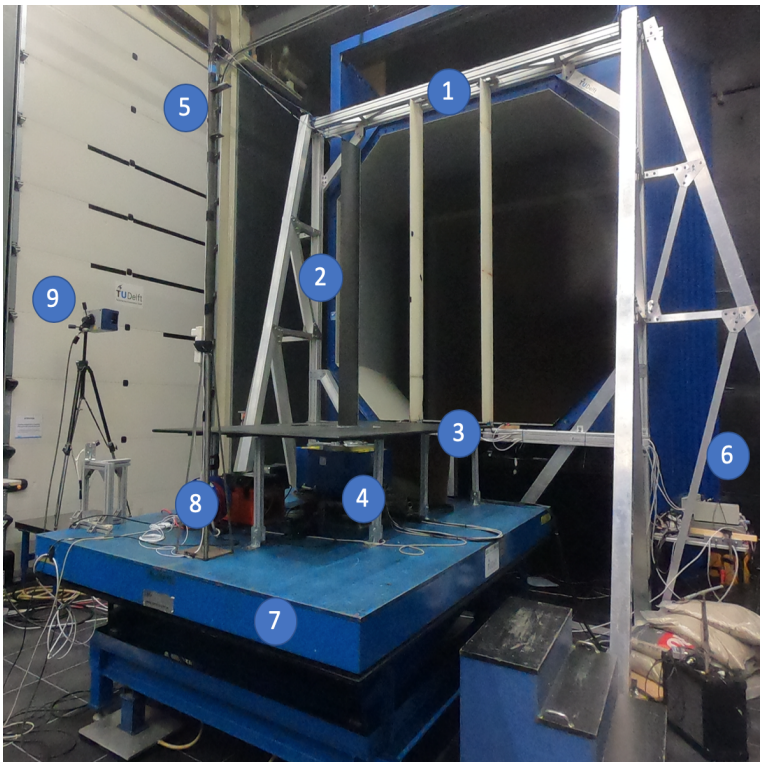

Figure 3.6: Picture of the test section of the OJF, showing the main components of the experimental setup **before** the installation of the robotic PIV system.

To start with, Figure 3.7 offers a general view of the setup before the installation of the robotic PIV system. The most relevant components are numbered, being each of them:

- **1: Gust Generator.**The gust generator is formed by an aluminium structure placed around the octagonal exit of the OJF which serves as a support for the 2 vertical vanes used to generate unsteady flow conditions. The vanes are operated by electrical motors and controlled through a LabView environment. The gust generator can generate both continuous or discrete (1-cosine gusts) of frequencies ranging from 0.5-10 Hz and amplitudes of δ_G = 0-10°. More details about the gust generator and its conception can be found in the work of Lancelot et al. [39].

- **2: Flexible wing model.** Discussed in Section 3.2

- **3: Splitter table.** A plank of (black) wood is used to separate the wing from the clamping system/balance setup. The height of the table is aligned with the bottom of the exit of the OJF, and its purpose is to reduce the aerodynamic interference of the setup in the flow around the wing and in particular, its root section.

- **4: Force balance and rotating table.**. Discussed in Section 3.4.3.

- **5: Accelerometer wiring**. The accelerometers are connected to the acquisition system through a set of wires which need to be routed down from the tip of the wing where the sensors are housed. To minimize aerodynamic interference and to prevent the cables from swinging during test runs, a metallic pole is installed approximately 1 m behind the wing to direct the cables and keep them in place. This pole is removed once the measurements requiring accelerometers are completed.

- **6: Main acquisition system.**This system consisting of a data acquisition module and a laptop is responsible for the operation of the gust generator through a LabView environment, as well as providing the trigger signals needed for the time-synchronization of the different measurement systems.

- **7: Hydraulic table.** Since the exit of the OJF tunnel is not at ground level, the model and some of the equipment pieces are placed on top of a hydraulic table to align them with the air stream of the tunnel.

- **8: Accelerometer acquisition system.** As discussed in section 3.4.1, the accelerometers have a dedicated acquisition system which is also housed under the splitter table. An input trigger is provided to the acquisition box to synchronize the accelerometer signal with the robotic PIV measurements.

- **9: Laser Vibrometer.** Not used in this campaign.

Secondly, Figure 3.7 shows a close-up of the setup while performing a robotic PIV measurement. Some components have been again highlighted, namely:

- **10: Helium-Filled Soap Bubble seeding rake.** As discussed in Section 3.3.1, located inside the settling chamber of the OJF. Not shown in any of the pictures is the control unit used to manage the feed of soap, air and helium to the seeder, as well as the storage containers for helium and soap.

- **11: Robot arm.** Discussed in Section 3.3.3. Mounted on top of a X95 beam support in order to cover the entire span of the wing.

- **12: Coaxial Volumetric Velocimetry probe.** Discussed in Section 3.3.2, mounted at the end of the robot arm.

- **13: Measurement region.** The laser cone coming from the CVV probe is illuminating both the marker grid and the HFSB tracers.

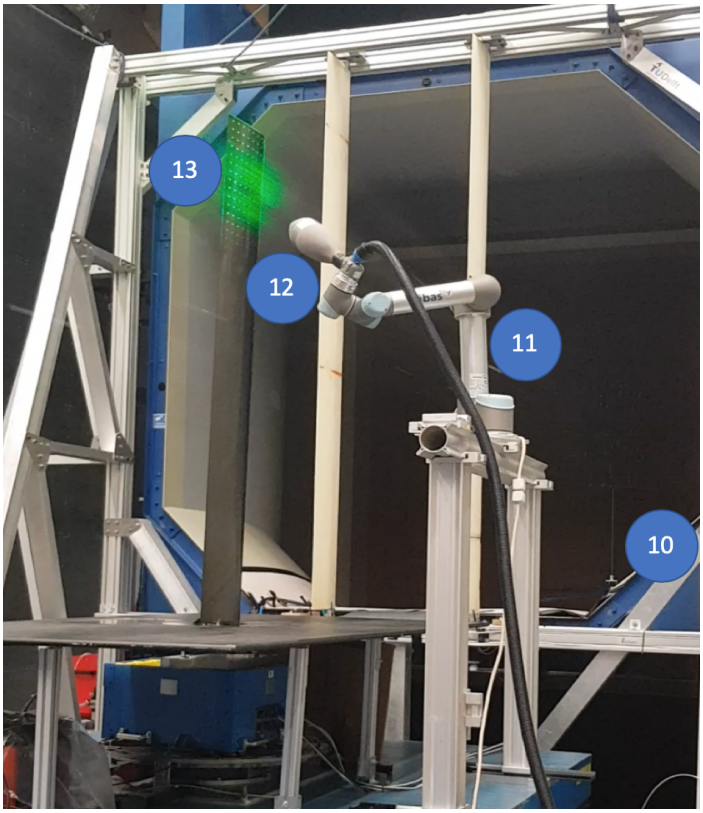

Figure 3.7: Close-up of the setup during a PIV acquisition, showing the main components of the robotic PIV system as well as the aspect of the measurement region.

3.6. Acquisition strategy

The final section of this chapter discusses how the measurements were conducted and what were the test conditions. The experimental campaign took place over the course of a week, of which only 4 days were used for measurements. This justifies the need for a carefully chosen test matrix which needs to produce results capable of answering the research questions and objectives presented in Section 2.4. In practice, this led to the division of the campaign in two main blocks to be presented next.

3.6.1. Measurement Block 1: Structural Measurements

The motivation behind the first block of measurements is to determine how the marker information acquired with robotic PIV compares to traditional structural measurement systems such as the accelerometers, strain fiber and force balance. A variety of static and dynamic test cases are chosen, where the choices of speeds and angle of attack of the wing (α_w) are made based on knowledge about the loads that the model can withstand without failing.

A simplified version of the test matrix of this measurements block is presented in Table 3.3. Even though it is not listed, every single acquisition of data was accompanied by a robotic PIV measurement where no HFSB seeding was used and only the marker grid was illuminated and captured. Some of the most important practical aspects of the measurements are:

- With the robotic PIV system sampling at 500 Hz, a larger field of view can be selected for the cameras. However, even in this configuration, only individual sections of the wing of approximately 30 cm in height can be captured in a single measurement and therefore several acquisitions are needed to cover the entire span of the wing. A total of 9 consecutive spanwise volumes are defined in the robot control software for this purpose.

  An important aspect is that, in dynamic cases, this means that the selected test case must be repeated

once for every single volume. In doing so, it is assumed that there exists a good level of repeatability of the experiment and that there are no changes in the structural response of the wing model due to fatigue for example.

- The strain measurements are acquired at a frequency of 500 Hz over the course of 5 seconds.

- The accelerometer measurements are acquired at 500Hz. Due to the need to repeat the dynamic measurements once per PIV view, several measurements are taken for the same event and then averaged.

Test Conditions	Flow Speed [m/s]	α_w [º]	Excitation Frequency [Hz]	Gust Amplitude [º]	Accelerometers	Strain Fiber	Force Balance
Wind off	0	5	-	-	-	-	-
	0	7	-	-	-	-	-
Static	14	5	-	-	-	Yes	Yes
	14	7	-	-	-	-	Yes
	24	5	-	-	-	Yes	Yes
1-Cosine Gust	14	5	3	10	Yes	-	Yes
	24	5	3	10	Yes	-	Yes
Sinusoidal Frequency Sweep	14	5	0.5 - 6 Hz	5	Yes	-	Yes

Table 3.3: Simplified test matrix of the first measurements block of the experimental campaign. All the listed cases have their own corresponding robotic PIV acquisition.

3.6.2. Measurement Block 2: Aerodynamic Measurements

The second block of measurements is dedicated to the acquisition of flowfield information combined with marker tracking as shown in Figure 3.7, therefore needing the use of the HFSB seeding system unlike in the first block.

Due to time constraints, only one section of the wing located at approximately 80% of the span is measured. The field of view of the PIV system is adjusted (reduced) to increase the acquisition frequency to 821 Hz, a requirement in order for the tracking of the flow tracers to work reliably. In addition, three different views, shown in Figure 3.8 are defined along the chord of the chosen section of the wing in order to capture the entire flowfield. Finally, the PIV measurements are first conducted on the suction side of the wing, after which the robotic PIV system is moved to the opposite side of the hydraulic table and positioned such that the setup is mirrored with respect to its previous location. The three chordwise views ($V1_s$, $V2_s$, $V3_s$) defined previously are used again to capture the pressure side of the flowfield ($V1_p$, $V2_p$, $V3_p$) .

Additionally, as also shown in Figure 3.8, the orientation of the CVV must be chosen carefully. In the problem at hand, there exist two main dimensions of interest: the main flow direction (aligned with the X axis as shown in the figure) and the main oscillation direction (aligned with the Y axis). On the other hand, it is known that the CVV probe has a limitation in terms of positioning precision along its main axis due to the low tomographic aperture angle of the cameras. In practice, this means that during the acquisition the "weak" axis of the CVV probe must not be aligned with the main directions of interest in order to reduce the measurement uncertainty of both the markers and the HFSB tracers. In this campaign, the robot is positioned such that the CVV probe is tilted and its main axis is aligned mainly with the vertical axis of the reference system.

The measurements are first conducted for a steady state condition described in Table 3.4.

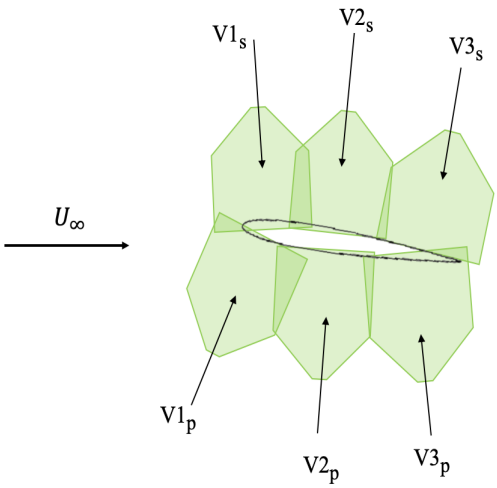

a)Sketch of the PIV views ($V1_s$-$V3_s$) and their correspondent symmetrical ones ($V1_p$ - $V3_p$) chosen for the measurement of the flowfield

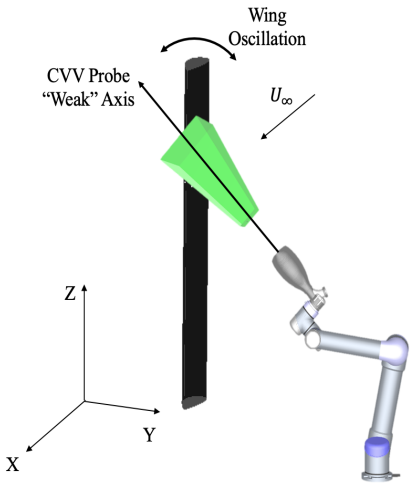

b)Relative positioning between the CVV prove, the wing model and the main flow direction.

Figure 3.8: Sketches of the PIV views and the positioning of the robotic PIV system during the measurements.

Property	Value
Flow Speed [m/s]	14
AOA [º]	[5, 7]
Sampling Frequency [Hz]	821
Acquisition Time [s]	18.3
Number of images	15000

Table 3.4: Acquisition settings for static robotic PIV measurements.

Secondly, measurements of the selected dynamic cases are taken. The acquisition of unsteady PIV data makes necessary the recording of several cycles of each event to phase-average them and achieve a high enough particle concentration for the posterior binning of the data (transformation from Lagrangian information to structured volumetric grid).

The most important dynamic case is the continuous gust excitation, where the frequency of the gust is set to 2 Hz and its amplitude to $\delta_G = 5°$[4]. The selected frequency implies a reduced frequency of $\kappa = 0.11$ and therefore unsteady effects should be relevant. A larger amplitude of the gust could not be considered due to the properties of the laminate on the pressure side of the wing, prone to debond when placed under compression. Finally, in this campaign only the purely oscillatory interaction is of interest and the transient period between the wing being at rest and oscillating periodically is discarded. The acquisition process works as follows:

1. The robot is positioned in the position of interest (see views in Figure 3.8).

2. A first check is conducted to ensure that the positions of the robot and the HFSB seeder are such that good seeding concentration is achieved throughout the interaction. The robot stays fixed in position during the entire measurement and therefore it needs to be on one side far enough from the wing to

[4]As measured by the deflection of the gust generator vanes δ_G

reduce aerodynamic interference but also close enough to illuminate the flow tracers when the wing is at its furthest point of oscillation.

3. The gust generator is started and set to provide the continuous gust excitation for a total time of 80 seconds. Of those, the first 40 seconds are not recorded and are left to ensure that a purely oscillatory state is reached and to perform some last checks before the acquisition of the data. At t = 40s, the gust generator controller triggers the robotic PIV acquisition and images are recorded for the remaining 40 seconds. This results in an image set containing 32840 images and 80 cycles of the interaction. The vane angle signal from the gust generator is also recorded to use it as a reference signal for the subsequent phase-averaging process later on.

4. The images are transferred from the RAM memory of the PIV acquisition unit to a hard drive.

5. The process is repeated again until a total of 240 cycles per view have been captured.

Finally, a discrete gust case is also tested with robotic PIV acquisition. The frequency is increased to 3Hz and the amplitude is set to $\delta_G = 10°$. The acquisition is simpler since in this case the averaging is done by purely synchronizing the discrete measurements over time. On the other side, there exists a problem in terms of the particle concentrations that can be achieved in a reasonable time. While the continuous gust allows the recording of hundreds of cycles in roughly 2 minutes, this case takes around 5 seconds per cycle considering: generation of the gust, interaction with the gust and posterior transient until oscillation dies out and image saving time. This makes the acquisition of many cycles prohibitive both in terms of time and cost due to soap and helium consumption by the HFSB seeding. Therefore, a total of only 10 individual gusts is recorded per PIV view during this study, placing the interest on what kind of spatial resolution can be achieved. This dataset was finally discarded due to a lack of enough particles to properly measure the unsteady flowfield.

The test cases and acquisition settings used for the unsteady aerodynamic cases are summarized in Table 3.5.

Case	**Excitation**				**Acquisition**			
	Flow Speed [m/s]	α_w **[º]**	f_G	δ_G	**Sampling Frequency [Hz]**	**Images per Recording**	**Gust Cycles per Recording**	**Acquisition Time [s]**
Continuous Gust	14	5	2	5	821	32840	80	40
Discrete Gust	14	5	3	10	821	1500	1	4

Table 3.5: Table summarizing the dynamic cases where unsteady aerodynamic measurements where conducted.

4

Methodology

After introducing how the experimental campaign was set up and how the data was achieved, this chapter will cover how the raw data is processed to generate the final results which will be covered in the next chapter. Section 4.1 covers how the raw data (images) acquired with the robotic PIV sytem is processed to generate both flowfield and marker tracking information. Next 4.3 explains how the aeroelastic response of the wing is reconstructed using a simple beam model coupled with an optimization problem. Finally, Section 4.4 explains how some of the aerodynamic and structural loads of the problem can be recovered using some simple, low-fidelity models.

4.1. Processing of robotic PIV data

The main postprocessing steps needed to transform the raw PIV images into flowfield and marker tracking information are presented here.

4.1.1. Image Pre-Processing

Some image pre-processing steps are taken before the tracking of the markers and flow tracers. These steps are mainly directed towards the elimination of reflections coming from the surface of the wing model, and towards improving the tracking performance of the Shake-The-Box algorithm that is used afterwards.

Separation Structure Markers - Flow tracers

In the first place, the images containing both structural markers and flow tracers need to be filtered to separate them. The separation is necessary to ensure an efficient and accurate tracking, since both the markers and HFSB tracers will need their own Optical Transfer Function [1], Volume Self-Calibration [2] and tracking parameters for the application of Shake-The-Box.

The separation of the HFSB tracers can be done through the application of a Butterworth High-Pass filter. This approach was first presented in Sciacchitano and Scarano [64] as a method to remove undesired background reflections based on the decomposition of pixel intensity in the frequency domain. In the case of this thesis, the method can also be used to remove the structural markers from the images since the time scale of their motion is much larger than the average transit time of the bubbles across a single pixel. A kernel of 7 images is selected in *Davis 10* for the application of the filter. This value has been found to give good results in terms of marker removal, while minimizing the introduction of ghost particles which is a known secondary effect of the application of this kind of filter.

The previous approach is able to produce images where only the flow tracers are present, but it is still also necessary to obtain the structure markers. A logical step would be to use the result of the previous operation:

[1] Hereafter referred to as OTF
[2] Hereafter referred to as VSC

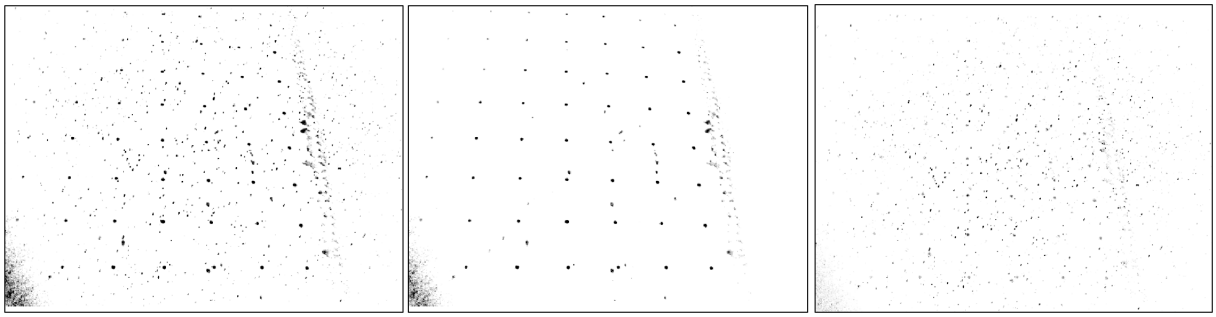

Figure 4.1: Result of the process used to separate structure markers and flow tracers. Left: raw image. Center: Marker grid. Right: Flow tracers. The image is displayed with an inverted gray scale.

subtract the recordings of the HFSB tracers from the original images to obtain images where only markers are present. Unfortunately this is not completely possible in *Davis 10*, and the subtraction operation fails to completely eliminate the HFSB tracers. An alternative approach is needed, and the processing software has other interesting filtering functions, of which the application of a symmetrical minimum time filter with a kernel size of 3 images has been found to produce the desired output. An example of the application of this methodology to the images acquired during the campaign is shown in Figure 4.1.

Structure Markers

After separating the markers from the original recordings, some further operations are performed on the images before the tracking step. The operations are listed in Table 4.1.

Operation	Parameter Value
Subtract Sliding Minimum	50 px
Gaussian Smoothing	3x3 px
Multiply Pixel Intensity by Factor	1.1

Table 4.1: Pre-processing steps used for the structural markers.

A sliding minimum is applied to remove any remaining reflections and a gaussian smoothing is applied to the markers to uniformize their appearance, which has been found to be beneficial for tracking. Finally, the intensity of the pixels is multiplied by a small factor to compensate for the effect of the sliding minimum subtraction.

Flow Tracers

No further pre-processing steps are applied to the recordings containing the flow tracers before the application of the Shake-The-Box algorithm.

4.1.2. Tracking with Shake-The-Box

The main processing step is the application of the Shake-The-Box algorithm to the images to obtain the tracks of both the markers and the flow tracers.

This step requires the previous creation of an Optical Transfer Function as well as a Volume Self-Calibration. The purpose of these will not be covered in this section (the reader is directed to Schanz et al. [61] and Schanz et al. [62] for detailed explanations), but it is important to highlight some aspects about how they are generated. Specifically, the creation of the OTF and VSC requires images from the tracers that are to be tracked. This means that in this study, two sets of OTF/VSC are created: one for the HFSB flow tracers and another one for the structural markers.

It is also important to remark that, as specified by the *Davis 10* documentation, the images used for this purpose are not the original ones but those on which the pre-processing steps described in the previous section have already been applied. Furthermore, images from different views (robot positions) are used for the generation of the OTF and VSC, as this is known to be beneficial for the final quality of the calibration process.

Finally, during the tracking with the time-resolved Shake-The-Box algorithm, the value of some parameters must be chosen. Their purpose is to tune how the algorithm detects and tracks particles, and some small differences exist between the values used for the tracking of markers and those used for the tracking of helium bubbles. The parameters and their values are listed on Table 4.2. The values used for the tracking of bubbles are mainly the default ones, while the ones used for markers have been chosen based on experience and give a good compromise between the amount of markers that are tracked simultaneously and the quality of their positional information in terms of the level of noise.

	Operations	**Units**	**Marker Tracking**	**HFSB Tracking**
Particle Detection	Threshold for 2D particle detection	[counts]	10	2
	Allowed triangulation error	[px]	1.5	2
Shaking	Outer loop iterations	[-]	8	4
	Inner loop iterations	[-]	8	4
	Shake particle position by	[vox]	0.1	0.1
	Remove particles if closer than	[vox]	30	1
	Remove particles if intensity lower than	[vox]	0.10	0.10
Particle shape and Intensity	OTF size factor	[-]	1.3	1
	OTF intensity factor	[-]	1	1
	OTF radius factor	[-]	auto	auto
Tracking	Minimum track length	[timesteps]	4	4
	Velocity limits [X,Y,Z]	[m/s]	[5, 5, 3]	[25, 10, 10]
	Max. absolute change particle shift	[vox]	5	2
	Max. relative change particle shift	[%]	35	25

Table 4.2: Shake-The-Box parameters used for the tracking of structural markers and flow tracers.

On the Shake-The-Box velocity limits

As mentioned previously, the time-resolved data is used to obtain the Lagrangian information from the flow using Shake-The-Box, meaning that no Double Pulse-Double Frame or Multi-Step techniques are used. One known limitation of using time-resolved information affects the maximum flow speeds that can be recovered with the tracking algorithm. This limitation comes from the maximum displacement that the flow tracers can undergo between two consecutive frames: if the flow speed is too high this displacement will increase and the algorithm might fail in pairing the same particle between frames. Previous research on this aspect by authors like Jux et al. [35] or Saredi et al. [56] indicates that time-resolved data can be successfully processed with Shake-The-Box for flow speeds under the limit $U_\infty \lesssim 15$ m/s.

The measurements conducted in this study are taken at an incoming flow speed of $U_\infty = 14$ m/s although the presence of the wing will accelerate the flow locally, likely surpassing the aforementioned tracking limit. This does not mean that the tracking algorithm will fail completely, but a slight decrease in the number of

tracks being tracked by the algorithm and an increase in false pairing can be expected. This is a known limitation of the study, and the flow speed was not changed to maximize the structural response of the wing to the gusts, which was a preferential aspect for this campaign.

4.1.3. Phase-Averaging of Unsteady Flow data

As introduced in Section 3.6.2, the PIV measurements in unsteady conditions are to be phase-averaged to increase the spatial resolution and the statistical convergence of the final flowfields. This is something that can be easily done in periodic events, where the acquisition of several cycles (in the order of hundreds) can be done in a matter of minutes. This section introduces how the phase-averaging of the data was conducted in this study for the case of a continuous gust excitation.

To synchronize in time and phase-average the data, a reference signal must be recorded in parallel with the image acquisition of the robotic PIV system together with the trigger signal. In this case, the trigger signal is provided by the gust generator control system, which also stores the gust generator vane angle over time as the reference signal. Once this is done, the objective is to divide the periodic reference signal into cycles and to define phases within those cycles. Each phase within a cycle will define one instant in the interaction between the wing and the gust. A sketch of the phase-averaging approach is shown in Figure 4.2.

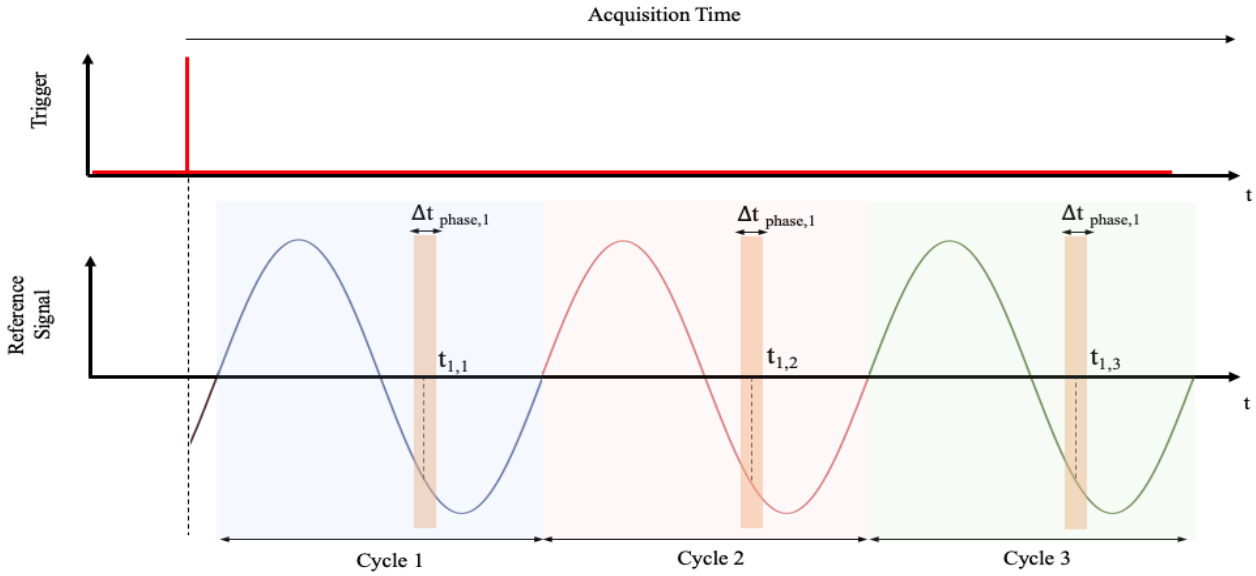

Figure 4.2: Sketch of the phase-averaging methodology

In the first place, the trigger is identified to determine the start time of the acquisition and secondly, the reference signal is divided into cycles, where the start and end of each cycle are defined by the zero-crossings of the signal. The next step is to define the phases within each cycle, as well as a time kernel k_T with which those phases will be defined. The value of k_T is defined as a percentage of the duration of each cycle T_{cycle} and it therefore defines the number of phases in which each cycle is divided. For example, for a time kernel of 1% of T_{cycle}, 100 phases can be defined.

The final outcome of the process are the time instants $t_{i,j}$ where i corresponds to the phase and j corresponds to the cycle, which define the **instantaneous** phases. However, because of the use of a time kernel, these time instants become "time bins" defined by:

$$\Delta t_{phase} = t_{i,j} \pm \frac{k_T * T_{cycle}}{2} \tag{4.1}$$

For each cycle, a "time bin" corresponding to each phase will exist. From an practical point of view, this means that from our measurements, all the particles captured within the Δt_{phase} bins will be gathered and used as an input for the ensemble averaging of the flow data. The value of the time kernel therefore allows to establish a trade-off between the statistical convergence of the flowfield and temporal resolution: the higher the value of the kernel, the bigger Δt_{phase} will be and consequently there will be a higher number of particles, increasing the statistical convergence.

Increasing the value of k_T is in principle something undesirable as it implies a loss in temporal resolution. However, if there is a large enough difference between the characteristic timescales of the flow and the structure, it can be argued that the value could be increased up to a certain limit. As long as the transit time of the flow tracers over the chord is much smaller than the period of oscillation of the wing, the structure is effectively "frozen" from the point of view of the flowfield, meaning that several time instants can be averaged together without necessarily losing a significant amount of temporal resolution. This is a condition that applies to this specific case, but might not be fulfilled in other experiments where the timescale of the structural motion is smaller.

4.1.4. Ensemble Averaging

The flowfield information produced by the STB algorithm is in Lagrangian format, meaning that the discrete position of the particles and their velocities is known over time. This data format is unstructured and makes the handling (combining different measurement views, computing gradients...) and interpretation of the information more complex. It is therefore preferred to transform this data into a structured Eulerian grid, using a process formally known as ensemble averaging.

This process takes all the particles captured in a measurement run and divides the volume that contains them into cubic cells, also commonly referred to as bins. Each of those cells will contain a variable number of particles with their corresponding velocities, from which velocity statistics for that cell can be computed. One of the most important aspects of this process is the definition of the cell size l_b, which determines the spatial resolution of the resulting velocity field since it defines the smallest resolvable length scale. Ideally this value should be small, although reducing the value of l_b implies a reduction in the number of particles inside each bin and an increase in the uncertainty level of the velocity as described by

$$\epsilon_u = \frac{z_a \sigma_u}{\sqrt{N_{unc}}} \tag{4.2}$$

where N_{unc} indicates the number of uncorrelated measurement samples within the cell, σ_u is the standard deviation of the velocity (which can be estimated from the PIV measurements themselves) and z_a is a coverage factor to account for the confidence interval.

Increasing the spatial resolution is also particularly important in this experiment in order to have a final flowfield which complies with the geometry of the wing. If the bin size is too big (of the order of the thickness of the airfoil), the flowfield and the reconstructed wing surface will inevitably overlap. For reference, Figure 4.3 shows bins of different sizes compared to the leading edge of the airfoil.

Another choice that must be made is how to recover the velocity statistics for the bin from the velocity information of the particles inside it. The work of Agüera et al. [2] explores methods of different complexities and computational costs, ranging from a top-hat filter to a polynomial fit inside the bin, which is shown to give the best results. In this study, the top-hat filter has been used for the ensemble averaging of all cases. This choice is made based on the fact that the cases measured here are never truly static:

- During the static measurements, the wing suffers small oscillations.

- During the continuous gust measurements, even if a good level of repeatability is expected,the wing could be in slightly different positions for the same phase in different cycles of the measurement. Considering that the position of the CVV probe stays fixed during the measurement, any non-periodical effects will introduce a small positioning error of the particles in the global reference system.

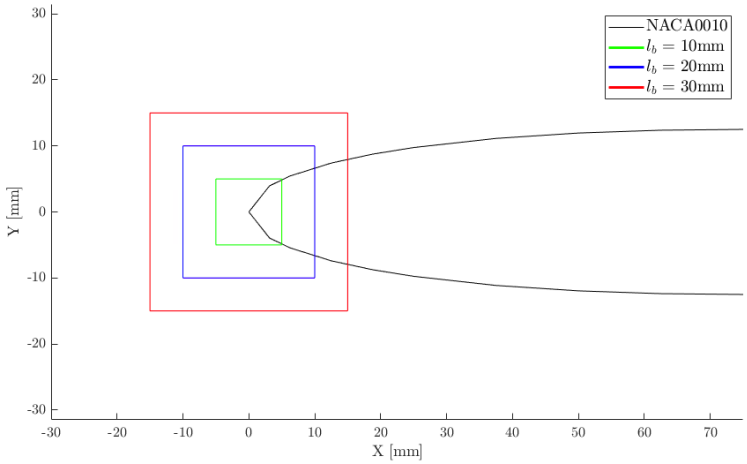

Figure 4.3: Comparison between the leading edge of the NACA 0010 used in the wing and bins of typical sizes used for ensemble averaging of Lagrangian PTV data.

Because of this, the use of more advanced averaging approaches which account for spatial variations of velocity within the cell does not make sense if the cell is not perfectly static, or at least if it is not guaranteed that the order of magnitude of the positioning error introduced by the wing vibrations / non-periodical effects is much smaller than the bin size used for the ensemble averaging.

Apart from the use of the top-hat filter, a bin size of 10mm and an overlap between bins of 75 % has been chosen. These settings give good results for the static case and also in the phase-averaged cases where particle concentration could be a limiting factor. A discussion of the quality of the flowfields in terms of the relative uncertainty of the velocity measurements will be offered in Chapter 5.

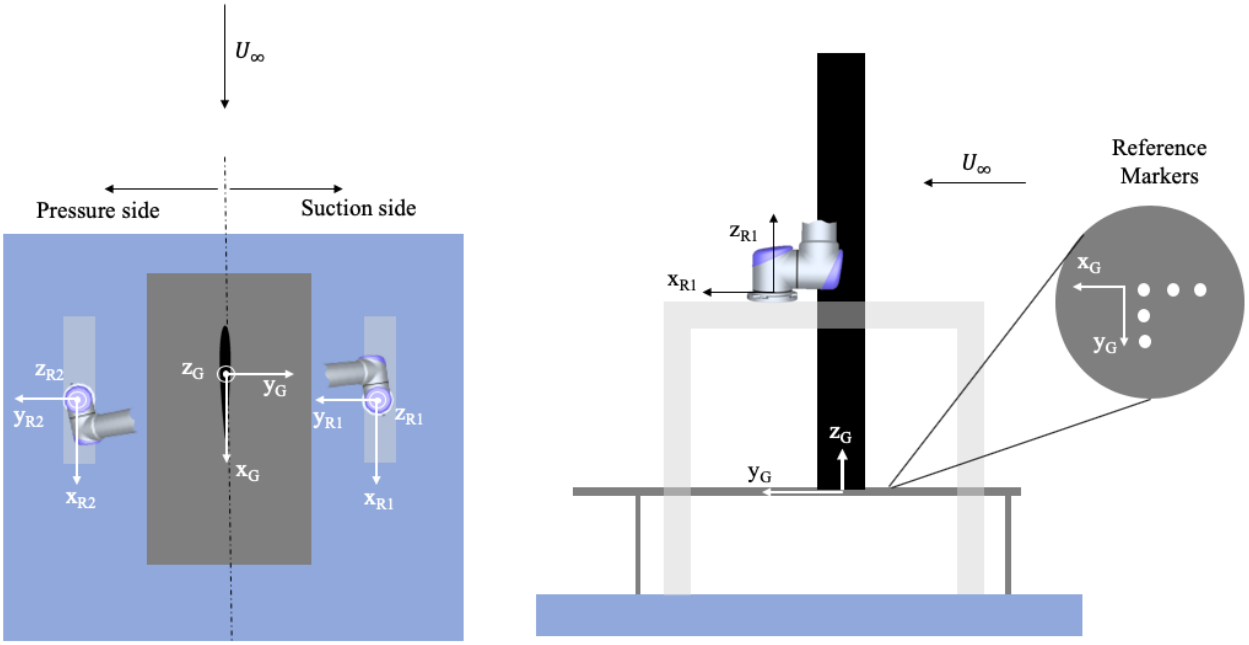

Figure 4.4: Top and lateral view of the reference systems used for local and global data positioning. Close up: reference markers used for global positioning of the data.

4.1.5. Data Positioning

As described in Section 3.3.3, the robot control software can be used in coordination with the *Davis 10* acquisition software to transform the data of each measurement from the "Tool" reference frame (see Fig.3.4) to the "Robot Base" reference frame, positioning the measurements into a common reference frame as long as the robot base stays in the same location within the wind tunnel setup during the campaign. However, in large-scale experiments it is commonly more useful to position the measurements in a global reference frame which is more consistent with the wind tunnel setup. In addition, in this study the location of the robot changes from one side of the wing to the other to capture the entire flowfield around it. This makes mandatory the definition of a global reference frame in which measurements from both sides can be merged and interpreted.

Figure 4.4 shows the local reference systems (x_{G1}, y_{G1}, z_{G1}) and (x_{G2}, y_{G2}, z_{G2}), defined by the locations of the robot as well as the global reference system which is located at the base of the wing and centered at its mid-chord point at $\alpha_w = 0°$. The global reference system does not rotate with the angle of attack of wing. With the chosen setup, the transformation from one frame to the other only requires the application of a translation in X,Y and Z. This translation is determined with the help of some reference markers (see close-up in Fig. 4.4) painted on the support table on which the wing rests, as well as with the information of marker position measured with the robotic PIV system.

4.2. Performance of Marker Tracking with Shake-The-Box

4.2.1. Pre-processing of marker tracking data

The first step in the wing reconstruction process is to filter and organise the marker information outputted by STB. This is necessary for a series of reasons:

- **Filter marker outliers.** The raw images of the marker grid might contain small reflections caused by laser illumination or by the presence of soap accumulations on the wing, especially at the location of the zig-zag strip. These features are sometimes identified as markers by the STB algorithm and therefore result in false marker tracks in the final data. These false tracks are filtered based on their total track length, which is usually much shorter than a real marker. Further filtering can be done based on whether the positions of those tracks are consistent with the dimensions of the marker grid: real markers should stay within at least 30mm from other markers in all directions.

- **Marker track interruption.** The marker tracks created by STB are sometimes interrupted. This can be caused by markers going out of the field of view of the cameras, markers losing light intensity as they move away from the CVV probe and factors which originate from the STB software. Some mitigation of the problem can be achieved with some image pre-processing operations and a careful selection of the tracking parameters used by STB. However, the end result is that, for a set of images containing N markers, the final STB data file might contain up to hundreds of tracks which in reality, when put together, correspond to the real N tracks that should exist. An algorithm therefore needs to be established to reorganize this information, as explained in the next paragraph.

Track-Stitching algorithm

The algorithm created to compute the complete marker tracks works in the following way:

1. When an interruption of a marker track is detected at time t_n, a sphere of radius R is created in 3D space, with its center placed at the last known coordinates of the markers.

2. The output file produced by the Shake-The-Box software is scanned to look for a valid continuation of the track, which must satisfy the following two requirements:

   - The continuation of the track must be located within the search sphere.
   - The track must continue in the future, that is, at a time $t_{n+\Delta t} > t_n$.

In this study, a value of R = 20 mm has been found to give good results. However, this parameter would likely need to be adjusted in other cases depending on factors such as the expected speed of the markers and the typical duration of the interruptions in the marker tracking.

4.2.2. Marker tracking performance with STB

Once the complete marker tracks are built, it is possible to get some information about marker tracking performance with the Shake-The-Box algorithm. As an example of the quality of the tracks, Figure 4.5 displays two cases: a marker from an acquisition conducted in "wind-off" conditions and a marker from a measurement run where the excitation was a discrete gust at 24 m/s.

In the first case, the wing was perfectly still and therefore, no oscillations in the position of the markers should be expected. As the aforementioned figure shows, the positional oscillations measured by STB are of the order of tenths of millimeters. The magnitude of these oscillations can be used to estimate the tracking precision of STB when applied to marker tracking. Some detailed values are displayed in Table 4.3, where the standard deviation in each dimension has been computed for 2 static cases: wind-off and wind-on. In both cases, the final value corresponds to the average and maximum standard deviations computed among the entire marker grid.

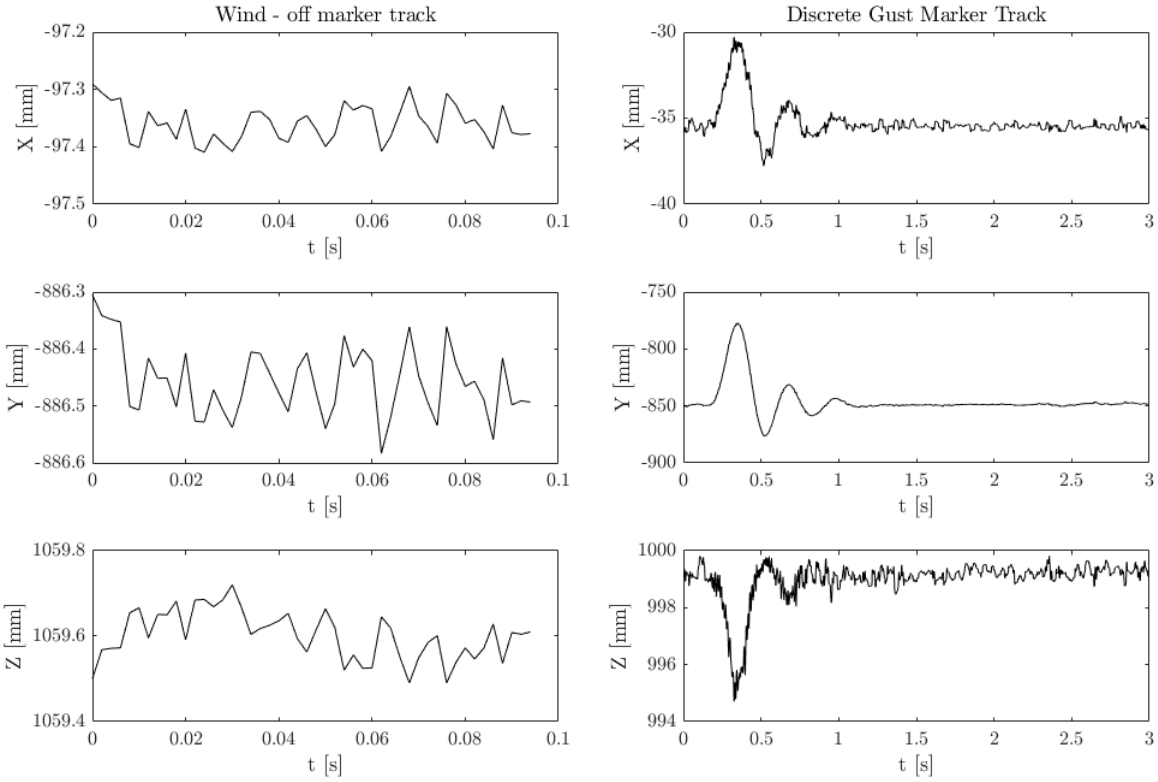

Figure 4.5: Examples of marker tracks for a static case with no wind and a discrete gust at 24 m/s.

	N° of samples	**N° of**	σ_X **[mm]**		σ_Y **[mm]**		σ_Z **[mm]**	
	in Time / Marker	**Markers**	Avg.	Max.	Avg.	Max.	Avg.	Max.
Static, Wind - Off	50	413	0.07	0.38	0.25	1.0	0.22	0.91
Static, Wind - On	500	383	0.15	0.47	0.50	1.06	0.42	1.02

Table 4.3: Standard deviation of marker position in wind-off and wind-on static cases. Both cases acquired at 500Hz.

The value of the standard deviation in the wind-off case originates from the measurement system itself, since there are no external factors that could be causing an oscillation of the wing. In particular, the STB software could be introducing some uncertainty due to the way it detects the markers in the images and positions them in space. On the other hand, the low-aperture angle of the CVV probe could also play a role, which could explain why the value of the standard deviation in the Y and Z directions is higher than that of the X direction. Because of the robot positioning, the CVV main axis is contained in a YZ plane[3].

Furthermore, the standard deviation computed in the wind-on case originates from the aforementioned factors as well as from any vibrations of the wing caused by non-uniform flow conditions. The difference with respect to the wind-off case seems to indicate that vibrations of the wing could be estimated as a few tenths of a millimeter. However, this value was computed using marker information from acquisitions with an observation time of only 1 second, so bigger oscillations outside of this observation period cannot be completely ruled out.

These noise levels seem to be similar in dynamic cases as the one displayed in Figure 4.5. An aspect to highlight is the excellent continuity of the track in this case, which is representative for all the other measurement cases. This good continuity means that in general, interruptions of the tracks are short as long as the marker stays within the field of view of the camera, and thus it has deemed unnecessary to use any kind of interpolation to fill in the missing information during those interruptions. It is also assumed that, even if a marker is lost for more than a few time-steps, there will be sufficient remaining markers to still be able to retrieve structural information.

4.2.3. Absolute marker positioning in 3D space

The information discussed in the previous section seems to indicate that the tracking performance of the STB applied to markers is very good, with noise levels of under a millimeter. However, there is an additional relevant aspect that must be discussed regarding the measurement of markers with robotic PIV: the absolute positioning in 3D space.

As mentioned in Chapter 3, the measurement of the entire wing requires conducting a span-wise sweep with the robot, meaning that several views will ultimately need to be merged together into the global reference system. It is important that the relative positioning between the different views is consistent, meaning that for example, a sweep of the entire wing in wind-off conditions should result in a set of markers that define a smooth surface and that are positioned with respect to each other according to the dimensions of the grid that was imprinted on the wing.

However, when doing this a significant positioning error is found, as shown in Figure 4.6. The markers not only do not define a smooth surface, but they show a significant misalignment of the order of centimeters between views, mainly in the Y direction. In addition, within each individual view, a curvature of the surface defined by the markers can be observed . This effect is also incompatible with the geometry of the wing and it cannot be attributed to the positional information of the robot, but rather to an optical distortion not corrected by the calibration process. The hypothesis as to where this issue originates is that it is caused by the robot and CVV probe for one/a combination of the following reasons:

- The robot positional accuracy and repeatability could be worse than the one advertised by the manufacturer. This could be caused by a maintenance issue, meaning that the robot should be re-calibrated.
- When conducting a full scan of the wing, the robot undergoes large displacements in between measurement positions, meaning that the views are quite far apart from each other. Any small errors in the positional information reported by the robot controller could be amplified by this fact and cause the observed problem. It is worth highlighting that an observation which favours this explanation is that when conducting the PIV measurements the views were much closer together[4] and in this case the markers were indeed aligned as expected.
- Since these measurements only involved capturing markers and not flow tracers, a larger field of view of the cameras was selected to capture larger sections of the wing per acquisition. This is another possible

[3] As per the global reference system introduced in Fig.4.4

[4] The robot did not change height, just slightly rotated around the wing to capture the flowfield along the chord

origin of the issue, since the positioning error was not observed during the PIV acquisitions were the field of view was reduced. Specific OTFs and VSCs were created for the acquisition with an extended FOV using images of markers as an input, and it is possible that these images did not contain enough markers to generate a successful volumetric calibration.

- Shortly before finishing this research project, an inspection of the robot before re-calibration revealed that one of the robot joints had a broken component. This fact was unknown for most of the duration of this research and it is obviously a clear candidate for the origin of the positioning problem.

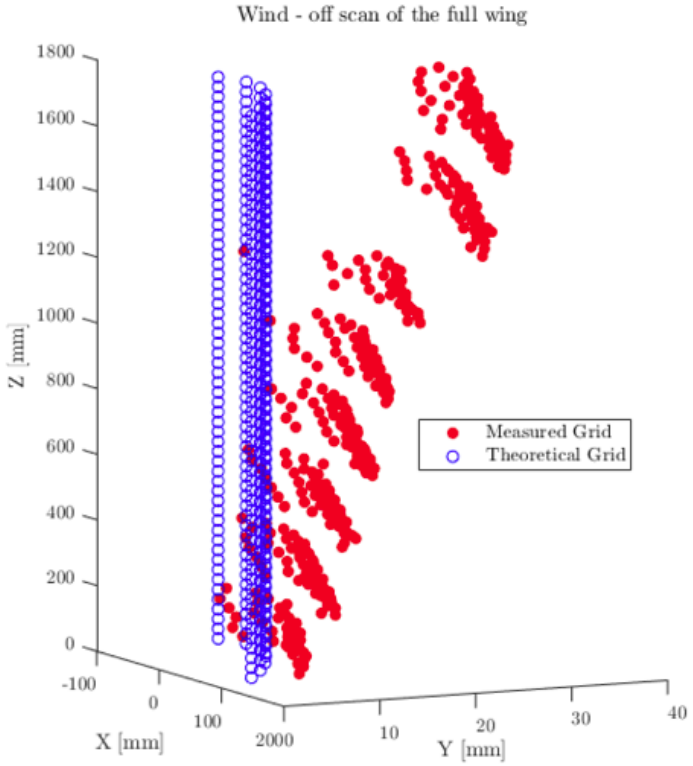

Figure 4.6: Positioning error found when merging all different views of the wing into the same reference system

The marker information is unusable in this state, which indicates that a methodology must be developed to circumvent this issue. This is explained in the next subsection.

Marker position correction

Fortunately, the aforementioned problem could be bypassed thanks to a series of reasons listed here:

1. The positional error of each view was observed to stay unchanged in between measurements. It affects all of them, but the effect on each view is always the same.
2. The exact same robot positions were used throughout the campaign whenever a full scan of the wing was conducted.
3. Scans of the wing for each angle of attack were conducted in both wind-off and wind-on conditions.

These facts open the possibility of effectively removing the error in position for each view by computing the relative displacement between a given wind-on condition (static or dynamic) and its correspondent wind-off measurement. As a result of this approach, the markers are not used to give absolute positional information but a relative displacement field between conditions. This field can then be applied to a theoretical

grid where the markers are positioned according to the dimensions of the wing and of the marker grid that was imprinted on it. Once the shape of the deflected marker grid is established, that information can be used to recover the 3D wing shape following the method to be explained in Section 4.3.

The basic steps of this algorithm are shown in Figure 4.7. As it can be seen in the middle section of the image, the deflected marker grid obtained using relative displacement information from the markers is more in line with the expectations: while some small misalignment can still be appreciated, the grid now clearly defines a surface.

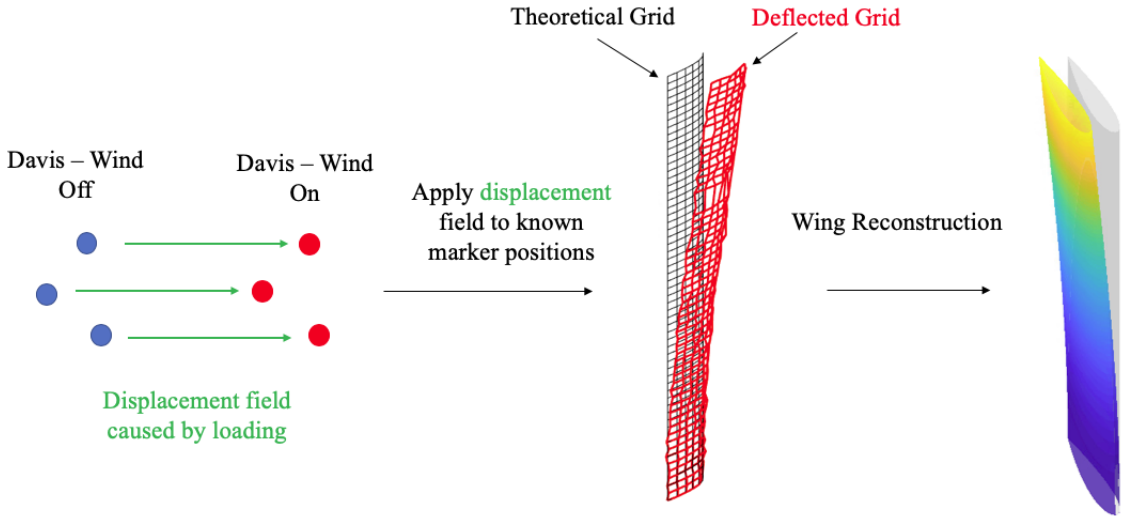

Figure 4.7: Basic steps of the process used to bypass the error in positioning of the markers from different views.The surface of the wing is colored by the lateral deflection of each section. A detailed analysis of the deflection will be provided in the next chapter.

4.3. Reconstruction of Wing Response using Marker information

So far, it has been discussed how the raw information (images) is processed to produce steady and unsteady flowfield information in Lagrangian format and its posterior translation to a structured grid. The processing of marker information with the Shake-The-Box algorithm has also been covered, highlighting some of the small differences that exist between marker tracking and HFSB tracking. While this information is useful, the full reconstruction of an aeroelastic event requires further steps to recover more meaningful information such as loads or the magnitude of the wing deflection for example.

Once positioned in the final reference frame, the aerodynamic information which results from the ensemble averaging process can already be used to derive some important variables such as the pressure fields and thus the aerodynamic loading on the wing. On the other side, the raw marker information is just a set of individual marker tracks which offer limited insight into the problem just by themselves.

Therefore, the next step in the processing of the data is to develop a methodology to recover structural information from the marker tracking data. In this study, the chosen approach has been to develop a wing reconstruction algorithm which couples a simplified structural wing model with the marker information. The wing is modelled as a 1D beam from which the 3D geometry is recovered. Subsequently, an optimization problem is formulated to find the load that must be applied to that beam to deflect it in such a way that the final 3D wing shape matches the deflected marker grid as measured by the robotic PIV system.

In this section, the steps of the wing reconstruction algorithm will be explained in detail.

4.3.1. Wing Beam model

The wing reconstruction is conducted based on a simplified model where the entire wing structure is reduced to an Euler-Bernoulli beam. The beam is only allowed a single degree of freedom which is the deflection in the direction perpendicular to the wing chord or bending.

The bending stiffness is allowed to change along the span of the wing as described in Figure 4.8. The plot shows the variation of the bending stiffness ratio EI_i/EI_1[5] along the different design regions of the wing, where E is the elastic modulus of the material of the beam and I is the second moment of inertia of the beam cross-section. The real wing was designed with three design regions of equal length (58.3 cm), and the values of the stiffness ratio have been extracted from a finite element model of the structure created in the in-house structural analysis software PROTEUS. The simplified wing model only accounts for the change in stiffness between regions 1 and 2, as it is the one with the biggest magnitude and because that formulation simplifies the solution of the beam deflection equation. The exact value used for the stiffness jump is $EI_2/EI_1 = 0.28$, which is the average between the ratios EI_2/EI_1 and EI_3/EI_1 in the wing FEM model.

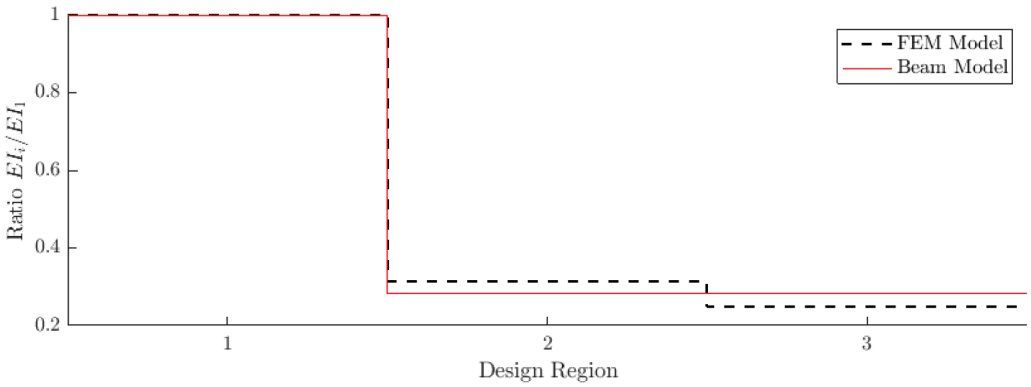

Figure 4.8: Change in the stiffness ratio EI_i/EI_1 along the different design regions of the wing.

The final element needed in the model is the loading on the wing. In this case, the loading on the wing has been modelled as a uniform load per unit length q_{ufm}, which accounts for both the aerodynamic q_{aero} and inertial loading q_{inr}. The value of this uniform loading will be constant in cases of static aerodynamic loading or change over time in dynamic cases of continuous and discrete gusts.

Modelling the load as a uniform distribution is a significant simplification since the real span-wise load experienced by the wing might be far from this assumption. However, the primary goal of this modelling approach is to explore how marker information can be used to retrieve meaningful structural information. In that sense, while a uniform load might not accurately represent the reality of the problem, it is believed that it could be a good approximation in terms of order of magnitude. In addition, choosing a uniform load distribution allows an analytical solution of the beam equation, which simplifies the wing reconstruction problem.

As a final remark regarding the constant load assumption, the reader is directed to Figure 4.9 where sketches of the typical load distribution from aerodynamic and inertial origin are shown. The aerodynamic load is basically equivalent to the lift, which in potential theory can be modelled as a constant load and a posterior drop caused by wing-tip losses until the lift becomes null at the tip. On the other side, the inertial loading on a clamped wing under gust conditions will be almost zero at the root of the wing and it will grow towards the tip since that is the area that experiences the largest deflections. Considering these distributions, the uniform load assumption can be considered as a reasonable approximation for the aerodynamic load, and the largest discrepancies are to be expected to occur at the wing tip. In this area, not only is the aerodynamic load not uniform, but also where the inertial load experiences its largest variations. Finally, as it will be shown later in this document, the inertial loading is significantly smaller in magnitude than the aerodynamic loading.

[5] The sub-index denotes the design region.

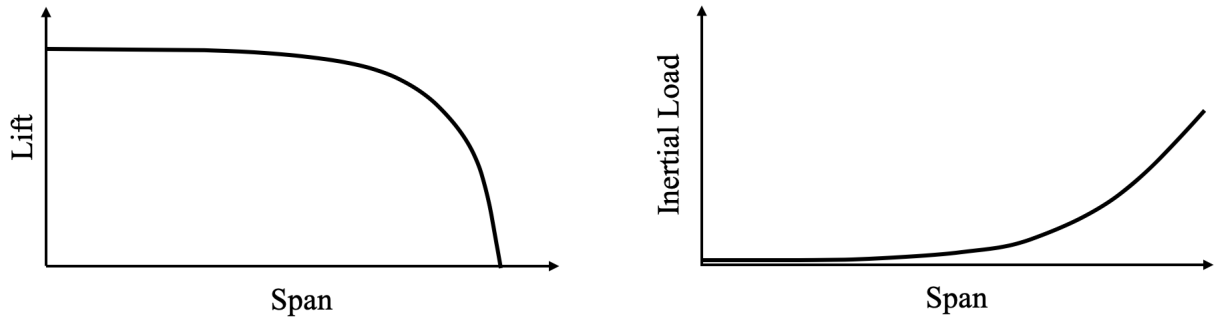

Figure 4.9: Sketches of the expected distributions of the aerodynamic and inertial loading acting on the wing.

Once the stiffness properties and load are known, the deflection of the beam w can be computed from the Euler-Bernoulli beam equation:

$$\frac{\mathrm{d}^2}{\mathrm{d}z^2}\left(EI\frac{\mathrm{d}^2 w(z)}{\mathrm{d}z^2}\right) = q_{ufm}(t) \approx (q_{aero}(t) + q_{inr}(t)) \tag{4.3}$$

which can be solved analytically under the previously discussed conditions, giving as a result two fourth-order polynomials $w(z_1)$ and $w(z_2)$, where z_1 and z_2 correspond to the two span-wise wing sections with different stiffness. The integration of Equation 4.3 leads to two expressions for the deflection of each region of the beam model:

$$EI_1\, w(z_1) = \frac{q_{ufm}}{24} z_1^4 + \frac{1}{6} C_1 z_1^3 + \frac{1}{2} C_2 z_1^2 + C_3 z_1 + C_4 \qquad 0 < z_1 < L_1 \tag{4.4}$$

$$EI_2\, w(z_2) = \frac{q_{ufm}}{24} z_2^4 + \frac{1}{6} C_5 z_2^3 + \frac{1}{2} C_6 z_2^2 + C_7 z_2 + C_8 \qquad 0 < z_2 < L_2 \tag{4.5}$$

where L_1 and L_2 are the lengths of the first and second sections of the beam model respectively. $C_1 - C_8$ are the integration constants which must be determined through the application of the proper boundary conditions. The boundary conditions affect the deflection of the wing w, its first derivative w', the shear force Q and the moment load M:

- **Wing Root:** The wing is modelled as being clamped at the root, which means that both the deflection and rotation of the wing sections at this location is zero. These boundary conditions determine the value of integration constants C_3 and C_4.
  - $w(z_1 = 0) = 0$
  - $\frac{\mathrm{d}w}{\mathrm{d}z}(z_1 = 0) = 0$
- **Wing Tip:** At the tip of the wing, both the shear force and the moment will tend towards zero. With this information, the value of C_5 and C_6 is found.
  - $M(z_2 = L_2) = EI_2 \frac{\mathrm{d}^2 w}{\mathrm{d}z^2}(z_2 = L_2) = 0$
  - $Q(z_2 = L_2) = EI_2 \frac{\mathrm{d}^3 w}{\mathrm{d}z^3}(z_2 = L_2) = 0$
- **Collocation point where the two sections connect:** At this point, first an equilibrium of loads between the two sections is prescribed, allowing the determination of the C_1 and C_2 integration constants.
  - $M(z_1 = L_1) = M(z_2 = 0)$
  - $Q(z_1 = L_1) = Q(z_2 = 0)$

Finally, the continuity of the deflection of the wing is also imposed at this location.

- $w(z_1 = L_1) = w_2(z_2 = 0)$
- $\frac{\mathrm{d}w}{\mathrm{d}z}(z_1 = L_1) = \frac{\mathrm{d}w}{\mathrm{d}z}(z_2 = 0)$

Due to the prescribed continuity of loads (Q, M) at the collocation point and considering that $EI_1 \neq EI_2$, a discontinuity must appear in the second derivative of the beam deflection. This discontinuity is related to the jump in the strain distribution that will be shown in Section 5.1.1.

Once the deflection of the beam has been determined by means of the two polynomials, the information can be used to reconstruct the 3D wing geometry. A reference axis is positioned at the mid-chord of the wing and the deflection is applied to it creating a line in 3D space. Afterwards, wing sections (NACA0010) are positioned along that line ensuring that their mid-chord coincides with the reference axis and that they stay perpendicular to the direction defined by the axis. This last point basically means that as the wing deflects, the sections experience a rotation as a result of the bending. The reconstruction process is illustrated in Figure 4.10.

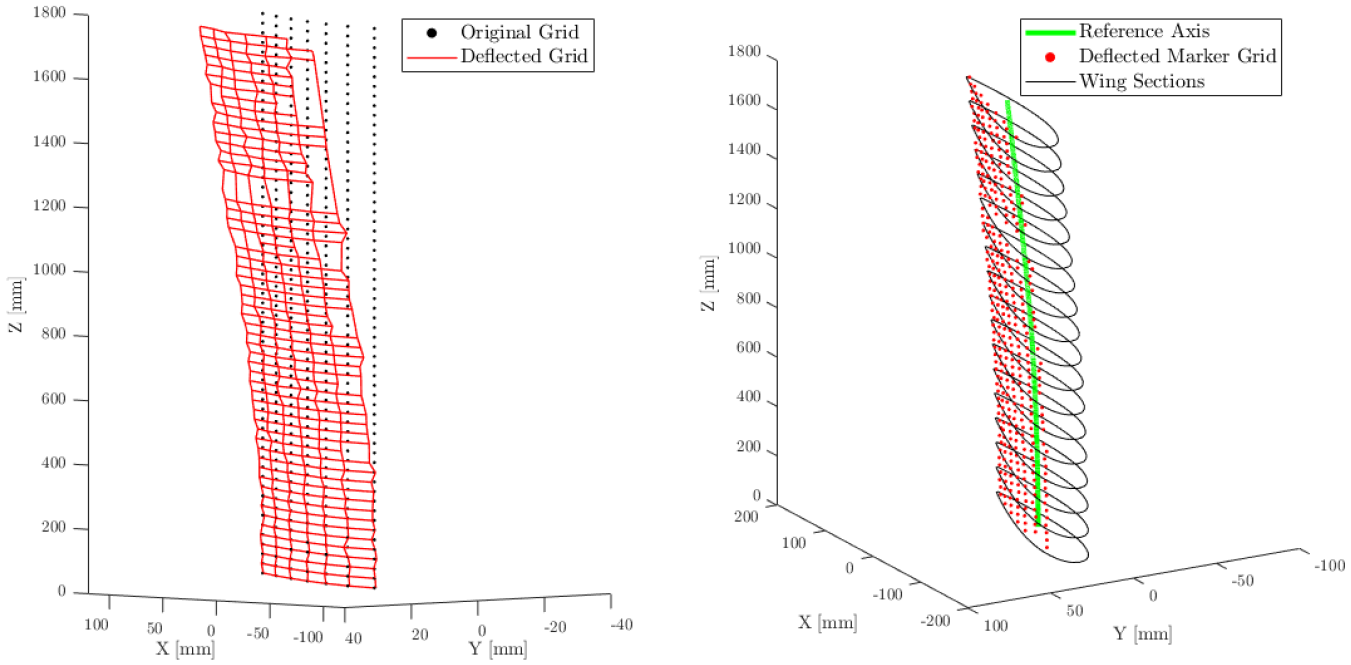

Figure 4.10: Left: Deflected marker grid at U = 14 m/s and α_w = 5°. Right: Positioning of wing sections along the reference axis that matches the deflected grid.

4.3.2. Wing reconstruction: Optimization problem

The reconstruction process described previously can only be started if the corresponding load q_{ufm} is known. This value is not available from marker or PIV measurements, and therefore an optimization problem is defined to find it. The problem involves finding the value of q_{ufm} that, in combination with the structural properties of the wing, produces a 3D wing shape that minimizes the distance $\overline{x}_{err}$ between the deflected marker grid and the surface of the reconstructed wing. This is done a single time in the case of the measurement of the static deflection of the wing, but must be ran for every timestep in time-dependent cases.

In particular, the objective function defined for this problem minimizes the average distance $\overline{x}$ between the measured position of the markers in 3D space and the position they would have in the reconstructed wing geometry:

$$\overline{x}_{err} = \frac{\sum|(\vec{x}_{measured} - \vec{x}_{reconstructed}|}{N_{mks}} \tag{4.6}$$

Where N_{mks} is the number of markers being tracked at a certain time instant. The mean fit error was chosen as the variable to be minimized during the early stages of the project. The mean is known to be more sensitive to outliers in the data, but it was kept throughout the entire study after observing that the use of other more robust measures such as the Root Mean Square did not produce any difference on the results. Finally, the Sequential Quadratic Programming method available in MATLAB is chosen as the optimization algorithm.

Apart from an optimal value of q_{ufm}, the final value of the objective function also gives a good estimation of how well the reconstructed 3D wing geometry matches the measured position of the deflected marker grid. In general the procedure has been found to give good results, with final objective function values in the order of 1mm. Further insight into the quality of the reconstruction and the origin of this value will be provided in Section 5.1, where the distribution of the reconstruction error over the wing will be discussed.

4.3.3. Structural properties of the beam model

The stiffness ratio EI_2/EI_1 between the two sections considered in the simplified wing model can be estimated from the FEM model mentioned previously. However, the value of EI_1 still needs to be determined to reduce the optimization problem to just finding the value of q_{ufm}.

The value of EI_1 is tuned based on the measurements of the static deflection of the wing at 14m/s and 24m/s, for which force balance measurements are also available. The process is comprised of the following steps:

- The force balance measurements are used to compute the equivalent uniform static loading q_{ufm} for each of the cases, where $q_{ufm,balance} = \frac{F_y}{b}$, being F_y the balance measurement and b the span of the wing.

- The value of $q_{ufm,balance}$ is used as an input to the optimization problem. In this special case, the load and the stiffness ratio EI_2/EI_1 are known and the optimization outputs the value of EI_1 which best reconstructs the shape of the deflected grid.

- The previous step produces two values for EI_1. The final value is chosen as the average of those two, that is:

$$EI_1 = \frac{EI_{1,14m/s} + EI_{1,24m/s}}{2} \tag{4.7}$$

The final structural properties used in the simplified wing beam model are listed in Table 4.4. An analysis of the order of magnitude of the expected wing tip deflection w_{tip} can be conducted based on equations 4.4 and 4.5, to check the sanity of the values reported in the table. This shows that:

$$\mathcal{O}(w_{tip}) \sim \mathcal{O}\left(\frac{q_{ufm}b^4}{EI}\right) \sim \mathcal{O}\left(\frac{10\,\text{N/m}\cdot(1.75\,\text{m})^4}{8.5\cdot10^2\,\text{Nm}^2}\right) \sim \mathcal{O}(0.1\,\text{m}), \tag{4.8}$$

where the order of magnitude of q_{ufm} has been chosen based on the force balance measurements presented in Chapter 5. Deflections of the wing tip of the order of 10 cm are expected based on the design specifications of the wing, on the behaviour observed during the tests and on the displacement of the markers. Thus, it is concluded that while the final value used for EI_1 might differ from the real one, its order of magnitude is consistent with the forces and deflections that characterize the wing response.

Final Structural Properties		
Parameter	**Units**	**Value**
$EI_{1,14m/s}$	[Nm^2]	8.047·10^2
$EI_{1,24m/s}$	[Nm^2]	8.997·10^2
EI_1	[Nm^2]	8.522·10^2
$\frac{EI_2}{EI_1}$	[-]	0.28

Table 4.4: Final structural properties used in the beam model.

4.4. Load Reconstruction using low-fidelity models

The use of a simplified structural model for the reconstruction of the wing opens up the possibility of recovering an additional piece of information which is of key importance in aeroelasticity: the loads.

To start with, the wing reconstruction algorithm is designed to find the load distribution that deflects the wing in such a way that it matches the deflected marker grid. The integration of this load distribution along the span of the wing can be used to recover the total load on the wing, which can be compared to the force balance measurements taken in the wind tunnel. In the current study, the load distribution q_{ufm} is constant and that integration is therefore reduced to a simple multiplication by the span of the wing.The results of this comparison will be shown in Chapter 5.

4.4.1. Separation of inertial and aerodynamic loading

As mentioned before, one of the shortcomings of the wing reconstruction algorithm is the assumption of a constant loading acting on the wing, which prevents the detection of any kind of local changes in the loads along the span.

However, local information can be obtained/estimated for the section where PIV measurements were conducted. Here, the PIV velocity field can be used to estimate the aerodynamic loading by means of the Kutta-Joukowski theorem, and the marker tracking data can be used to estimate the inertial loading.

Aerodynamic loading based on circulation

The Kutta-Joukowski theorem is a fundamental theorem in aerodynamics that relates the lift generated by a two-dimensional airfoil to the density, freestream velocity and circulation around it. It is a potential flow theory meaning that the flow viscosity is neglected in its derivation, and it can be applied under steady/cuasi-steady flow conditions and under the assumption that the flow stays attached to the airfoil.

The theorem states that the lift per unit span L' generated by an airfoil is given by:

$$L' = -\rho_\infty U_\infty \Gamma \tag{4.9}$$

where ρ_∞ and U_∞ are the density and velocity of the freestream respectively, and Γ is the circulation around the airfoil section, defined as the line integral:

$$\Gamma = \oint_C \vec{u} \cdot d\vec{l} \tag{4.10}$$

where C is an arbitrary, closed contour around the airfoil outside of boundary layer regions and which does not contain any large flow separations.

Its application in this study is possible thanks to the measurements conducted on both sides of the wing section, and it involves taking the unsteady, volumetric flowfield measured with robotic PIV and taking different slices of it along the span of the wing. While the flowfield is volumetric, the physics captured in each of

those slices are mainly 2D, and thus a rectangular contour can be defined around the airfoil to compute the circulation. By repeating this process for different slices of the volumetric flowfield domain, the lift per unit length is obtained for the section where PIV measurements were conducted.

Inertial loading based on marker tracking

The inertial loading per unit span can be modelled as:

$$q_{inr} = \mu_{st} \frac{\mathrm{d}^2 w(z)}{\mathrm{d}t^2} \tag{4.11}$$

where μ is the mass per unit length of the wing and $w(z)$ is the span-wise deflection of the wing. The acceleration of each section of the wing can be computed using marker tracking information by computing the second derivative of each marker track in a given grid row and then averaging the accelerations of those markers.

On the other hand, the mass distribution can be approximated by a weight distribution μ_{st} estimated as:

$$\mu_{st} = \frac{m_{wing}}{b} \approx \frac{1.44\,\mathrm{kg}}{1.80\,\mathrm{m}} = 0.8\,\frac{\mathrm{kg}}{\mathrm{m}} \tag{4.12}$$

With this approach, the contributions of the aluminium block at the root of the wing and the wing tip masses are modeled as step changes in μ_{st} which only affect certain sections of the wing. In this investigation, the inertial load will be computed in Section 5.2.3 for the Z = 1500 mm plane, which is considered to be far enough from the tip to ignore the contribution of the tip masses. Also note that for this estimation, the total length of the model of 1.80 m has been used instead of 1.75 m. This is because the available weight is the one for the entire model and therefore includes the bottom section of 5cm used for the attachment to the aluminium block.

4.4.2. Wing Reconstruction Process: Flowchart

As shown in previous sections of this chapter, the wing reconstruction process involves several steps, which have been summarised in a flowchart in Figure 4.11. The nomenclature WOn/Woff differentiates cases where the wind tunnel was on and off respectively, and the "st" and "dyn" subscripts separate static deflection cases from dynamic ones (gusts).

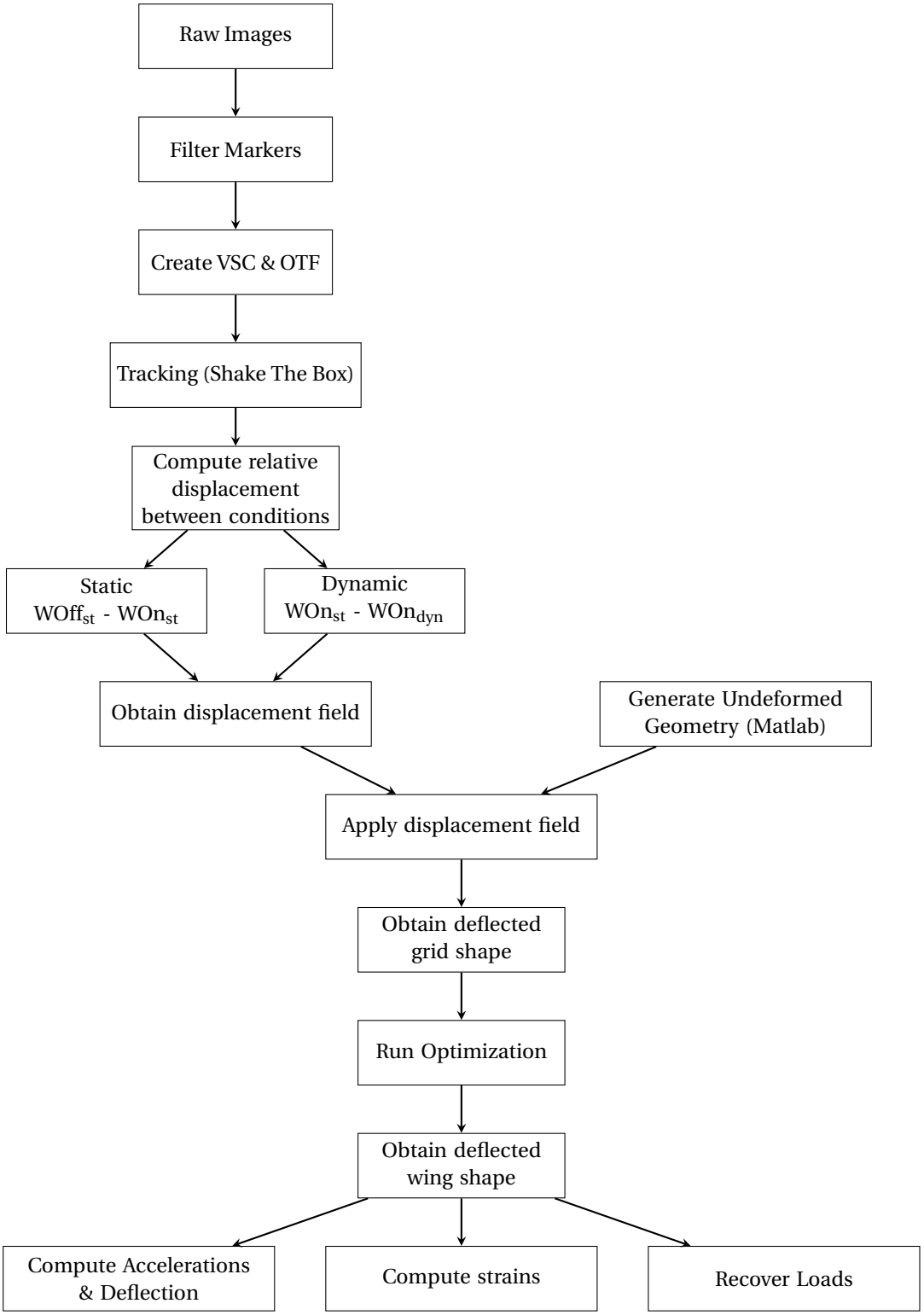

Figure 4.11: Flowchart showing the steps involved in the wing reconstruction process.

5

Results

This chapter presents the main results of this thesis. The experimental setup used to acquire the original, raw data has been described in Chapter 3, and the methodology that was followed to process that data and generate these results is covered in Chapter 4.

The discussion of the results starts with the analysis of the static case, where the static reconstruction of the wing at different freestream velocities is presented and validated through a comparison to optic fiber strain measurements. The corresponding steady robotic PIV measurements will also be examined. Secondly, the results for the gust encounter cases are discussed. The dynamic reconstruction of the wing is also compared to the accelerometers and the quality and evolution of the phase-averaged flowfields is analysed and compared to a theoretical approximation of the problem.

Finally, information about the different kinds of loads acting on the wing is also retrieved and presented for both the static and dynamic test cases.

5.1. Static deflection results

The analysis of the results starts with the reconstruction of the static deflection of the wing at different freestream velocities. The reconstructed geometry for the U_∞=14 m/s and U_∞=24 m/s cases is shown in Figure 5.1, being the angle of attack of the wing fixed at α_w=5°. The reconstruction seems to be good from a qualitative point of view, with a deflection that is close to zero near the root of the wing and progressively increases towards the wing tip. A maximum deflection of 18.2 mm is measured in the 14 m/s case, which subsequently increases to 48.9 mm in the 24 m/s. Considering that basic beam theory establishes a proportionality between load and deflection, and that in this case the aerodynamic loading increases by $(24/14)^2 = 2.94$ - due to the increase in dynamic pressure $1/2\rho_\infty U_\infty^2$-, the observed increase in deflection of $(48.9/18.2) = 2.69$ is within expectations.

It is also interesting to evaluate the reconstruction from a quantitative point of view. On one hand, the final value of the objective function after the optimization process can be examined. As explained in Section 4.3.2, this value is the average distance between the deflected marker grid measured with robotic PIV and the wing surface that is reconstructed afterwards. The exact value for each case is listed in Table 5.1, showing that the reconstruction error with respect to the deflected grid measured by robotic PIV is of the order of 1mm. This error originates from two sources:

1. **Misalignment of the deflected grid**. As shown in Figure 4.10, the deflected marker grid does define a somewhat smooth surface, but it does suffer from some misalignment between markers. This misalignment - even if small - is mostly random and not consistent with a smooth surface, meaning that it will inevitably contribute to the error of the reconstruction algorithm which is designed to reconstruct the entire, smooth surface of the wing and not local features. The misalignment can originate both from the performance of STB when tracking markers, but it is suspected that it is mostly caused by the

positioning error described in Section 4.2.3. The positional uncertainty of the CVV probe along its main axis is another contributing factor.

2. **Wing reconstruction algorithm**. The reconstruction approach is based on a very simplified structural model and load assumption, meaning that some of the real physics at play in the aeroelastic deformation might not be recoverable. An obvious example of this is limiting the degrees of freedom of the model to only one (bending), which excludes phenomena such as bending-torsion coupling.

Further insight into this matter can be obtained by exploring the spatial distribution of the error over the span of the wing. This is shown in Figure 5.2. For both cases, it is observed that the disagreement between the reconstructed wing and the grid is mostly concentrated near the wing tip region. In the case of the error in the Y direction ε_Y, it stays below 1mm in general in the 14 m/s case, although it increases considerably in the 24 m/s case to over 2mm at the wing tip. Local increases/drops in error which are inconsistent with a smooth gradient from the root of the wing to its tip are likely originated by the positioning error affecting the markers and the fact that we are only using their relative displacement between loading conditions instead of their absolute positioning.

On the other side, the map error in the X direction ε_X shows a gradual increase from root to wing tip in both the 14m/s and 24m/s case. The existence of this gradient is a possible indication that part of the wing structural response is not being captured due to the simplifications of the beam model used for the reconstruction, such as the restriction to 1DOF or the constant load assumption. Since this appears in the X component in particular, this could be an indication of the introduction of torsional effects, although in that case the sign of ε_X should change across the mid-chord of the wing.

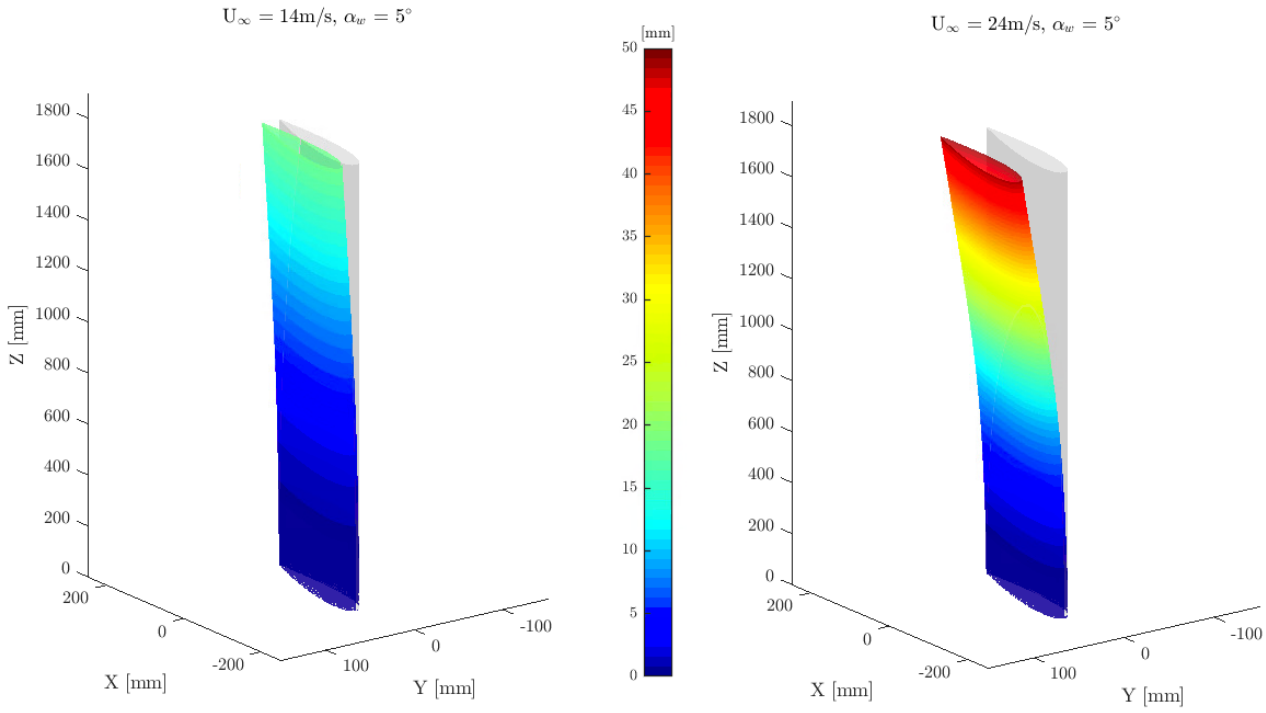

Figure 5.1: Reconstruction of the static deflection of the wing at U_∞= 14m/s and U_∞= 24 m/s. Surfaces are colored by the magnitude of the deflection in Y direction. Reference position of the wing is shown in gray.

U_∞ [m/s]	α_w [°]	Max. Δw [mm]	Average Fit Error $\overline{x}_{err}$ [mm]
14	5	18.2	0.83
24	5	48.9	1.57

Table 5.1: Quantitative results for the reconstruction of the wing in the U_∞= 14m/s and U_∞= 24m/s cases.

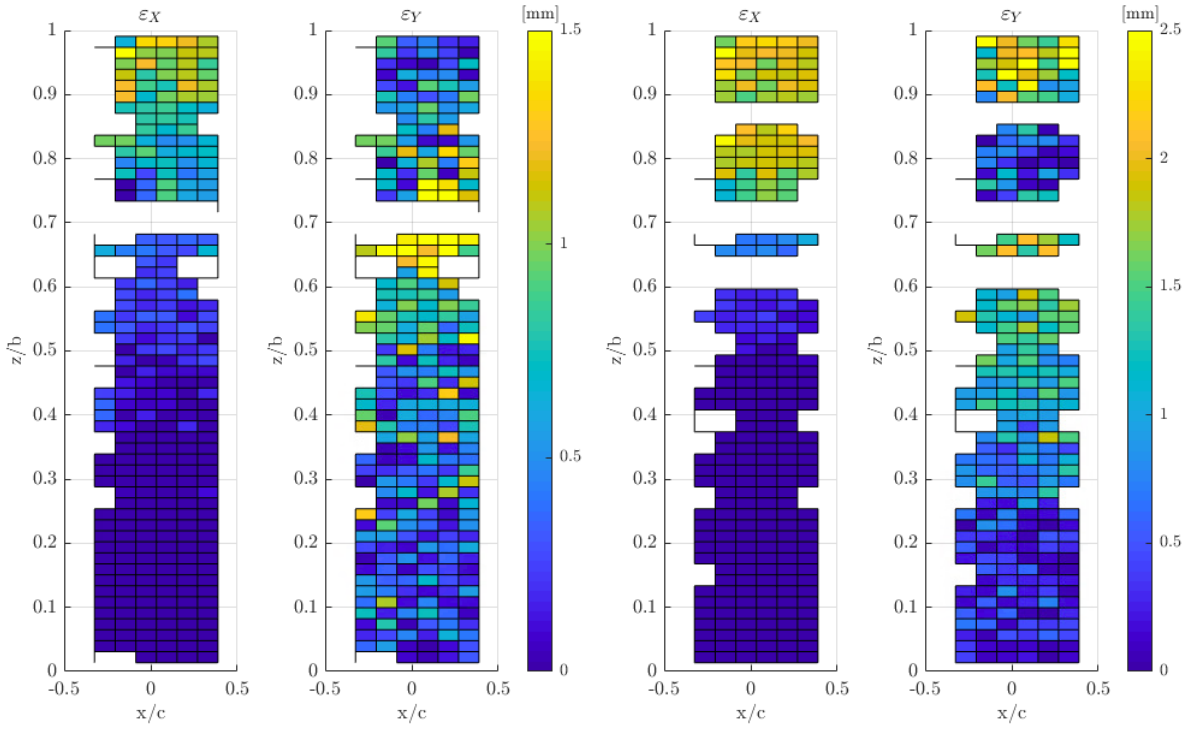

a) 14 m/s b) 24 m/s

Figure 5.2: Maps showing the wing reconstruction errors ε_X and ε_Y in the X and Y direction respectively, along the span of the wing in the U_∞= 14m/s (a) and U_∞= 24m/s (b) cases. Missing spots correspond to markers that could not be captured due to moving out of the field of view of the cameras.

5.1.1. Comparison with optic fiber strain measurements

The previous analysis of the reconstruction error examines how well the reconstructed wing matches the deflected shape of the marker grid. However, this cannot be considered as a validation for the reconstructed wing geometry since it depends on the marker tracking results themselves. Therefore, an independent measurement must be used for this purpose. This section discusses the comparison between the information generated by the wing reconstruction algorithm and the data measured by the strain fiber embedded on the laminate that forms the wing skin.

The marker-based strain measurements are generated by first considering the wing in an undeformed state and taking the line along which the fiber is placed on the wing model, at approximately the mid-chord of the wing. That line is then divided into segments of known length to determine the local deformation. After this, the deformed shape of the wing is generated and the same line is extracted from the model. The lengths L of the segments of that line are then compared between the deformed and undeformed state according to the definition of strains:

$$\varepsilon = \frac{\Delta L}{L} \tag{5.1}$$

An important factor in the comparison between the strains measured by the fiber and the reconstructed ones is the fact that in the model, the fiber is bounded to the inner side of the wing skin laminate, whereas in the wing reconstruction model the skin has zero thickness. This is a simplification of the model and it could affect the comparison slightly. In addition, the fact that the position of the strain fiber is not known exactly is another contributor to the uncertainty in the comparison.

The results of the comparison between the optic fiber and the reconstructed strains are presented in Figure 5.3 for both the U_∞= 14 m/s and U_∞= 24 m/s cases. It can be observed that, in a qualitative sense, the reconstruction based on the beam model agrees well with the shape of the strain distribution measured by the fiber in both cases. Some important features are the trend towards zero deformation at the wing tip as a

consequence of the drop in load, and most importantly the discontinuity in the strain distribution at z/b = 0.33. This jump is caused by the change in the laminate thickness - and therefore stiffness - in the real wing according to Figure 4.8. The strains rise significantly after the jump due to the sudden drop in stiffness.

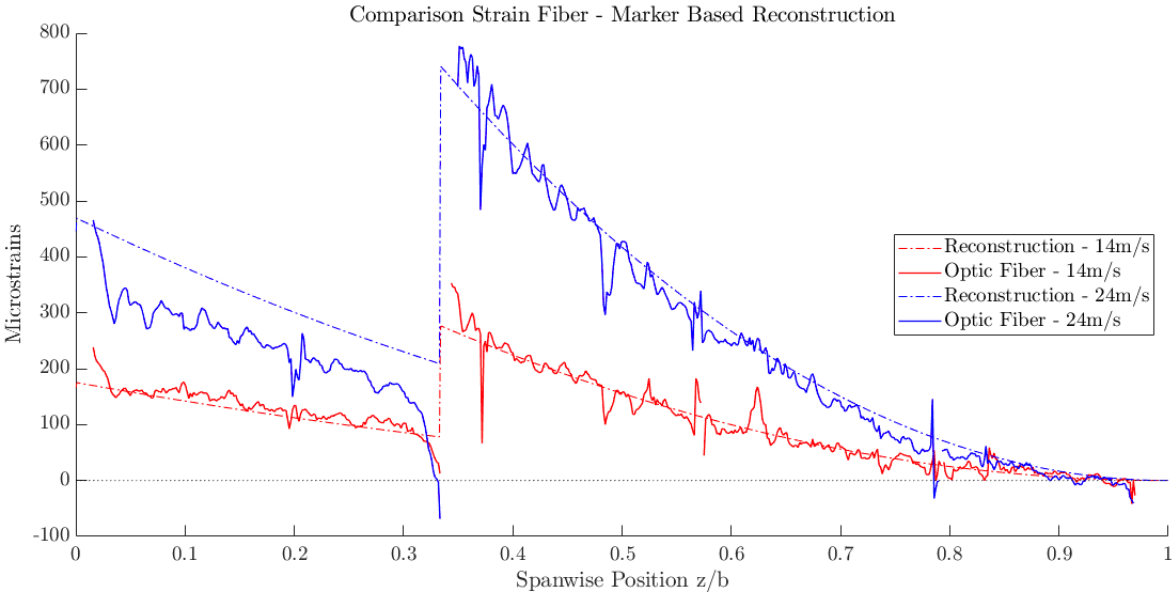

Figure 5.3: Comparison between the optic fiber strain measurements and the results from the marker-based wing reconstruction.

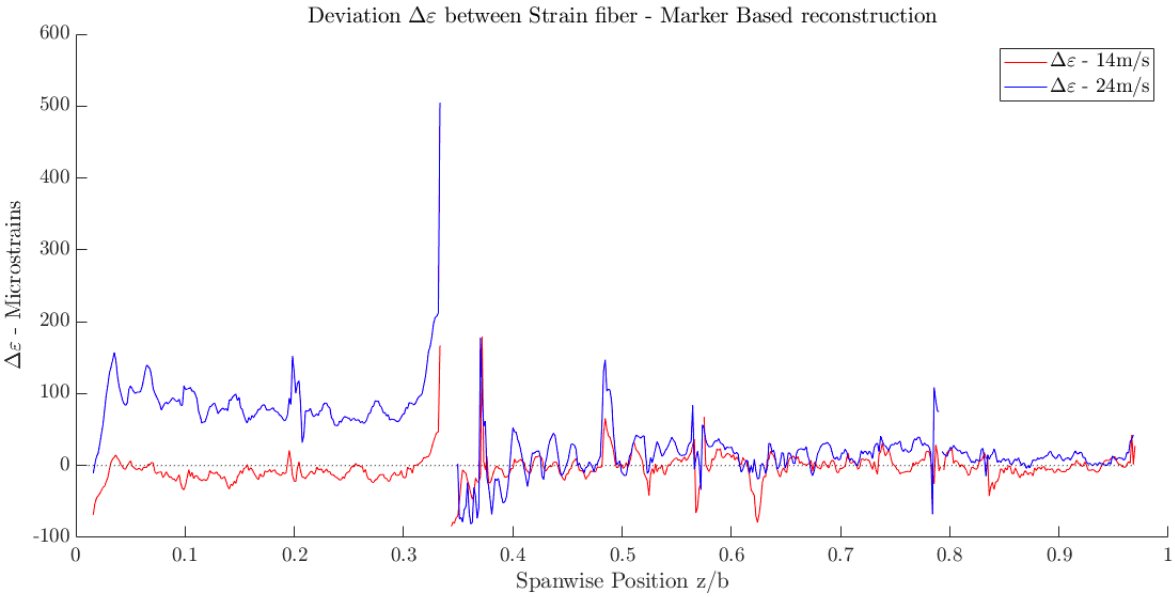

Figure 5.4: Deviation between the strain measured by the optic fiber and the strain reconstructed using marker data.

Additionally, Equation 5.1 shows that the strain is a purely kinematic property, meaning that computing them only requires an accurate description of how a surface is being deformed. In this study, that information is provided by the markers and used by the wing model to reconstruct the deformed wing surface. The agreement between the optic fiber and the wing model will therefore largely depend on two factors: the ability of the marker grid to measure the deformed wing surface and the ability of the wing model to reconstruct a wing geometry that fits that surface optimally. In this sense, a detailed examination of the comparison results reveals two main observations regarding the disagreement between the two measurements:

- In both cases, the reconstruction underpredicts the jump in strain at z/b = 0.33 or z = 583 mm. The magnitude of this jump is a function of the stiffness ratio EI_2/EI_1, and these results could suggest that

the real stiffness ratio is slightly different from the one extracted from the FEM model. A lower value ($EI_2/EI_1 \sim 0.25$) of the ratio has been found to give a better agreement with the strain fiber, but its use has been discarded due to the lack of evidence to support that choice.

- While the reconstruction very slightly underpredicts the value of the strains in the U_∞= 14 m/s case and overpredicts it in the U_∞= 24 m/s one, the maximum disagreement in both cases is located in the lower half of the wing. This can be explained considering that this region is the one subject to higher loads since it supports the sections of the wing above it. This means that the load distribution acting on the wing will significantly affect the deformation in this region and thus the strains. Therefore, the constant load assumption used in the implementation of the beam model (see Section 4.3) could be part of the cause of this behaviour.

These factors are related to the wing reconstruction model, although as mentioned before, the positioning of the markers can also influence the results. Regarding this aspect, the fit error committed by the reconstruction algorithm is listed in Table 5.1 for both cases. No validation data for the absolute 3D positioning of the wing in space (such as laser vibrometer data) is available.

Perhaps one of the most important observations is the difference in agreement between the 14 m/s case and the 24 m/s case. While the reconstruction matches the fiber very closely in the 14 m/s case, much higher disagreements can be observed in the root region of the wing in the 24 m/s case. This is likely to be an indication that the wing deformation becomes more complex as the aerodynamic loading increases. Due to the level of simplification used in the beam model, it is possible that it cannot capture well cases of high deflection of the wing where this complexity appears.

However, despite the simplicity of the wing reconstruction model, the issues affecting the positioning of the markers in space and the aforementioned factors, the deviation $\Delta\varepsilon$ between the reconstructed strains and the ones reported by the optic fiber is relatively small in comparison to the maximum strain measurement at each inflow velocity, as shown in Figure 5.4. This is a reinforcing fact which suggests that a more robust methodology in future experiments could deliver improved results.

5.1.2. Steady PIV measurements

The results for the time-averaged PIV flowfield at α_w = 5° and U_∞ = 14 m/s are presented here, together with the reconstructed wing surface. The presentation will start with the analysis of some 2D results and will continue with a visualization of the flow in 3D.

Note on the wing surface reconstruction methodology

All the flowfield measurements shown in this section and later in Section 5.2.2 are presented together with a representation of the wing surface which has been reconstructed from marker information. In this case, only the wing section corresponding to the location where the PIV measurements are conducted is presented instead of the entire wing. However, the wing surface of this section is reconstructed using a different and simpler approach to the one described in Chapter 4.

Due to the way the data was acquired, the measurements containing both flow tracers and structural markers do not have a reference position measured when the wing was undeformed. Therefore, it is not possible to follow all the steps listed in the flowchart presented in Section 4.4.2 to reconstruct the entire wing geometry. Therefore, the alternative approach used instead involves approximating the wing section as a straight, perfectly rigid surface. This surface is still reconstructed using marker information, but only the section where the flowfield is measured is recovered.

Modelling the wing section as straight and perfectly rigid is considered to be a valid assumption given that it corresponds to a location close to the wing tip where the deformation and curvature of the wing are small, as shown by the strain measurements presented in Figure 5.3. Additionally, a comparison between the perfectly rigid surface and the flexible one was conducted, showing that the average difference between them was of the order of 0.25mm.

2D visualization

Figure 5.5 shows different flowfield variables at the Z = 1500 mm plane. This plane has been chosen because it is the one at which the volumetric domain measured with robotic PIV covers a wider area around the wing.

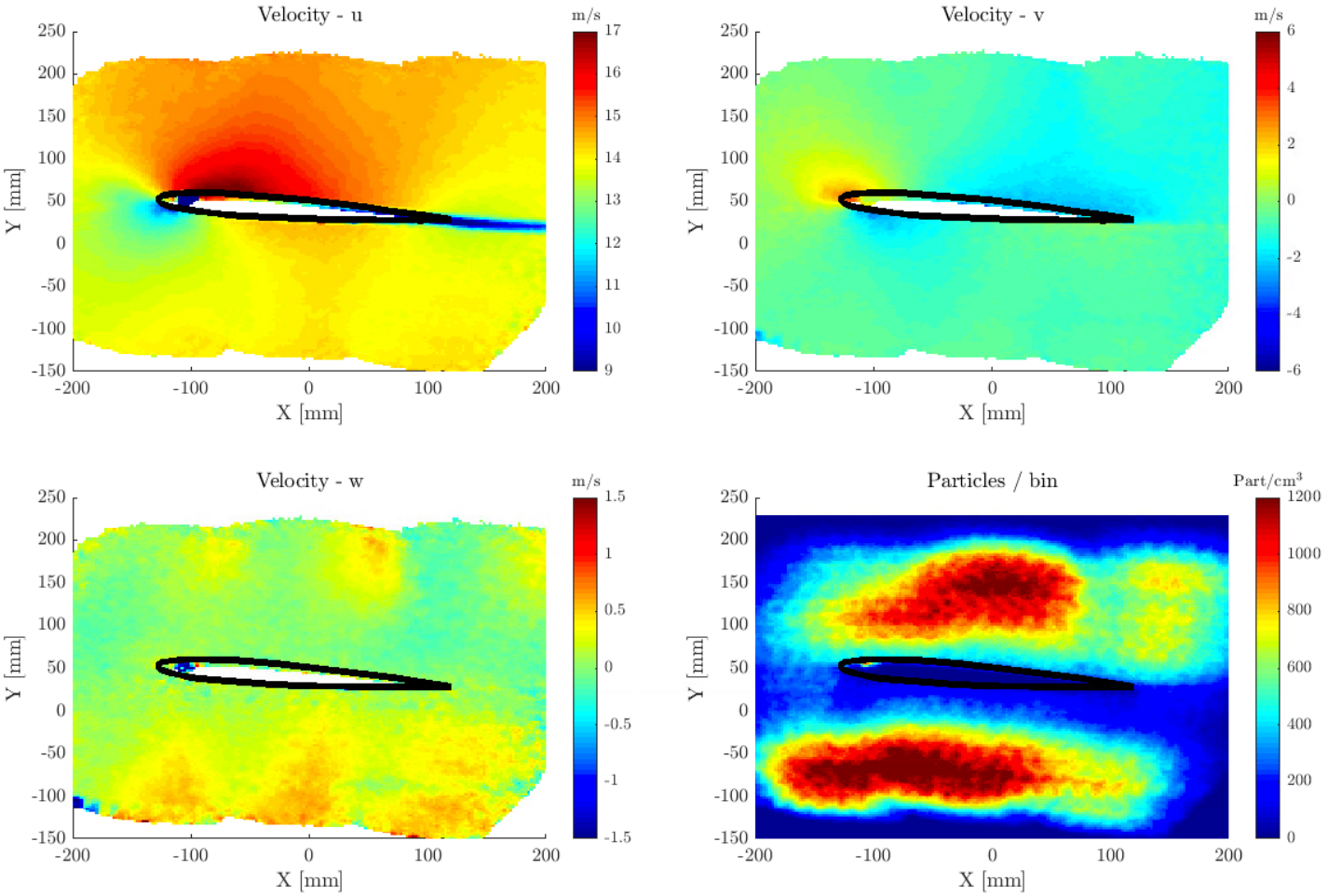

Figure 5.5: Top view of the wing and different flowfield quantities in the Z = 1500mm plane. Bins of 1cm^3 with a 75% overlap between them were used for the ensemble averaging of 11000 images. U_∞= 14 m/s, α_w = 5°.

The flowfield shows the typical features of the flow around an airfoil. Looking at the streamwise component of the velocity u, the flow first decelerates from the freestream value of 14m/s and reaches the stagnation point on the pressure side of the wing, close to the leading edge. The flow then accelerates over the airfoil reaching a maximum speed of around 17 m/s and then leaves the airfoil at the trailing edge producing a wake that is clearly recognizable as a low-speed velocity region. The crossflow velocity component v is consistent with the previous description, and the vertical component w is small in magnitude, indicating that the flow is mainly 2-dimensional at this location.

The merging between the different PIV volumes used to measure the flow around the wing from both sides is also good, since no noticeable spatial discontinuities can be observed in any of the flow components. On the other side, a possible interference from the CVV flow can be observed on both the pressure and suction sides at the edges of the domain. In particular, the streamwise velocity component plot shows an acceleration of the flow on the pressure side of the wing at the X = [-150 -50 100] mm, Y = -130 mm locations. The interference can also be appreciated on the w component plot, also affecting the pressure side to a greater extent, although the magnitude of the perturbation is small as indicated by the color scale.

The results also show the particle concentration, which in this case is not a limitation since a total of 11000 images per PIV view was used to generate the results. The results indicate concentrations of over 200 particles

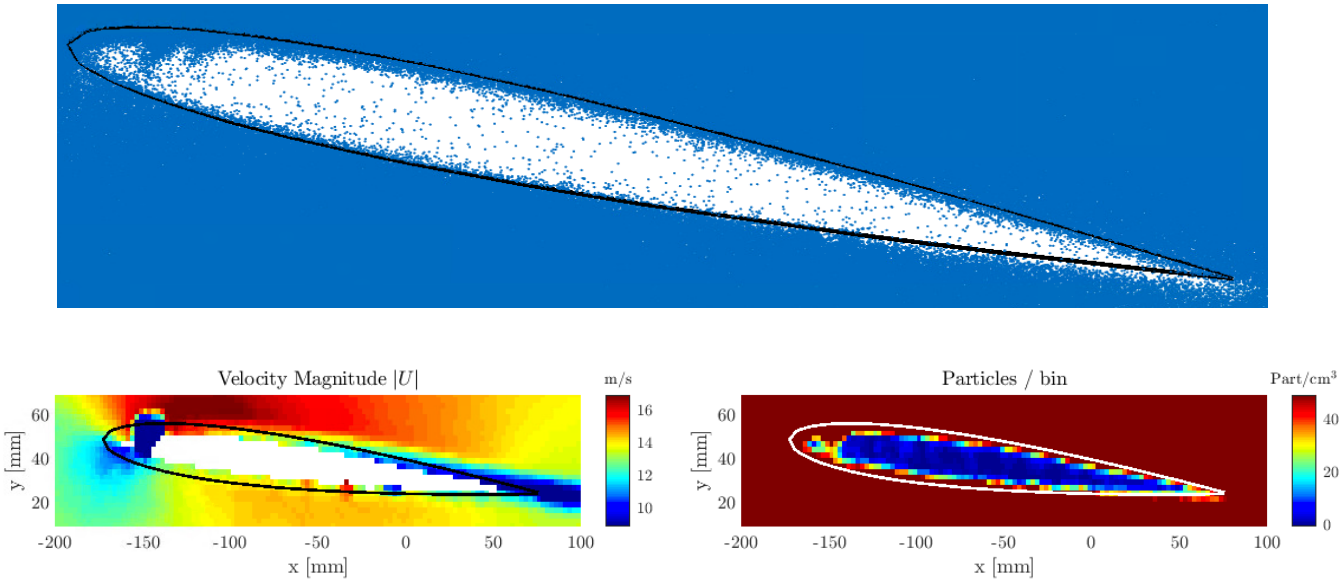

Figure 5.6: Top: Illustration of the overlap between the particle field measured with STB and the surface reconstructed based on marker data. Bottom: Close up view of the Z = 1500 mm plane near the wing surface, showing the overlap between the measured flowfield and the reconstructed surface. U_∞= 14 m/s, $\alpha_w = 5°$.

over a large domain around the wing, reaching maximums of over 1000 particles per bin.

It is also interesting to assess the compliance between the flowfield and the wing surface reconstructed with marker information. Some insight into this matter is presented in Figure 5.6. The top view displays the particle field used as an input for the ensemble-averaging process and the wing surface, showing a good agreement between the position of the flow tracers and the wing. Some areas of high particle concentration are positioned inside the reconstructed wing volume, especially on the suction side near the leading edge. This is caused by soap accumulation in the zig-zag strip, creating false particles. Additionally, some higher overlap can be observed along the suction side than along the pressure side, as well as an area with low particle seeding near the trailing edge. This could point towards a small positioning issue affecting the PIV view used to cover the trailing edge area of the pressure side of the wing.

Figure 5.6 also shows that any particle located inside the wing volume will cause the bins resulting from the ensemble-averaging process to overlap with the wing surface. Luckily, those bins show particle concentrations much lower than the ones outside the surface, suggesting that these spurious bins could be eliminated by establishing a minimum required concentration.

3D flow visualization

While 2D visualizations of the flowfield are useful to analyze quantities in detail, the data produced by robotic PIV is volumetric and allows the generation of 3D visualizations as the one shown in Figure 5.7. The steady flowfield is shown once again, with a planar plot of the Z = 1500 mm plane and two isosurfaces of the velocity magnitude $|U|$ which allow the visualization of the wake region at the trailing edge as well as the maximum flow speed region near the leading edge. A secondary low velocity region can be observed at some locations near the leading edge of the wing, which is believed to be originated by soap contamination at the location of the zig-zag strip on the suction side.

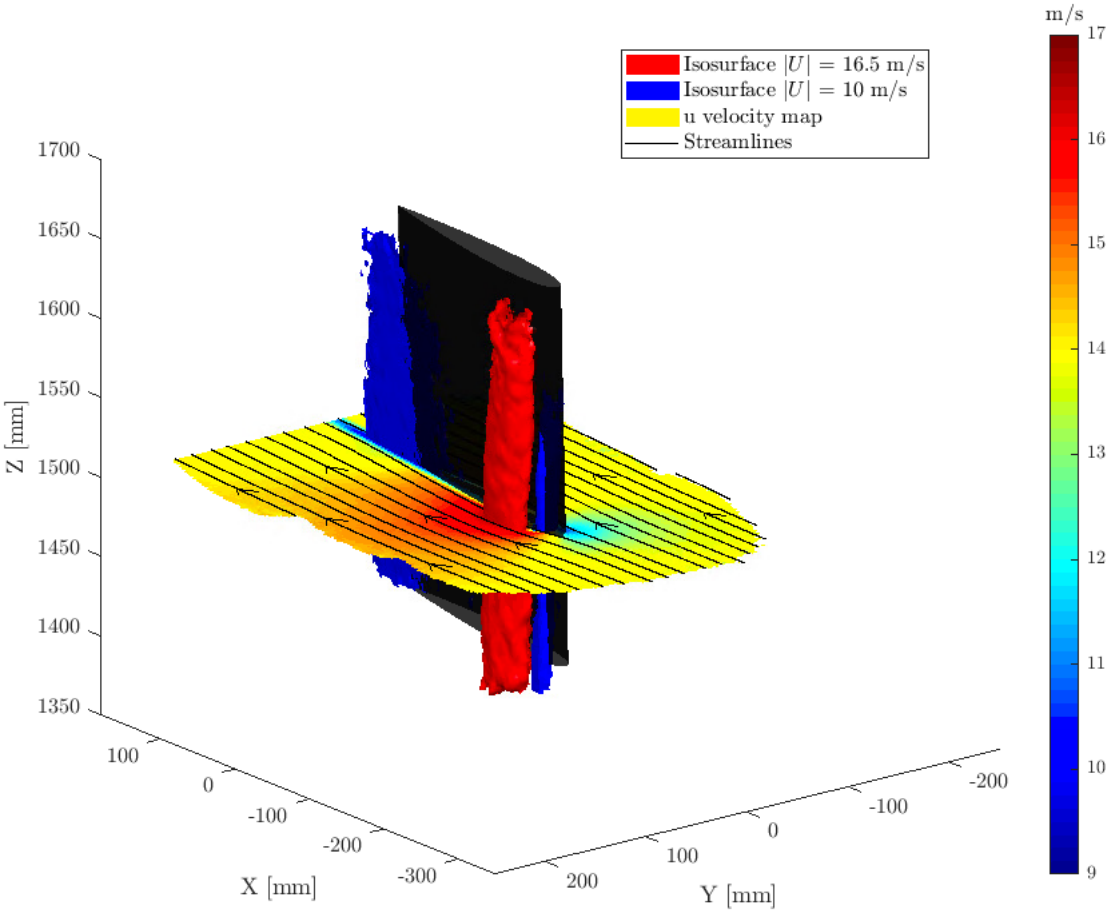

Figure 5.7: Visualization of the steady flowfield at U_∞ = 14 m/s and α_w=5°. The Z = 1500 mm plane is colored by the u component of the velocity.

5.1.3. Static load: comparison to force balance

As the final result in this Section, a preliminary evaluation of the aerodynamic loading acting on the wing is presented in Figure 5.8, where the load per unit span F'_y is calculated based on the circulation of the flowfield around the wing as described in Section 4.4.1. Measurements are only available over a limited length of around 10cm due to the size of the volumetric flowfield.

The loading is compared to the one reported by the force balance, if modeled as uniform. While this is a significant simplification, it does allow a comparison between the measurements in terms of order of magnitude, showing a good agreement. Another interesting feature is the drop of the measured aerodynamic loading towards the tip of the wing, which is to be expected due to wing tip losses as the location of the section where the PIV measurements are conducted is close to the end of the wing.

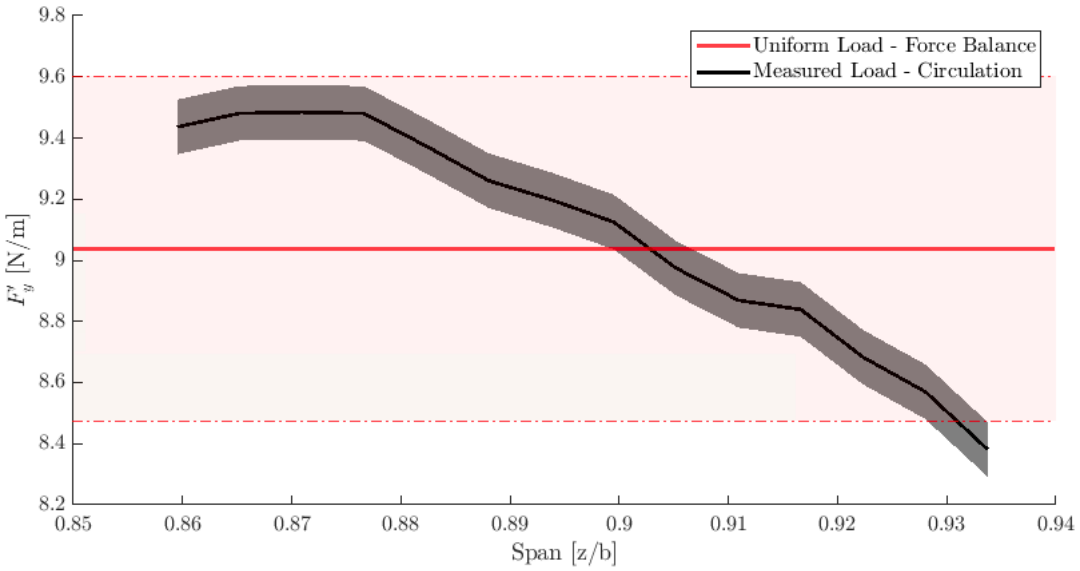

Figure 5.8: Comparison between the local aerodynamic loading computed using the circulation and the loading according to the balance, if the loading is modelled as uniform.

Both measurements are displayed with a confidence region which has been computed in the following way for each case:

- Circulation: The circulation was computed using contours of different sizes around the airfoil. The obtained values are used to compute the mean circulation at each spanwise position (displayed in solid black) and the standard deviation of the circulation. The shaded area of the circulation plot corresponds to ± 2 standard deviations with respect to the mean, which amounts to a 95% confidence interval if the noise in the circulation measurements is modeled as a normal distribution.
- Force Balance: The manufacturer of the balance ([3]) reports a calibration error of the balance of 0.23% of the nominal load. However, the observed noise in the force balance signal was well below that estimation and therefore, the uncertainty region for the balance measurement is computed based on the measurements themselves. 8 individual measurements are used to once again compute the mean and standard deviation of the output signal of the balance, and the shaded region (red) in Figure 5.8 corresponds to ± 2 standard deviations. This confidence interval should cover any noise inherent to the balance as well as any other effects such as repeatability of the experiment, aerodynamic interference from the robot or disturbances in the wind tunnel jet.

5.2. Gust encounter results

Following the previous analysis of the static results, the dynamic results corresponding to the cases of gust encounters are presented here.

First, the dynamic reconstruction of the wing will be validated through a comparison with the readings of the accelerometers placed at the wing tip. Secondly, the phase-averaged PIV results for the continuous gust case will be analysed. Finally, the reconstruction of the different kinds of dynamic load acting on the wing will be discussed.

5.2.1. Reconstruction of wing kinematics - Discrete Gusts

Comparison to accelerometers

As mentioned in the description of the experimental setup used during the wind tunnel campaign, the wing was fitted with two tri-axial accelerometers placed its tip. The purpose of these sensors is to provide a validation measurement for the dynamic reconstruction of the wing geometry.

The signal of the accelerometers is recovered from the wing reconstruction process by extracting the positional information over time of the wing tip. This signal is then fitted with a polynomial and derived over time to extract the acceleration.

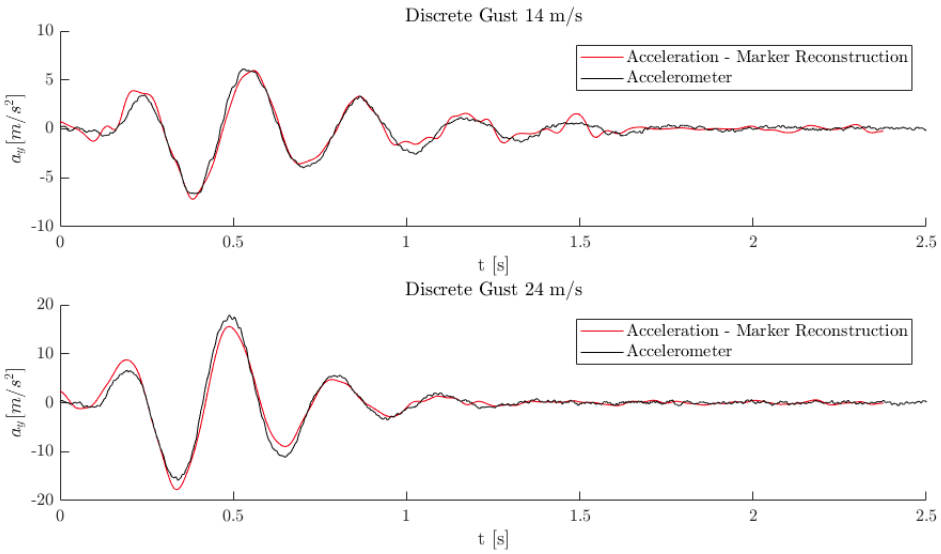

Figure 5.9: Comparison between the accelerometer readings in Y direction and the dynamic reconstruction of the wing during the two cases of discrete gust encounters. The validation readings belong to the leading edge accelerometer.

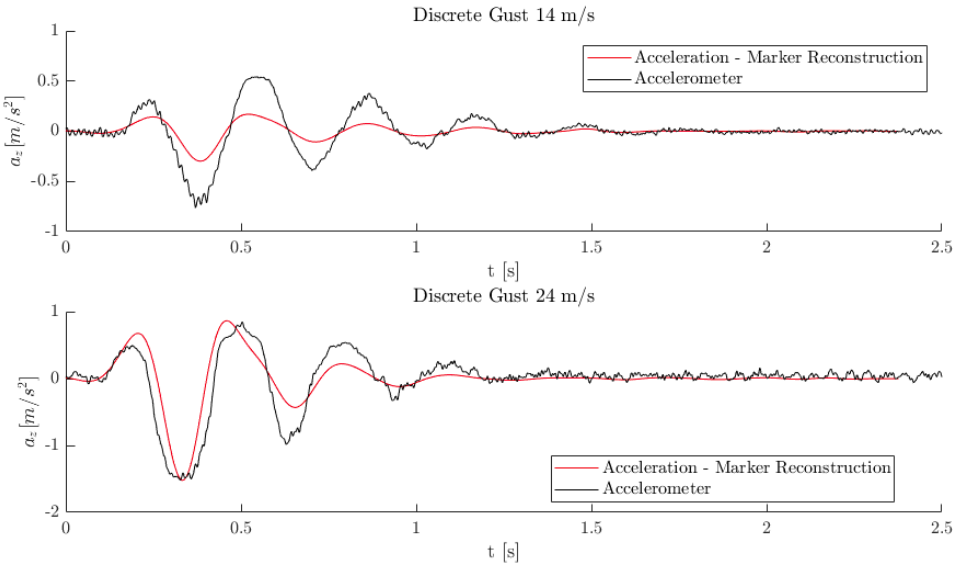

Figure 5.10: Comparison between the accelerometer readings in Z direction and the dynamic reconstruction of the wing during the two cases of discrete gust encounters. The validation readings belong to the leading edge accelerometer.

The results of this comparison are shown in Figure 5.9 and Figure 5.10. The figures show the acceleration signals for both the Y and Z directions in the cases of a discrete gust encounter at 14 and 24m/s. As a reminder, the frequency of the gust was f_G=3 Hz and the maximum deflection of the gust vanes of $\delta_G = 10°$. Also, before discussing the results it is worth mentioning that a cross-correlation analysis of the original signals indicated that a time offset of approximately 0.02 seconds existed between the accelerometers and the reconstructed signal. This offset has been judged to be caused either by the triggering of the measurement systems or artificially introduced by the data-reduction process. The offset was subsequently corrected.

Figure 5.9 shows the acceleration in the Y direction perpendicular to the chord of the wing, that is, the direction of maximum deflection. For both the 14m/s and 24m/s case the comparison shows an excellent

agreement between the accelerometer and the reconstructed signal, both in terms of amplitude and frequency. Some small differences in amplitude can be observed in the 24m/s case, especially during the first four peaks where the magnitude of the acceleration is over $10 m/s^2$. These small mismatches could be another indication that the wing reconstruction model loses validity for large deflections of the structure.

On the other hand, Figure 5.10 shows the acceleration measurements in the vertical direction. This acceleration is caused by the change in height caused by the rotation of the wing sections along their chordwise directions as a consequence of the bending. As it can be seen by the scale in the plot, this is a much smaller feature of the structural response. Nonetheless, a correlation between the accelerometer reading and the reconstruction can be observed. The reconstructed signal shows a correct behaviour in terms of frequency, and its amplitude also matches the reference for oscillations of above $1 m/s^2$, while smaller peaks are underpredicted. This underprediction is likely caused by either the positional error affecting the marker grid or by an inability of the wing reconstruction model to capture such small effects.

However, the overall conclusion is that the dynamic response of the wing is well captured using the proposed approach, showing an excellent agreement in the main direction of deflection and promising results regarding detailed features such as the vertical acceleration.

Wing deflection during gust encounter

The previous section offered a quantitative assessment of the accuracy of the wing reconstruction during a time-dependent event. While insightful, this is done using the pointwise information corresponding to the accelerometers, restricting the full potential of the proposed measurement approach which is capable of reconstructing the entire wing geometry.

Following this idea, Figure 5.11 shows the instants of maximum and minimum deflection of the wing with respect to the static deflected shape shown in black. The results correspond once again to the discrete gust encounters at 14 m/s and 24 m/s, for a gust generator vane amplitude of $\delta_G = 10°$ and a frequency f_G =3 Hz. The exact wing tip deflection values measured are listed in Table 5.2. This values are measured with respect to the static deflected position.

As logical, both the maximum and minimum deflection are higher in the 24m/s as the loads are higher. Also, there is a clear asymmetry in the deflection of the wing towards its pressure side ($\Delta Y > 0$). This is caused by the fact that the gust velocity profile follows a "1-cosine" law, meaning that only a positive transverse velocity component v is induced by the gust. Also, the angle of attack of the wing was once again set to α_w=5°, which obviously favours the deflection towards the Y>0 side.

f_G [Hz]	δ_G [°]	Flow Speed [m/s]	Max. Tip Deflection [mm]	Min. Tip Deflection [mm]
3	10	14	34	-14
3	10	24	85	-30

Table 5.2: Values of the wing tip deflection for the discrete gust encounters at 14m/s and 24m/s. Dynamic deflections are measured with respect to the static deflected position.

5.2.2. Phase - Averaged PIV measurements

The previous sections have shown the marker tracking information acquired with the robotic PIV system and processed with STB can be used to successfully reconstruct the dynamic response of the wing. This section will focus on showing that this can be done while conducting aerodynamic measurements simultaneously.

For this, the results of the continuous gust excitation case are presented. These results (flowfield and structure) have been extracted from images containing both markers and flow tracers. These are separated form each other and subsequently used to reconstruct the wing surface as well as the flowfield, which is phase and ensemble-averaged. This is done following the procedures described in Chapter 4. In particular, the flowfield is phase-averaged using a time kernel k_T = 1% resulting in 100 phases. Secondly, bins of $1 cm^3$ with an overlap of 75% between them are used for the ensemble averaging.

As a reminder, the continuous gust excitation case is defined by a freestream speed U_∞=14m/s, a fre-

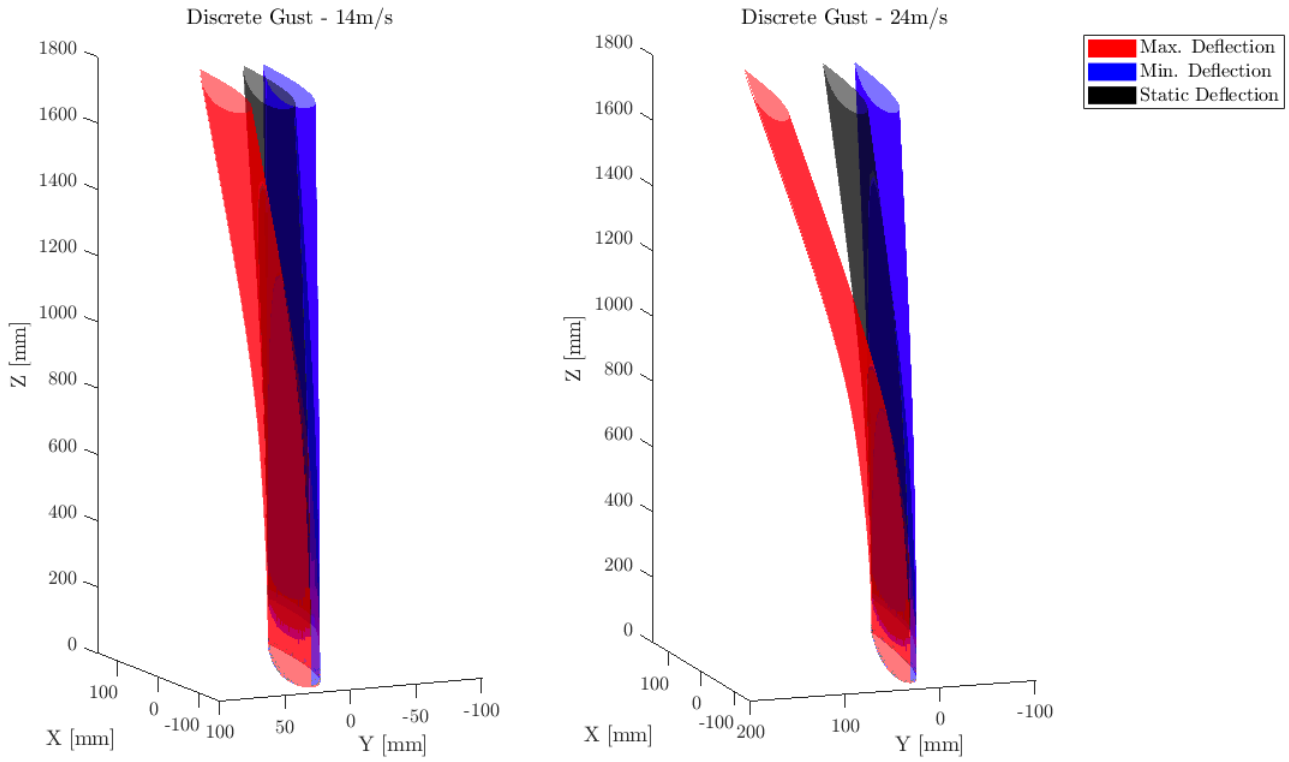

Figure 5.11: Shapes of the wing at the point of maximum and minimum deflection during the discrete gust cases. The static deflection is shown in black for reference. Note that the aspect ratio of the axes slightly alters the deflection of the wing along the span shown in the plot.

quency of 2Hz and a deflection of the gust vanes of δ_G=±5°. In this case, the gust profile follows a continuous sinusoidal motion instead of the "1-cosine" law, meaning that the gust profile is symmetrical, inducing both positive and negative transverse velocities. These parameters result in a reduced frequency of:

$$\kappa = \frac{\pi f_G c}{U_\infty} = 0.11 \tag{5.2}$$

which according to the classification proposed by Leishman [41] corresponds to a case where unsteady effects are relevant. The results will first discuss how the angle of attack and the loading on the wing are related over time, and how that relation compares to analytical unsteady aerodynamic models. Secondly, those results will be used to analyze the phase-averaged flowfields.

Evolution of the angle of attack

To better understand the physics at play during the continuous gust interaction, the relation between the aerodynamic loading on the wing and its effective angle of attack is discussed first. The circulation is used as an estimation of the loading, while the effective angle of attack is computed as:

$$\alpha_{eff} = \alpha_w + \alpha_G + \alpha_{st} \tag{5.3}$$

where α_w is the geometrical angle of attack at which the wing is set with respect to the inflow, α_G is the contribution of the gust and α_{st} is the angle of attack due to the oscillation of the wing. The last two values are computed as

$$\alpha_G = \arctan\left(\frac{v_G}{U_\infty}\right) \tag{5.4}$$

$$\alpha_{st} = \arctan\left(\frac{v_{st}}{U_\infty}\right) \tag{5.5}$$

being v_G the crossflow velocity component introduced by the gust profile and v_{st} the velocity of the wing surface in the y direction. The calculations are done at the Z = 1500 mm plane, where v_{st} is computed at the quarter chord point of the wing and v_G is calculated by sampling the flowfield along a vertical line 8 cm away from the leading edge of the airfoil and averaging the v component of the velocity. A longer distance would be desirable for this calculation, but this cannot be realised in the current measurements due to the domain limitations upstream of the airfoil. Also, it should be noted that the induced angle of attack caused by wing tip effects is not being considered separately since it is not possible to separate the gust angle of attack from the induced one based on the flowfield, and the gust angle of attack is considered to be the dominant contribution. This means that the measurement of the angle of attack induced by the gust already contains the contribution of the induced angle of attack.

The results are shown in Figure 5.12, where both the different angles of attack and the circulation around the airfoil are shown over a cycle of the wing-gust interaction. The variables are displayed over a non-dimensional time $t^* = t/T$ where t is the physical time and T is the duration of a cycle of the oscillation. In this case, the value of T corresponds to 0.5 s as a consequence of the excitation frequency of 2Hz.

The evolution of α_G shows that the gust generator produces an oscillation $\alpha_G \approx \pm 3.6^\circ$. This value is lower than the deflection of the gust generator vanes, but this is expected due to the behaviour of the gust generator which is described in detail in Lancelot et al. [39]. The reference mentions that, as an approximation, the maximum gust angle and the gust vane deflection are related by $\alpha_G \sim \frac{\delta_G}{2}$. This points towards a possible overestimation of α_G in this study, which could be caused by an interference coming from the wing due to the proximity of the measurement point to the leading edge. Additionally, the plot also shows that the contribution by the oscillatory movement of the wing α_{st} is small in comparison to that of the gust.

On the other hand, the bottom of Figure 5.12 shows that the instants of minimum and maximum load (as estimated from the circulation) lag behind the instants of minimum and maximum effective angle of attack respectively. This lag is estimated to be 0.06 s and it is expected due to the unsteadiness of the problem, as indicated by the reduced frequency.

Comparison between experimental and theoretical aerodynamic results

Despite the lack of aerodynamic validation measurements such as pressure taps, a qualitative assessment of the unsteady aerodynamic results can be conducted based on simplified analytical models. These models rely on important assumptions such as potential flow theory, thin-airfoil theory, fully attached flow and small perturbation theory, but they are capable of capturing the effects of several sources of unsteady aerodynamic loading. Periodic airfoil pitching and plunging motion and changes in angle of attack (gusts) are typical examples of these sources of loading.

This section will focus only on the application of these analytical results to obtain a comparison for the aerodynamic measurements conducted during the experimental investigation of this thesis. For a general introduction of unsteady aerodynamic theory, the reader is referred to the work of Leishman [41], where the basic results of Theodorsen, Sears and others are presented.

For the purpose of this comparison, it is useful to start by identifying the two main contributions of unsteadiness of the problem of this study. This can be done by splitting the gust-wing interaction in two main aspects:

1. Change in angle of attack caused by a sinusoidal gust
2. Oscillatory plunging motion of the wing due to its flexibility.

The first problem was addressed by Sears [65], who studied the response of a 2D airfoil when encountering a sinusoidal gust of the form:

$$v_g = v_0 e^{i\frac{2\pi}{\lambda_g}(U_\infty t)} \tag{5.6}$$

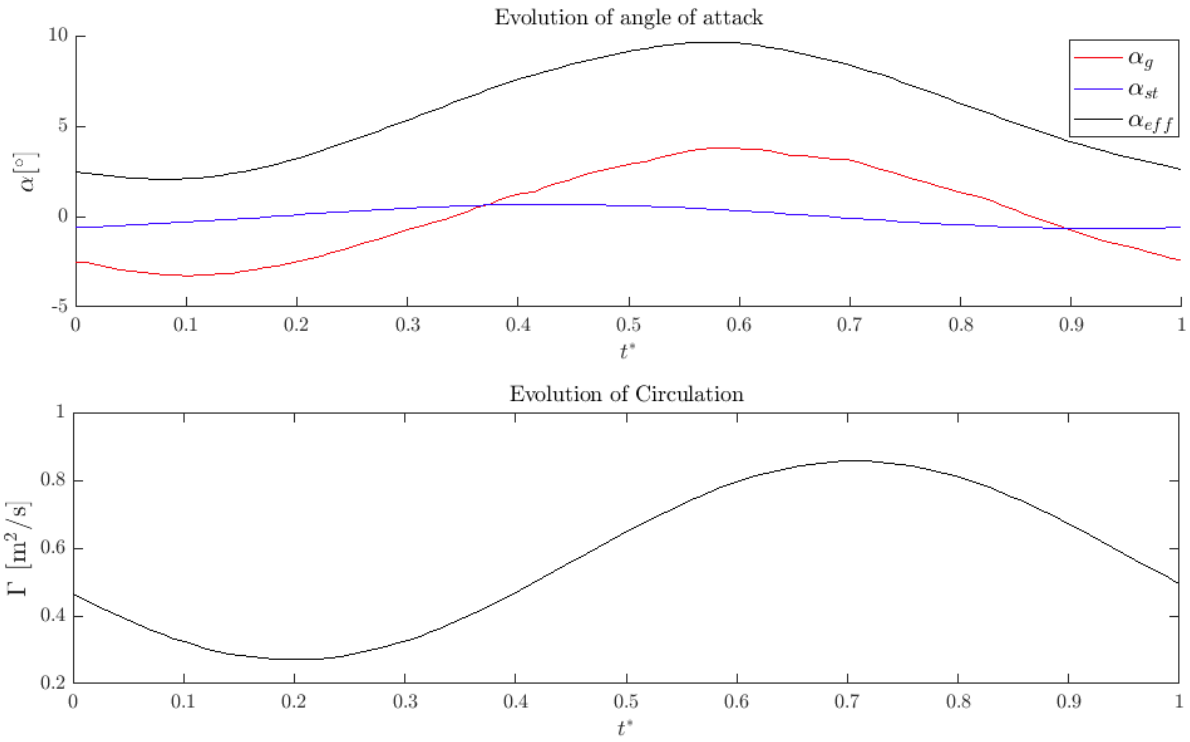

Figure 5.12: Evolution of the angles of attack and circulation over the phases.

where v_0 is the amplitude of the gust velocity profile and λ_g is the gust wavelength. The result for this excitation in terms of the lift coefficient is given by the following expression:

$$c_{l,gust} = c_{l\alpha}\frac{v_0}{U_\infty}S(\kappa)e^{\frac{i2\pi U_\infty t}{\lambda_g}} \tag{5.7}$$

where $c_{l\alpha}$ is the slope of the $c_l - \alpha$ curve of the airfoil and $S(\kappa)$ is Sears' function.

On the other hand, the evolution of the lift coefficient during the periodic plunging motion of an airfoil of the form $y = y_0 e^{i\omega t}$ can be computed from Theodorsen's results (Theodorsen [68]) as:

$$c_{l,plunging} = \left[c_{l\alpha}\kappa(iF(\kappa) - G(\kappa)) - \pi\kappa^2\right]\frac{2y_0}{c}e^{i\omega t} \tag{5.8}$$

where $F(\kappa)$ and $G(\kappa)$ are the real and imaginary parts of Theodorsen's function respectively. In addition, both Theodorsen's and Sear's results are based on linearized theory, meaning that the contributions of the gust and the plunging motion can be added to obtain the airfoil response the full interaction between the flexible wing and the gust. Furthermore, these results are only valid for 2D problems, which means that it is assumed that for the section of the wing being considered the flowfield is mainly 2D.

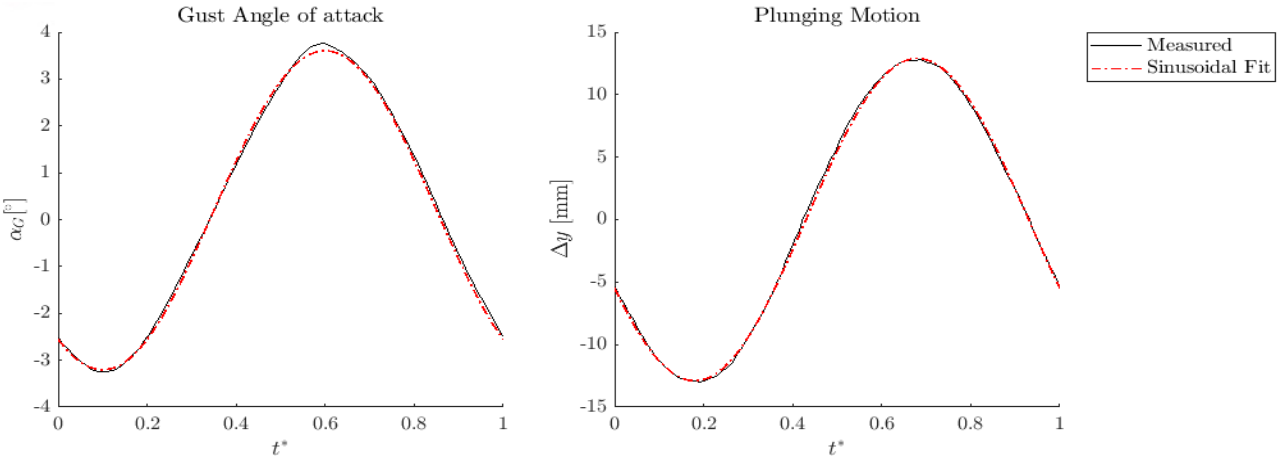

Figure 5.13: Comparison between the measured oscillations in gust angle of attack and wing deflection and the corresponding sinusoidal fits used as input for the analytical model.

Because the analytical results correspond to purely periodic excitations, the first step to establish a comparison is finding the laws $y(t)$ and $v_G(t)$ that describe the interaction between the wing and the gusts. This can be done by fitting a sinusoidal law to the measured angle of attack of the gust and to the oscillatory motion of the wing as shown in Figure 5.13. The excellent agreement between the fit and the measurement indicates that the periodicity of the experiment is good.

These laws can then be used as an input to Equations 5.7 and 5.8 to obtain the contribution to the lift coefficient from both the gust $c_{l,gust}$ and the plunging motion $c_{l,plunging}$. The two can then be added and compared to the measured lift coefficient, which can be computed based on the circulation as:

$$c_l = \frac{\rho U_\infty \Gamma}{q_\infty c} = \frac{2\Gamma}{U_\infty c} \tag{5.9}$$

Note that the lift coefficients $c_{l,gust}$ and $c_{l,plunging}$ are in reality the changes in c_l with respect to the steady value, which in this problem would be the value of the lift coefficient at $\alpha_w = 5°$ that has been computed based on the measurements presented in Figure 5.8.

The comparison between the analytical and experimental lift coefficients is shown in Figure 5.14. On the left, the evolution of the lift coefficient over the non-dimensional time t^* is shown, while the right side displays the c_l plotted against the effective angle of attack α_{eff}, showing a clear hysteresis loop both in the analytical and experimental cases. It can be seen that the agreement is good in terms of the amplitude of the lift oscillations, although a clear phase difference exists between the experimental and the analytical lift coefficient.

In addition, both plots in Figure 5.14 also show the quasi-static lift coefficient, which is simply computed as:

$$c_{l,quasi-steady} = c_{l\alpha}\alpha_{eff} \tag{5.10}$$

The comparison between the quasi-steady c_l and the unsteady experimental and analytical estimations clearly shows the unsteady aerodynamic effects at play during the wing-gust interaction. These are mainly a dampening in amplitude of the lift coefficient and the introduction of a lag between the quasi-steady and unsteady c_l.

This comparison shows that the experimental estimation of the unsteady aerodynamic loads based on the measurement of the circulation of the flowfield around the airfoil is capable of capturing unsteady effects qualitatively. However, it does not show how well those effects are captured. The existence of a phase difference between the analytical and experimental unsteady lift coefficients could suggest that the estimation of loads based on the circulation still suffers from some flaws, although it could also be an artifact introduced by the modelling assumptions used in the analytical models.

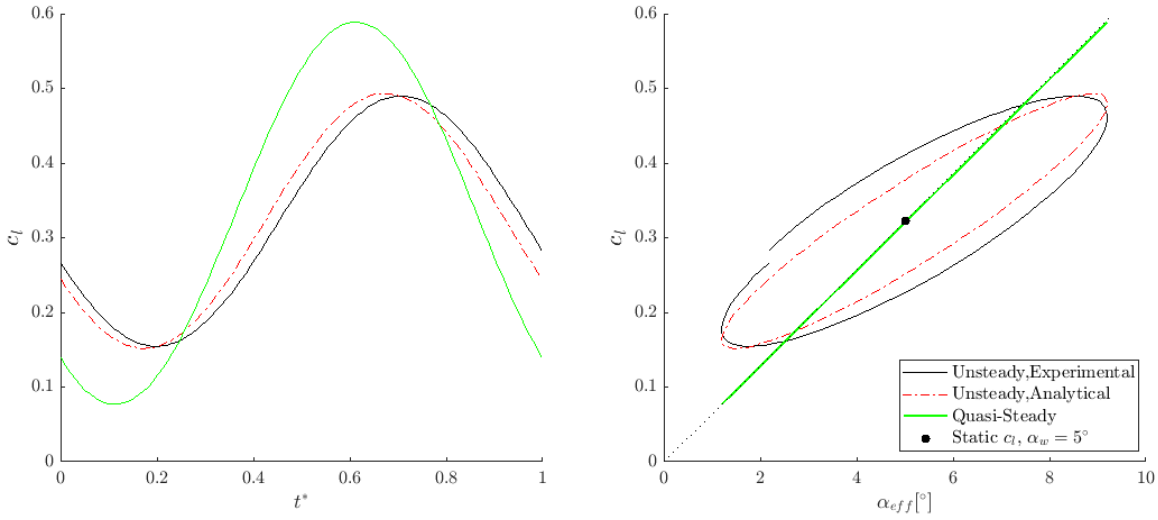

Figure 5.14: Comparison between the analytical and experimental hysteresis cycles in terms of lift coefficient c_l during the continuous gust case.

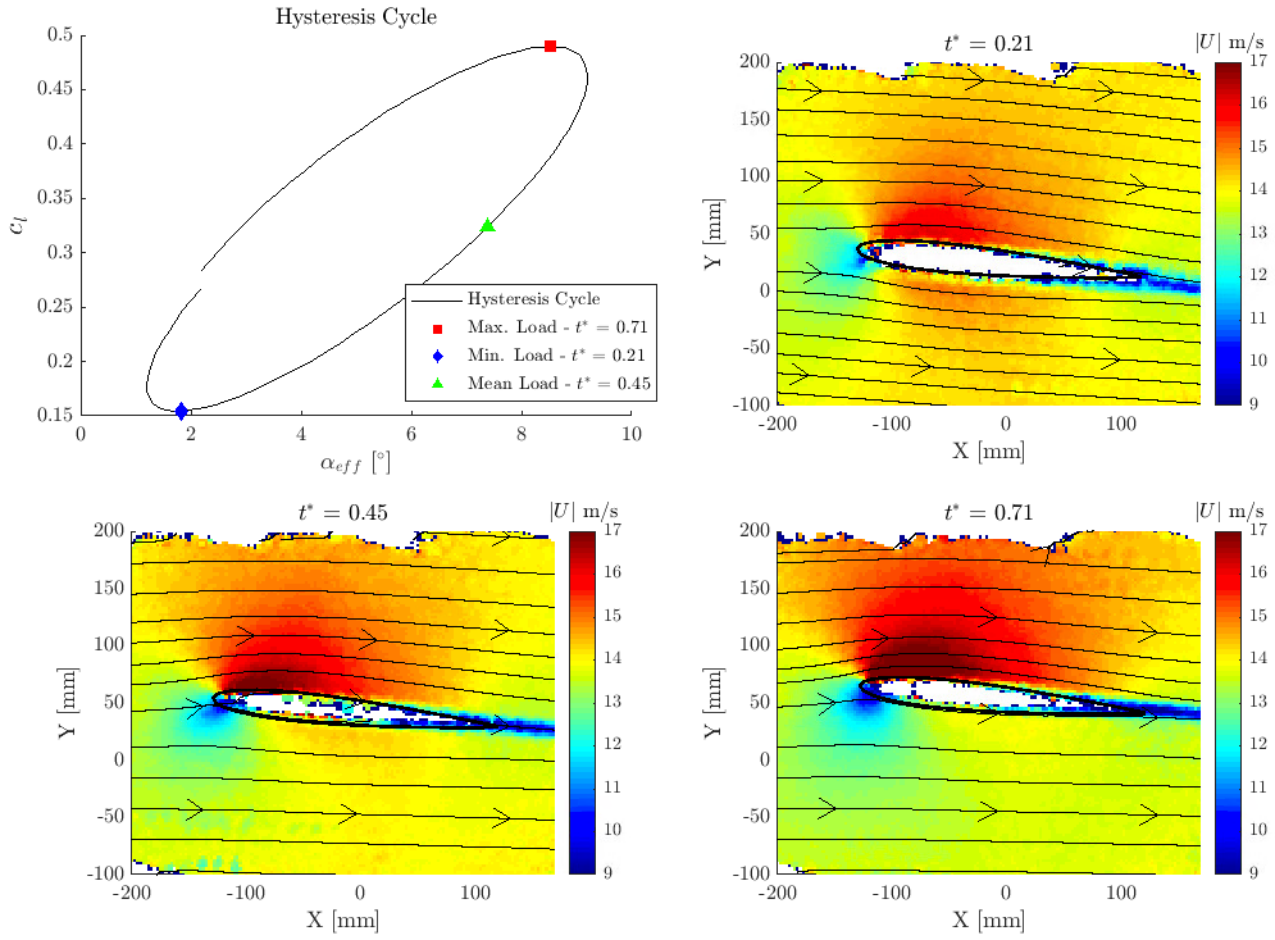

Figure 5.15: Hysteresis cycle during the continuous gust case and 2D plots of the velocity magnitude at z = 1500mm plane. The flowfields correspond to the highlighted phases in the hysteresis cycle. In-plane streamlines are plotted in black.

Flowfield evolution

The hysteresis loop displayed in Figure 5.14 is a well known characteristic of airfoils under unsteady conditions. The figure also shows the value of the load under a static deflection at $\alpha_w = 5°$ and U_∞ =14 m/s, as well as an estimation of the lift coefficient curve slope based on the available measurements.

The temporal information contained in the evolution of the lift coefficient and the hysteresis loop can now be used to analyze the evolution of the flowfield and to pick some of the most meaningful instants of the gust-wing interaction. This is done in Figure 5.15, where 3 instants have been selected and shown using the velocity magnitude information in the Z=1500 mm plane. The instants are the one of maximum and minimum load, as well as an intermediate phase showing the point of mean load.

The slices of the flow show an evolution which is clearly consistent with the load information given above. While all of them show the typical acceleration of the flowfield over the suction side of the airfoil, it can be seen that the maximum velocity at $t^* = 0.71$ (max. load) is indeed higher than at $t^* = 0.21$ (min. load) where the flow accelerates both over the pressure and suction side of the airfoil, thus decreasing the lift generated by the wing section. The slice corresponding to $t^* = 0.45$ depicts an intermediate state between the other two phases, as expected.

Quality assessment of the phase-averaged flowfields

On top of the overall temporal evolution of the flowfield, it is also interesting to perform a basic assessment of the quality of the phase-averaged velocity fields. One way to do this is by evaluating the velocity uncertainty, which can be computed based on the particle concentration and the flowfield as discussed in Section 4.1.4, following:

$$\epsilon_u = \frac{z_a \sigma_u}{\sqrt{N_{unc}}} \tag{5.11}$$

A coverage factor $z_a = 2$ is selected, providing a confidence level of 95% assuming a Gaussian distribution. The standard deviation of the velocity σ_u is computed from the phase-averaged flowfields, and the number of uncorrelated samples for each phase is estimated to be:

$$N_{unc} = \min(N_{cycles}, N_{part}) \tag{5.12}$$

where N_{cycles} is the number of periods used for the phase-averaging of the PIV data and N_{part} is the number of particles inside a given bin. As introduced in Chapter 3, a total of 240 cycles per PIV volume were used for the phase-averaging of the data. This estimate for N_{unc} is conservative and assumes that at least one uncorrelated measurement of the velocity is achieved for each phase in each cycle of oscillation, that is, that at least one particle is captured inside each bin every period. If the number of particles inside a cell is smaller than the number of cycles, this assumption becomes invalid and the number of particles inside the bin is chosen as the estimation for N_{unc} instead.

To do this, 4 locations around the airfoil in the Z = 1500 mm plane are selected. Location 1 corresponds to a point just in front of the leading edge of the section, Location 2 is positioned 4cm over the suction side of the airfoil and Location 3 corresponds to a point in the wake of the airfoil. Finally, a fourth location is positioned 1cm away from the surface of the airfoil to explore the quality of the data near the surface of the wing.

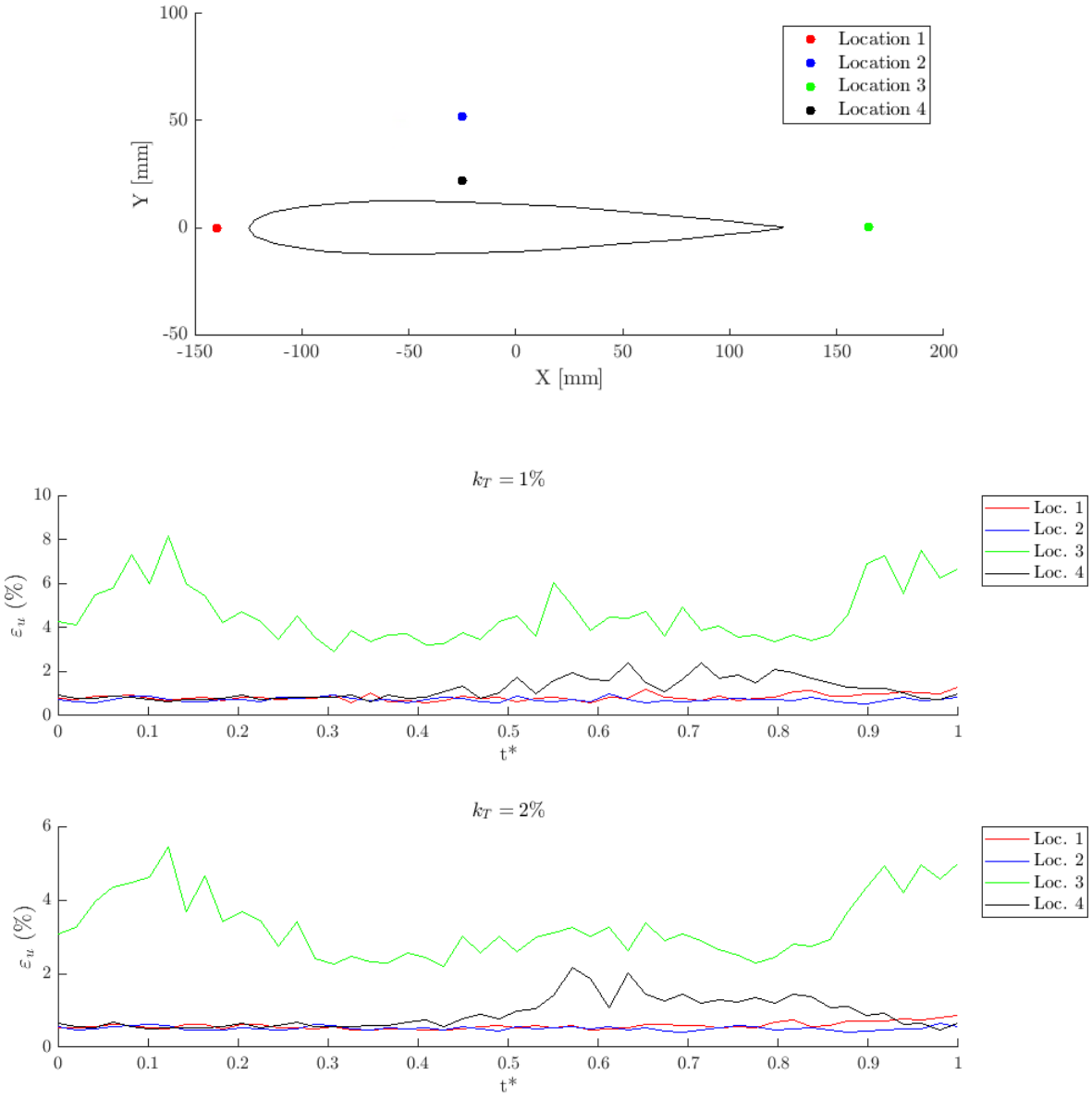

Figure 5.16: Relative uncertainty of the u component of the velocity over the period of oscillation. The uncertainty is shown for different locations around the airfoil and for different values of the time-kernel k_T used in the phase-averaging.

Figure 5.16 shows the evolution of the uncertainty of the u component of the velocity over the cycle of oscillation of the wing, expressed as a percentage of the freestream velocity U_∞ = 14 m/s. Locations 1,2 and 3 display consistent values of relative uncertainty of around 1%, while the uncertainty in the wake region increases to values of 5% on average. Some local increases of ε_u can be observed in Location 3 ($t < 0.3$, $t > 0.85$) and Location 4 ($0.5 < t^* < 0.9$). These are likely caused by a spatial error affecting the merging of the PIV views before the ensemble-averaging. Because of the proximity of Locations 3 and 4 to the surface of the wing and the boundaries of the PIV views, any errors in positioning are likely to manifest themselves in these regions. A secondary factor that affects the particle concentration, and therefore the uncertainty, is an irregular performance of the seeding system in terms of bubble production, although this effect is estimated to affect all phases equally.

There exist a series of options that can be used to improve values of the velocity uncertainty. For example, the value of the time kernel can be increased to improve the particle concentration. The effect of an increase in k_T from 1% to 2% is also displayed in Figure 5.16, showing that a small reduction in the velocity uncertainty is achieved. Other alternatives include increasing the size l_b of the bins used in the ensemble-averaging

process, which would provide a cubic increase in the number of particles per bin at the cost of a reduced spatial resolution of the resulting flowfield. A final option for future experiments could be to increase the number of cycles of the wing-gust interaction that are measured during the campaign, and to use a HFSB seeding system capable of providing a higher particle concentration.

As mentioned in the introduction of this section, for the final results of this study it has been decided to maximize both the temporal and spatial resolution, therefore minimizing the bin size and time kernel to l_b = 10 mm and k_T = 1% respectively. These settings have produced flowfields that clearly show the expected qualitative evolution and uncertainty levels which are in general below 10%, and therefore it has been decided that they are sufficiently good for the purpose of this thesis. It is possible that more detailed studies dealing with topics such as pressure reconstruction require a higher convergence to get smoother gradients for example. If that is the case, the steps described before (increasing bin size or temporal uncertainty) can be followed.

5.2.3. Dynamic loads

The final set of results related to dynamic cases is presented here and deals with the recovery of load information from the aerodynamic and structural measurements.

The calculation that can be performed is that of the total load acting on the wing, which can be later compared to force balance measurements. This calculation is simple due to the way that the optimization process has been set up since it has been designed to find the value of the uniform load distribution q_{ufm} which causes the wing model to deflect in the same way that the marker grid deflects. This is done for every time step, so an estimation of the evolution of the load over time can be obtained by a simple multiplication

$$F_y(t) = q_{ufm}(t) \cdot b \tag{5.13}$$

This is precisely done in Figure 5.17, where the comparison between the reconstructed total load and the force balance measurements is shown for the discrete gust cases at 14m/s and 24m/s. The reconstructed load shows a good agreement with the balance, especially in terms of the oscillation frequency and the mean force level before and after the gust encounter. The disagreement affects mostly the amplitude of the signal, where the reconstructed load overshoots the balance measurements both in the maximum and minimum load peaks.

This overprediction is likely to be caused by the constant load assumption used in the wing reconstruction algorithm, which is probably less valid at the points of maximum and minimum load. At these instants, both the aerodynamic and inertial loading will suffer significant changes over the span of the wing which the current wing model cannot capture. Another source of error could be the fact that the structural properties of the model - bending stiffness and stiffness ratio between the two sections considered - are not known exactly. For example, the use in the wing model of a bending stiffness higher than the real one would cause the optimization algorithm to move towards higher values of q_{ufm} in order to obtain the same wing deflection as if we were using a lower bending stiffness. However, the good agreement of the mean load seems to suggest that the current values used in the beam model are not a bad approximation.

Case	**Mean** F_y			**Max.** F_y			**Min.** F_y		
	$F_{y,rec}$ [N]	$F_{y,bal}$ [N]	Δ [%]	$F_{y,rec}$ [N]	$F_{y,bal}$ [N]	Δ [%]	$F_{y,rec}$ [N]	$F_{y,bal}$ [N]	Δ [%]
DG - 14m/s	15.3	15.7	-2.6	44.6	37.1	20.2	2.9	8.1	-64.6
DG - 24m/s	39.4	43.6	-9.6	114.7	100.9	13.7	11.1	28.0	-60.4

Table 5.3: Table listing the most significant values of the load reconstruction during the discrete gust encounters. The disagreement is expressed as a percentage with respect to the balance measurement. DG stands for Discrete Gust.

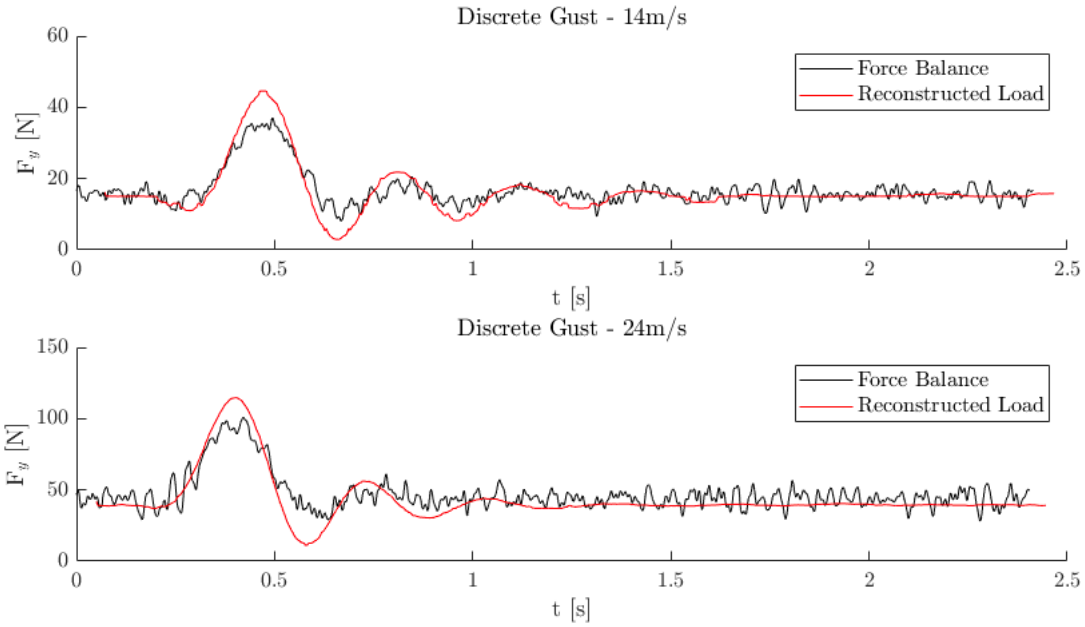

Figure 5.17: Comparison between the force balance measurements and the reconstructed total load during discrete gust encounters.

To provide a more accurate description of the agreement between the two measurements, Table 5.3 lists some of the exact values measured by the balance and reconstructed by the aforementioned methodology. The values show that the largest disagreements appear at the points of minimum load.

Separating the components of Collar's Triangle

It has been shown that the current methodology can be used to retrieve the value of the total transverse load acting on the wing and that this measurement is consistent with that of the force balance. However, this calculation includes both the aerodynamic and inertial loading into a single figure, meaning that it is not possible to know what the contribution of each term is.

In principle, the robotic PIV measurements can be used to perform this separation since:

- The inertial load can be estimated from the marker information over time, as described in Section 4.4.
- The aerodynamic loading along the span of the wing can be estimated using the circulation.

According to Collar's Triangle of forces, these two forces should be in equilibrium with the elastic forces. In this case, that equilibrium can be described by the beam equation:

$$\frac{\mathrm{d}^2}{\mathrm{d}z^2}\left(EI\frac{\mathrm{d}^2 w(z)}{\mathrm{d}z^2}\right) = q_{ufm}(t) \approx q_{aero}(t) + q_{inr}(t) \tag{5.14}$$

where the contribution of the inertial and aerodynamic loading is on the right hand side of the equation, and the elastic forces are contained in the left hand side. Therefore, the contribution of the elastic forces is precisely the value of q_{ufm} which the optimization outputs for each time step. Another estimate for q_{ufm} can be obtained from force balance measurements by dividing the load registered by the balance by the length of the wing.

The evolution of the 3 components during the continuous gust interaction is shown in Figure 5.18. The components are extracted from the Z = 1500 mm plane. It is clearly visible that the contribution of the aerodynamic loads is clearly dominant over the inertial effects, and that the combination of these two loads does not agree in amplitude with the elastic loads predicted by the optimization. On the other side, the sum of the aerodynamic and inertial loads is quite close to the estimation provided by the force balance.

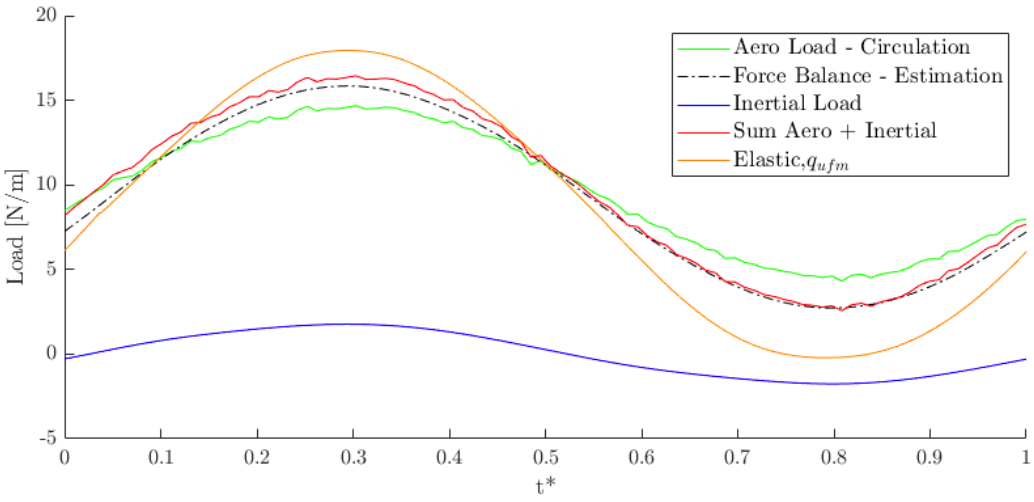

Figure 5.18: Evolution of the elastic, inertial and aerodynamic forces over the oscillation period during the continuous gust case.

This figure is particularly relevant for the objective of this thesis because it shows that the current methodology can indeed be used to separate the three components of Collar's triangle of forces. Additionally, it offers a good perspective of how the modelling assumptions used for the reconstruction of the wing structure deviate from the real physics. In this figure, this is represented by the disequilibrium between the elastic loads predicted by the optimization algorithm and the aerodynamic and inertial forces. The current methodology englobes these two terms into the value of q_{ufm}, and this figure shows that a possible improvement would be to introduce these two terms into the beam model separately. This statement is backed up by the fact that the sum of the measured inertial and aerodynamic terms is quite close to the estimation extracted from the balance.

6

Conclusions and Recommendations

This chapter summarizes the main outcomes of the research conducted during this thesis. The performance of the Robotic PIV system as a unified measurement system for large-scale aeroelasticity experiments will be discussed in the conclusions, followed by a series of recommendations regarding future work.

6.1. Conclusions

Aeroelastic interactions between fluids and man-made structures have been and will continue to be a subject of extensive research in many engineering fields as structures evolve towards more complex geometries and use more advanced materials. Part of this research involves conducting wind tunnel campaigns to gather experimental data which is typically acquired with several kinds of measurement systems such as the ones presented in the literature review. However, the use of these systems implies a series of limitations and undesired effects, mainly in terms of the spatial resolution of the measurements, the intrusiveness of the instruments and the complexity of the experimental setups which must be usually tailored for each campaign. Therefore, there exists a need for the development of a measurement technique capable of overcoming these limitations. This thesis is part of this effort and proposes the use of the Robotic PIV technique as a tool capable of providing full-field, simultaneous and integrated aerodynamic and structural measurements in a minimally intrusive way. To prove this concept, the following research goal has been defined:

"Develop a framework for the use of robotic PIV system as a tool for integrated, simultaneous and coherent aerodynamic and structural measurements by means of an experimental campaign on a flexible wing exposed to discrete and continuous gust excitations".

To achieve this research objective, a wind tunnel experiment is conducted in TU Delft's OJF facility. The investigation features the aeroelastic interaction between a flexible wing model and different kinds of aerodynamic excitations provided by a gust generator. The test object is fitted with a reflective marker grid so that information about its structural response can be captured with the cameras of robotic PIV system at the same time as the flowfield data using HFSB tracers. Additionally, given the formulation of the research goal, information from other independent measurement systems is needed to validate the data extracted from robotic PIV acquisitions. For this reason, tri-axial accelerometers, an optic fiber strain sensor and a force balance are also used during the investigation. The test cases used for the experiment include the static deflection of the wing at different speeds, the dynamic response to discrete 1-cosine gusts and the periodic interaction with a continuous sinusoidal gust.

Following the experimental campaign, a methodology has been developed to extract meaningful aerodynamic and structural data from the raw PIV measurements. On the structural side, a procedure has first been established to separate the structural tracers from the flow tracers and subsequently track them with Shake-The-Box. However, marker positional information offers limited insight by itself, which is why a simplified wing structural model based on Euler-Bernoulli beam theory has been created and used to reconstruct the entire wing geometry based on marker information. This model can also be used to obtain estimations of the loads acting on the wing.

The structural measurements obtained with this approach have been compared to the reference measurement systems. An excellent agreement with the accelerometer data has been found, being capable of recovering the wing tip acceleration accurately during discrete gust encounters. The longitudinal strains of the wing have also been reconstructed for the static deflection of the wing at two different speeds, finding a clear correlation between marker-based strains and the optic fiber measurements with maximum disagreements of the order of 100 microstrains. Finally, the total load acting on the wing during discrete gusts has also been recovered and compared to the reference provided by the force balance, obtaining again a good qualitative agreement and a maximum difference of 20% in the prediction of the maximum load. The results also show that the observed accuracy can only be achieved provided that some basic structural information about the test object is known in advance. However, the overall conclusion to be drawn from the analysis of the comparisons is that the use of marker tracking information in combination with a structural model is a promising approach to reconstruct the aeroelastic response of the wing.

It is worth highlighting that the use of a structural model in combination with marker tracking information requires good knowledge about the structural characteristics of the test object. These characteristics are needed to calibrate the structural model and, if they are not correct, significant differences between the reconstructed variables and their real values can be expected.

On the aerodynamic side, robotic PIV has been successfully capable of retrieving flowfield information for both steady and unsteady conditions on both sides of a section of the wing. The unsteady data has been phase-averaged and has only been captured for the case of a continuous sinusoidal gust, which is a periodic problem where it is easy to acquire several cycles of the phenomenon to gain statistical convergence. In addition and unlike in other experiments, the surface of the wing has been reconstructed using marker information, and it has been found to show a good compliance with the ensemble-averaged flowfield obtained with STB tracking of flow tracers. Finally, the velocity fields have been used to estimate the aerodynamic loading acting on the wing through the measurement of the circulation and the Kutta-Joukowski theorem. The load levels estimated with this approach are consistent with the force balance measurements both in the static deflection case and in the unsteady, continuous gust case. Furthermore, the unsteady loads measured based on the circulation display a temporal evolution which is consistent with typical unsteady aerodynamic effects: a time lag between the effective angle of attack and the lift coefficient is observed together with a dampening of the lift response in comparison to the quasi-steady approximation.

As the final step in this study, an attempt has been made to separate the different components of the forces acting on the wing according to the division proposed by Collar. It has been shown that it is possible to separate the different components and that a disequilibrium exists between them, although this is thought to be caused by the assumptions used in the structural modelling of the wing.

All in all, this study has fulfilled the proposed research goals, showing that marker tracking and flowfield information acquired with a robotic PIV system can indeed be used to reconstruct relevant aeroelastic information. The accuracy of the system to do so has been assessed showing promising results. Furthermore, a number of limitations and weaknesses of the current approach have been identified. This opens the possibility for future work and additional lines of research that could prove that this technique has the potential to become a non-intrusive and very versatile alternative to traditional measurement approaches in large-scale aeroelastic investigations.

6.2. Recommendations

As the final contribution of this study, a series of recommendations are given in this section. These recommendations are based on the limitations of the current methodology which have been observed during the analysis of the results, and that in the opinion of the author should be considered for future applications.

In the first place, even though the use of robotic PIV and STB tracking has been proven to be effective to track reflective markers placed on the surface of the wing, a significant error in the positioning in space of the markers has been observed as described in Section 4.2.3. This study has found a way to work around this problem by using only relative displacement information, but it is be desirable to have both reliable tracking and reliable positioning of the markers. Some hypotheses as to what the origin of the problem could be have been listed in this document, although a detailed investigation should be conducted to determine when this issue appears and how to avoid it. In particular, it is recommended to establish a procedure on how to

perform a successful VSC and OTF when performing marker tracking.

Secondly, since the results of this thesis show that the reconstructed wing surfaces and the surrounding flowfield show a good compliance, some improvements in the ensemble-averaging process could be realised. The current version of the process only allows the division of the volumetric flowfield domain in rectangular bins, which are not able to accurately reproduce the shape of curved surfaces. A possible approach would be to first reconstruct the structure surface based on marker information and create a structured volumetric grid around it such that the geometry is preserved, in a similar way as how meshing around bodies is done in Computational Fluid Dynamics.

Thirdly, it has been shown that the combined use of marker tracking information and a structural model of the wing is a viable way to reconstruct the structural variables of the problem and. In fact, this approach becomes mandatory if the retrieval of the structural loads is needed, since the marker positional information by itself does not contain force information. This study has used a very simplified wing model where the entire structure is reduced to a one dimensional Euler-Bernoulli beam, and while some promising results have been obtained, the assumptions used for the modelling are likely to be the origin of the observed discrepancies between measurements. Therefore, the use of a more complex structural model is highly recommended for future research. In particular, the present case could benefit from the addition of torsion as an extra degree of freedom, as well as from a more complex modelling of the wing instead of the use of the constant load assumption. A different approach could involve using a beam model where the load term is not found through an optimization, but rather computed from measurements as shown in Section 5.2.3 of this document.

Finally, this study shows that robotic PIV data can be used to retrieve all components of Collar's triangle in a periodic case, where the phase-averaging of aerodynamic data can be done using a reasonable amount of resources. This has been done for relatively low inflow speed of 14m/s and a reduced frequency of $\kappa = 0.11$. Future work should explore what the exact range of application of this technique is in terms of the parameters of the problem and the achievable temporal and spatial resolution. Some possible lines of work in this direction are:

- Application of this methodology to problems at higher flow speeds using double-pulse double-frame acquisition.
- Attempt the retrieval of the aerodynamic loads through pressure instead of the circulation around the wing. This opens the possibility to study the aeroelastic response of more complex geometries, which might not satisfy the assumptions used by the Kutta-Joukowski theorem.
- Exploring the application of this technique to discrete aeroelastic events where phase-averaging is not possible or at least much more expensive. A possible approach could involve data assimilation, where low-resolution robotic PIV data is combined with a computational fluid-structure-interaction simulation.
- Another aspect that should be assessed is the scale of deformations that can be measured with robotic PIV. In this case, the deformation is small enough to allow measurements where the robot is static: the wing is located far enough to avoid collisions but close enough to allow the detection of particles close to its surface despite the drop in laser light intensity. This situation would change considerably in cases where large structural deformations of the order of the size of the robotic PIV measurement volume are expected.

Bibliography

[1] Ronald J. Adrian. Scattering particle characteristics and their effect on pulsed laser measurements of fluid flow: speckle velocimetry vs particle image velocimetry. *Applied Optics*, 23(11):1690, 1984. ISSN 0003-6935. doi: 10.1364/ao.23.001690.

[2] Nereida Agüera, Gioacchino Cafiero, Tommaso Astarita, and Stefano Discetti. Ensemble 3D PTV for high resolution turbulent statistics. *Measurement Science and Technology*, 27(12), 2016. ISSN 13616501. doi: 10.1088/0957-0233/27/12/124011.

[3] H J Alons. OJF External Balance Documentation. (November), 2008.

[4] O. Ammann, T. Von Karman, and Glenn B Woodruff. The failure of the tacoma narrows bridge. Technical report, Federal Works Administration, 1941.

[5] M.P. Arroyo and C.A. Greated. Stereoscopic particle image velocimetry. *Measurement Science and Technology*, 2, 1991.

[6] Javad Baqersad, Peyman Poozesh, Christopher Niezrecki, and Peter Avitabile. Photogrammetry and optical methods in structural dynamics – A review. *Mechanical Systems and Signal Processing*, 86:17–34, 2017. ISSN 10961216. doi: 10.1016/j.ymssp.2016.02.011. URL `http://dx.doi.org/10.1016/j.ymssp.2016.02.011`.

[7] D. B. Barker and M. E. Fourney. Measuring fluid velocities with speckle patterns. *Optics Letters*, 1(4):135, 1977. ISSN 0146-9592. doi: 10.1364/ol.1.000135.

[8] R. Bleischwitz, R. de Kat, and B. Ganapathisubramani. On the fluid-structure interaction of flexible membrane wings for MAVs in and out of ground-effect. *Journal of Fluids and Structures*, 70(October 2016):214–234, 2017. ISSN 10958622. doi: 10.1016/j.jfluidstructs.2016.12.001.

[9] Johannes Bosbach, M. Kühn, and C. Wagner. Large scale particle image velocimetry with helium filled soap bubbles. *Experiments in Fluids*, 46:539–547, 2009. doi: 10.1007/s00348-008-0579-0.

[10] Alpheus W Burner, William A Lokos, Danny A Barrows, Alpheus W Burner, William A Lokos, and Danny A Barrows. In-flight aeroelastic measurement technique development. In *Optical Science and Technology, SPIE's 48th Annual Meeting*, San Diego, California, 2003. doi: 10.1117/12.504157.

[11] C.D. Butter and G.B. Hocker. Fiber optics strain gauge. *Applied Optics*, 17(18):2867–2869, 1978.

[12] Giuseppe Carlo Alp Caridi. *Development and application of helium-filled soap bubbles For large-scale PIV experiments in aerodynamics*. PhD thesis, Delft Univesity of Technology, 2016.

[13] P. Castellini, M. Martarelli, and E. P. Tomasini. Laser Doppler Vibrometry: Development of advanced solutions answering to technology's needs. *Mechanical Systems and Signal Processing*, 20(6):1265–1285, 2006. ISSN 08883270. doi: 10.1016/j.ymssp.2005.11.015.

[14] Julio Chu and James M Luckring. Experimental Surface Pressure Data Obtained on 65 ° Delta Wing Across Reynolds Number and Mach Number Ranges. Technical Report NASA Technical Memorandum 4645, National Aeronautics and Space Administration, 1996.

[15] A. R. Collar. The Expanding Domain of Aeroelasticity. *Journal of the Royal Aeronautical Society*, 50(428): 613–636, 1946. ISSN 0368-3931. doi: 10.1017/s0368393100120358.

[16] Guido Dietz, M. Sinapius, and G. Schewe. Limit Cycle Oscillantion Experiments at a transport aircraft wing model T. In *Proc. Int. Forum Aeroelasticity and Structural Dynamics*, Amsterdam, 2003.

[17] German Dutch Wind Tunnels (DNW). Model Deformation Measurement Techniques, 2018. URL https://www.dnw.aero/services/measurement-techniques/model-deformation/.

[18] E. H. Dowell, R. H. Scanlan, F. Sisto, H. C. Curtiss, and H. Saunders. *A Modern Course in Aeroelasticity*, volume 103. 2010. ISBN 9783319094526. doi: 10.1115/1.3254897.

[19] EASA. Easy Access Rules for Normal, Utility, Aerobatic and Commuter Category Aeroplanes (CS-23), 2018. URL https://www.easa.europa.eu/sites/default/files/dfu/CS-23Initialissue.pdf.

[20] G. E. Elsinga, F. Scarano, B. Wieneke, and B. W. Van Oudheusden. Tomographic particle image velocimetry. *Experiments in Fluids*, 41(6):933–947, 2006. ISSN 07234864. doi: 10.1007/s00348-006-0212-z.

[21] K N Everett, A A Gerneiy, and D A Durston. Seven-Hole Cone Probes for High Angle Flow Measurement : Theory and Calibration. *AIAA Journal*, 21(7):992–998, 1982.

[22] Federal Aviation Administration. Code of Federal Aviation Regulations, 2019. URL https://www.faa.gov/regulations{_}policies/faa{_}regulations/.

[23] Maxim Freydin, Miko Keren Rattner, and Daniella E Raveh. Strain-Based Aeroelastic Shape Sensing. *AIAA Journal*, Article in:1–17, 2019. doi: 10.2514/6.2018-0190.

[24] Qi Gao, Cecilia Ortiz-duenas, and Ellen K Longmire. Eddy structure in turbulent boundary layers based on tomographic PIV. In *15th Int Symp on Applications of Laser Techniques to Fluid Mechanics*, Lisbon, Portugal, 2010.

[25] I.E. Garrick. Aeroelasticity - Frontiers and Beyond. *Journal of Aircraft*, 13(9), 1976.

[26] E Garrigues. A Review of Industrial Aeroelasticity Practices at Dassault Aviation for Military Aircraft and Business Jets. *Aerospace Lab*, 9(14):1–34, 2018. doi: 10.12762/2018.AL14-09. URL http://www.aerospacelab-journal.org/sites/www.aerospacelab-journal.org/files/AL14-09{_}0.pdf.

[27] A De Gaspari, S Ricci, L Riccobene, and A Scotti. Active Aeroelastic Control Over a Multisurface Wing : Modeling and Wind-Tunnel Testing. *AIAA Journal*, 47(9), 2009. doi: 10.2514/1.34649.

[28] Daniele Giaquinta and Andrea Sciacchitano. Investigation of the Ahmed body cross-wind flow topology by robotic volumetric PIV. In *13th International Symposium on Particle Image Velocimetry – ISPIV*, Munich, Germany, 2019. doi: 10.18726/2019.

[29] Jorge Pereira Gomes and Hermann Lienhart. Time-phase resolved PIV/DMI measurements on two-dimensional fluid-structure interaction problems. *International symposium 13th Int Symp on Applications of Laser Techniques to Fluid Mechanics*, 16:29, 2006.

[30] Yves Govers, Julian Sinske, and D L R German. Latest design trends in modal accelerometers for aircraft ground vibration testing. In *Conference Proceedings of the Society for Experimental Mechanics Series*, number May. Springer, 2019.

[31] D. Heitzig, B. W. Van Oudheusden, and D Olejnik. Effects of asymmetrical inflow in forward flight on the deformation of interacting flapping wings. In *11th International Micro Air Vehicle Competition and Conference*, Madrid, Spain, 2019.

[32] Gene Hou, Jin Wang, and Anita Layton. Numerical Methods for Fluid-Structure Interaction — A Review. *Communications in Computational Physics*, 12(2):337–377, 2012. ISSN 1815-2406. doi: 10.4208/cicp.291210.290411s.

[33] Luther N Jenkins, Chung-sheng Yao, Scott M Bartram, Jerome Harris, Brian Allan, Oliver Wong, and W Derry Mace. Development of a Large Field-of-View PIV System for Rotorcraft Testing in the 14- x 22-Foot Subsonic Tunnel. In *AHS International 65th Forum and Technology Display*, Grapevine, TX; United States, 2009. ISBN 2009002237.

[34] Constantin Jux, Andrea Sciacchitano, and Fulvio Scarano. Surface Pressure Visualization by 3D PTV. In *18th International Symposium on Flow Visualization*, Zurich, Switzerland, 2018.

[35] Constantin Jux, Andrea Sciacchitano, Jan F.G. Schneiders, and Fulvio Scarano. Robotic volumetric PIV of a full-scale cyclist. *Experiments in Fluids*, 59(4), 2018. ISSN 07234864. doi: 10.1007/s00348-018-2524-1. URL http://dx.doi.org/10.1007/s00348-018-2524-1.

[36] Constantin Jux, Andrea Sciacchitano, and Fulvio Scarano. measurements Aerodynamic pressure reconstruction on generic surfaces from robotic PIV measurements. In *13th International Symposium on Particle Image Velocimetry – ISPIV*, Munich, Germany, 2019. doi: 10.18726/2019.

[37] A. Kalmbach and M. Breuer. Experimental PIV/V3V measurements of vortex-induced fluid-structure interaction in turbulent flow-A new benchmark FSI-PfS-2a. *Journal of Fluids and Structures*, 42:369–387, 2013. ISSN 08899746. doi: 10.1016/j.jfluidstructs.2013.07.004. URL http://dx.doi.org/10.1016/j.jfluidstructs.2013.07.004.

[38] Dinesh Kalpoe, Kourosh Khoshelham, and Ben Gorte. Vibration measurement of a model wind turbine using high speed photogrammetry. In *Proc. SPIE 8085, Videometrics, Range Imaging, and Applications XI*, Munich, Germany, 2011. doi: 10.1117/12.889440.

[39] Paul M.G.J. Lancelot, Jurij Sodja, Noud P.M. Werter, and Roeland De Breuker. Design and testing of a low subsonic wind tunnel gust generator. *Advances in aircraft and spacecraft science*, 4(2):125–144, 2017. ISSN 2287-528X. doi: 10.12989/aas.2017.4.2.125.

[40] LaVision. Minishaker: 3D camera for volumetric flow field measurements, 2018. URL https://www.lavision.de/en/download.php?id=2908.

[41] J. Gordon Leishman. *Principles of Helicopter Aerodynamics*. Cambridge University Press, 2006.

[42] Marc L Levitan and Kishor C Mehta. Texas Tech field experiments for wind loads part 1 : building and pressure measuring system. *Journal of Wind Engineering and Industrial Aerodynamics*, 41(44):1565–1576, 1992.

[43] Charrissa Y Lin, Edward F Crawleyf, Jennifer Heegl, and Aeroelasticity Branch. Open loop and preliminary closed loop results of a strain actuated active aeroelastic wing. *AIAA Journal*, 95(138), 1995. doi: 10.2514/6.1995-1386.

[44] Tianshu Liu, Alpheus W Burner, Thomas W Jones, and Danny A Barrows. Progress in Aerospace Sciences Photogrammetric techniques for aerospace applications. *Progress in Aerospace Sciences*, 54:1–58, 2012. ISSN 0376-0421. doi: 10.1016/j.paerosci.2012.03.002. URL http://dx.doi.org/10.1016/j.paerosci.2012.03.002.

[45] H.G. Maas, A. Gruen, and D. Papantoniou. Particle Tracking Velocimetry in three-dimensional flows. *Experiments in Fluids*, 15:133–146, 1993.

[46] L. Marimon Giovannetti, J. Banks, S. R. Turnock, and S. W. Boyd. Uncertainty assessment of coupled Digital Image Correlation and Particle Image Velocimetry for fluid-structure interaction wind tunnel experiments. *Journal of Fluids and Structures*, 68(July 2016):125–140, 2017. ISSN 10958622. doi: 10.1016/j.jfluidstructs.2016.09.002. URL http://dx.doi.org/10.1016/j.jfluidstructs.2016.09.002.

[47] Blanca Martinez, B. W. Van Oudheusden, Andrea Sciacchitano, and M. Karásek. Large-Scale Flow Visualization of a Flapping-Wing Micro Air Vehicle. In *18th International Symposium on Flow Visualization*, Zurich, Switzerland, 2018.

[48] A. Melling. Tracer particles and seeding for particle image velocimetry. *Measurement Science and Technology*, 8:1406–1416, 1997.

[49] Francesco M A Mitrotta, Andrea Sciacchitano, Jurij Sodja, Roeland De, and Bas W Van Oudheusden. Robotic-PIV measurements of the fluid-structure interaction between a flexible plate and a periodic gust. In *13th International Symposium on Particle Image Velocimetry – ISPIV*, Munich, Germany, 2019.

[50] Masaki Nakagawa, Frank Michaux, Stephan Kallweit, and Kazuhiro Maeda. Unsteady flow measurements in the wake behind a wind-tunnel car model by using high-speed planar PIV. In *11TH INTERNATIONAL SYMPOSIUM ON PARTICLE IMAGE VELOCIMETRY*, Santa Barbara, California, 2015.

[51] Matteo Novara, Daniel Schanz, Nico Reuther, Christian J. Kähler, and Andreas Schröder. Lagrangian 3D particle tracking in high-speed flows: Shake-The-Box for multi-pulse systems. *Experiments in Fluids*, 57 (8):1–20, 2016. ISSN 07234864. doi: 10.1007/s00348-016-2216-7.

[52] David Ordonez. Time-averaged pressure from Robotic Volumetric PIV, 2018. URL `http://resolver.tudelft.nl/uuid:01f4d050-efcb-4b6d-8bf2-5b3c9ce9a7ddhttp://resolver.tudelft.nl/uuid:01f4d050-efcb-4b6d-8bf2-5b3c9ce9a7dd`.

[53] Markus Raffel, Christian E Willert, Steve T Wereley, and Jürgen Kompenhans. *Particle Image Velocimetry: A practical guide*. Springer, 2nd edition, 2007. ISBN 9783540723073. doi: 10.1007/978-3-540-72308-0.

[54] D. Rajpal, E. Gillebaart, and R. De Breuker. Preliminary aeroelastic design of composite wings subjected to critical gust loads. *Aerospace Science and Technology*, 85:96–112, 2019. ISSN 12709638. doi: 10.1016/j.ast.2018.11.051. URL `https://doi.org/10.1016/j.ast.2018.11.051`.

[55] M. Ramakrishnan, G. Rajan, Y. Semenova, and G. Farrell. Overview of Fiber Optic Sensor Technologies for Strain / Temperature Sensing Applications in. *Sensors*, 16(99), 2016. doi: 10.3390/s16010099.

[56] Edoardo Saredi, Andrea Sciacchitano, and Fulvio Scarano. Multi- Δt 3D-PTV based on Reynolds decomposition. In *13th International Symposium on Particle Image Velocimetry – ISPIV*, Munich, Germany, 2019. doi: 10.18726/2019.

[57] F. Scarano. Tomographic PIV : principles and practice. *Measurement Science and Technology*, 24, 2013. doi: 10.1088/0957-0233/24/1/012001.

[58] Fulvio Scarano and Christian Poelma. Three-dimensional vorticity patterns of cylinder wakes. *Experiments in Fluids*, 47:69–83, 2009. doi: 10.1007/s00348-009-0629-2.

[59] Fulvio Scarano, Sina Ghaemi, Giuseppe Carlo Alp Caridi, Johannes Bosbach, Uwe Dierksheide, and Andrea Sciacchitano. On the use of helium-filled soap bubbles for large-scale tomographic PIV in wind tunnel experiments. *Experiments in Fluids*, 56(2), 2015. ISSN 07234864. doi: 10.1007/s00348-015-1909-7.

[60] Edward T. Schairer and Lawrence A. Hand. Measurements of Unsteady Aeroelastic Model Deformation by Stereo Photogrammetry. *Journal of Aircraft*, 36(6):1033–1040, 1999. ISSN 0021-8669. doi: 10.2514/2.2545.

[61] Daniel Schanz, Sebastian Gesemann, Andreas Schröder, Bernhard Wieneke, and Matteo Novara. Non-uniform optical transfer functions in particle imaging: Calibration and application to tomographic reconstruction. *Measurement Science and Technology*, 24(2), 2013. ISSN 13616501. doi: 10.1088/0957-0233/24/2/024009.

[62] Daniel Schanz, Sebastian Gesemann, and Andreas Schröder. Shake-The-Box: Lagrangian particle tracking at high particle image densities. *Experiments in Fluids*, 57(5):1–27, 2016. ISSN 07234864. doi: 10.1007/s00348-016-2157-1.

[63] Jan F.G. Schneiders, Fulvio Scarano, Constantin Jux, and Andrea Sciacchitano. Coaxial volumetric velocimetry. *Measurement Science and Technology*, 29, 2018.

[64] Andrea Sciacchitano and Fulvio Scarano. Elimination of PIV light reflections via a temporal high pass filter. *Measurement Science and Technology*, 25(8), 2014. ISSN 13616501. doi: 10.1088/0957-0233/25/8/084009.

[65] W. R. Sears. Some Aspects of Non-Stationary Airfoil Theory and Its Practical Application. *Journal of the Aeronautical Sciences*, 8(3):104–108, 1941. doi: 10.2514/8.10655.

[66] P. Sriram, J. I. Craig, and S. Hanagud. Scanning Laser Doppler Techniques for Vibration Testing. *Experimental Techniques*, 16(6):21–26, 1992. ISSN 17471567. doi: 10.1111/j.1747-1567.1992.tb00716.x.

[67] D. Tang and E. H. Dowell. Experimental and theoretical study of gust response for high-aspect-ratio wing. *AIAA Journal*, 40(3):419–429, 2012. ISSN 0001-1452. doi: 10.2514/3.15078.

[68] T. Theodorsen. General theory of aerodynamic instability and the mechanism of flutter. Technical report, National Advisory Committee for Aeronautics, 1949.

[69] C. Tropea, A. Yarin, and J.F. Foss. *Springer Handbook of Experimental Fluid Mechanics*. Springer Berlin Heidelberg, 2007. ISBN 9783540251415.

[70] B. W. Van Oudheusden. PIV-based pressure measurement. *Measurement Science and Technology*, 24, 2013. doi: 10.1088/0957-0233/24/3/032001.

[71] M.S. Vijaya. *Piezoelectric Materials and Devices*. CRC Press, 2013. ISBN 9781439887882.

[72] T. Von Karman and William R. Sears. Airfoil theory for non-uniform motion. *Journal of the Aeronautical Sciences*, 5(10), 1938.

[73] Noud P. M. Werter, Jurij Sodja, and Roeland De Breuker. Design and Testing of Aeroelastically Tailored Wings Under Maneuver Loading. *AIAA Journal*, 55(3):1012–1025, 2016. ISSN 0001-1452. doi: 10.2514/1.j054965.

[74] B. Wieneke. Volume self-calibration for 3D particle image velocimetry. *Experiments in Fluids*, 45(4): 549–556, 2008. ISSN 07234864. doi: 10.1007/s00348-008-0521-5.

[75] Bernhard Wieneke. Iterative reconstruction of volumetric particle distribution. *Measurement Science and Technology*, 24(2), 2013. ISSN 13616501. doi: 10.1088/0957-0233/24/2/024008.

[76] E. B. Wilson. Theory of an Aeroplane Entering Gusts. *American Philosophical Society*, 56(3):212–248, 1915.

[77] J.R. Wright and J.E. Cooper. *Introduction to aircraft aeroelasticity and loads*. John Wiley & Sons, Ltd, 2007. ISBN 9780470858400. doi: 10.1533/9781782421863.1.